PERFORMANCE ENHANCEMENT IN BULK THERMOELECTRIC MATERIALS

by

Si Hui

A dissertation submitted in partial fulfillment
of the requirements for the degree of
Doctor of Philosophy
(Mechanical Engineering)
in the University of Michigan
2016

Doctoral Committee:

Associate Professor Kevin P. Pipe, Co-Chair
Professor Ctirad Uher, Co-Chair
Professor Katsuo Kurabayashi
Professor Cagliyan Kurdak

To My Parents

Acknowledgements

I would like to thank, above all, my advisors, Professor Kevin Pipe and Professor Ctirad Uher, for their unconditional support and motivation through the past 6 years. They taught me how to make scientific discoveries from enormous amount of experimental data, how to convey a complicated scientific discovery and its potential applications to other fields, how to obtain an acute sense of science, and the most important, how to be a responsible, dedicated, enthusiastic, optimistic, and persistent person. I would like to thank my committee, Professor Katsuo Kurabayashi and Professor Cagliyan Kurdak, who gave me valuable advice and suggestions on my Ph.D. work and thesis. Professor Joseph Heremans, at Ohio State University, who taught me a lot about the transport theory in bulk materials. Professor Janusz Tobola, at AGH University of Science and Technology, who helped me with *ab initio* calculations and taught me about the fundamental theories on density functional theory. Professor Donald Morelli, at Michigan State University, who kindly allowed me to use his laboratory. Professor Stephen Forrest, who offered me the photoemission spectroscopy equipment and helpful discussion on the charge transfer model. Professor Xiaoqing Pan, Dr. Douglas Medlin, and Dr. Wenpei Gao, who dedicated themselves to detailed and professional TEM characterization and analysis on my samples. Professor Kai Sun at Department of Materials Science, Dr. Gordon Moore, and Dr. Jerry Li, who patiently walked me through the procedures and details on the sample preparation and characterization using electron microscopes. Professor Kai Sun at Department of Physics, who offered me helpful theoretical discussions on how to achieve high band dispersion order in

highly symmetric materials. Dr. James Salvador, at General Motors, who kindly helped me with SPS. Dr. Xu Lu, who helped me with materials sintering. I would like to thank all the co-authors, who dedicated themselves to contributing to my projects. I am thankful to all the former and current postdocs and students in Professor Pipe's lab and Professor Uher's lab, especially, Dr. Abhishek Yadav, Dr. Huarui Sun, Dr. Gunho Kim, Dr. Lei Shao, Dr. Kejia Zhang, Dr. Guoyu Wang, Dr. Xiaoyuan Zhou, Dr. Xianli Su, Dr. Hui Sun, Dr. Hang Chi, Mr. Vahid Rashidi, Mr. Chen Li, Mr. Shantonio Birch, Mr. Alexander Page, Mr. Trevor Bailey, Ms. Si Wang, Mr. Pan Ren, Mr. Lynn Endicott, Ms. Jennifer Ma, and Professor Junmei Fan, for their dedicated, unconditional and professional help with both inside and outside the lab. Especially, I would like to thank Mr. Alexander Page and Mr. Trevor Bailey for their help with my English during the past several years and corrections of this dissertation. Finally, I thank my parents, for their unwavering love and support, who help me overcome all the difficulties.

Table of Contents

Dedication ii

Acknowledgements iii

List of Figures viii

List of Tables xiii

Chapter 1 Introduction 1

1.1 Basic Concepts 3

1.2 Challenges and Approaches 6

Chapter 2 Synthesis and Measurement Setup 8

2.1 Thermoelectric Materials Synthesis 8

2.2 Crystallographic and Microstructural Characterization 9

2.3 Transport Measurements 9

2.3.1 High Temperature Electrical Properties Measurement 9

2.3.2 Low Temperature Thermoelectric Transport Properties Measurement 11

2.3.3 High Temperature Thermal Conductivity Measurement 14

2.3.4 Hall Effect Measurement 15

Chapter 3 Resonant Density of States in p-type CoSb3 16

3.1 Background 16

3.2 Prediction of Resonant Density of States in $CoSb_3$ through incorporation of Sn by Band Structure Calculation 18

3.3 Sample Synthesis and Pellet Sintering 20

3.4 Crystallographic and Microstructural Characterization 21

3.5 Thermoelectric Properties 28

3.6 Summary 40

Chapter 4 Thermoelectric Properties of *p*-type Filled Skutterudites $Yb_zFe_yCo_{4-y}Sb_{12-x}Sn_x$ 42

4.1 Background 42

4.2 Materials Synthesis and Pellets Sintering 43

4.3 Crystallographic and Microstructural Characterization 43

4.4 Transport Fitting Theory 46

4.5 Thermoelectric Transport Properties 50

4.6 Summary 57

Chapter 5 Engineering Temperature-Dependent Carrier Concentration for Average Power Factor Enhancement *via* Novel Doping Method 59

5.1 Introduction 59

5.2 Material Synthesis and Pellet Sintering 60

5.3 Crystallographic and Microstructural Characterization 61

5.4 Poisson Model 69

5.5 Transport Properties Calculation 73

5.6 Thermoelectric Transport Properties 76

5.7 Summary 97

Chapter 6 Thermoelectric Power Factor Enhancement from High Order Band Dispersion 99

6.1 Introduction 99

6.2 Theory 100

6.3 Results and Discussion 115

6.4 Summary 122

Chapter 7 Conclusion 124

References 128

List of Figures

Figure 1.1 Energy flow chart 2016. Source: LLNL March, 2016. Data is based on DOE/EIA MER (2015). The work was performed by Lawrence Livermore National Laboratory and the Department of Energy. LLNL-MI-410527 2

Figure 2.1 Schematic of the high temperature Seebeck coefficient and electrical conductivity measurement setup. 11

Figure 2.2 Low temperature thermoelectric transport measurement setup for (a) normal measurement and (b) radiation loss 14

Figure 3.1 Density of electronic states (DOS) calculation results as a function of energy for $CoSb_{3-x}Sn_x$ for (a) x~0, (b) x=0.01, (c) x=0.05, and (d) x=0.1 samples. 20

Figure 3.2 (a) Powder XRD patterns of three samples ($CoSb_{3-x}Sn_x$ with x=0.01, 0.05, and 0.1) before SPS. (b) Powder XRD patterns of two samples (with x=0.01 and 0.1) after SPS..... 23

Figure 3.3 (a) BSE image of the x=0.01 sample. (b) BSE image of the x=0.05 sample. (c) BSE image of the x=0.1 sample. (d) SEM image of the x=0 sample. 25

Figure 3.4 STEM analyses found the presence of some secondary phases localized to intergranular regions. (a) x=0 sample: example of Sb-rich intergranular phase. (b) x=0.05 and (c) x=0.15 samples show Sn-rich inclusions at grain-boundaries. (d) High resolution HAADF-STEM image of inclusion in (c). Inset shows diffractogram calculated from Fourier transform of STEM image. Spacings and angular relationships from this and other orientations identify the phase as SnO_2 (Cassiterite). The image in (d) is oriented along a [111] zone axis. 27

Figure 3.5 (a) Hall coefficients measured in all of the samples from room temperature to 800 K. The x values in the legend correspond to the Sn fraction in $CoSb_{3-x}Sn_x$. (b) The calculated temperature dependence of the Hall coefficient using a linearly dispersing valence band, assuming two constant carrier concentrations and a constant scattering parameter. 30

Figure 3.6 (a) Seebeck coefficients measured in all of the samples from room temperature to 800 K. The x values in the legend correspond to the Sn fraction in $CoSb_{3-x}Sn_x$. (b) Seebeck coefficients as a function of nominal Sn concentration x at 330 K, 560 K, and 800 K. 31

Figure 3.7 Electrical conductivity measured in all of the samples from room temperature to 800 K. The x values in the legend correspond to the Sn fraction in $CoSb_{3-x}Sn_x$. 32

Figure 3.8 Power factor from room temperature to 800 K. The x values in the legend correspond to the Sn fraction in $CoSb_{3-x}Sn_x$. 33

Figure 3.9 Measured data points compared to the Pisarenko relation at room temperature. 35

Figure 3.10 Fermi energy and carrier concentration as a function of x in $CoSb_{3-x}Sn_x$. 37

Figure 3.11 (a) Total thermal conductivity from room temperature to 825 K. The x values in the legend correspond to the Sn fraction in $CoSb_{3-x}Sn_x$. (b) Lattice thermal conductivity from room temperature to 825 K derived by subtracting the electronic thermal conductivity (approximated using the Wiedemann-Franz law) from the total measured thermal conductivity. x values in the legend correspond to the Sn fraction in $CoSb_{3-x}Sn_x$. 39

Figure 3.12 ZT values from room temperature to 800 K. x values in the legend correspond to the Sn fraction in $CoSb_{3-x}Sn_x$. 40

Figure 4.1 Powder XRD results of all the skutterudite samples from 5^o to 85^o. Secondary phases in the skutterudites samples can be identified by comparing the powder XRD results of the samples to the powder XRD patterns of the references 45

Figure 4.2 High temperature Hall coefficient of $Yb_zFe_{4-y}Co_ySb_{12-x}Sn_x$ samples. The room temperature carrier concentration of different samples is labeled in the figure. 51

Figure 4.3 High temperature (a) electrical conductivity and (b) Seebeck coefficient from 300 K to 800 K..... 53

Figure 4.4 (a) Room temperature mobility vs. carrier concentration for all 6 $Yb_zFe_yCo_{4-y}Sb_{12-x}Sn_x$ samples. (b) Room temperature Seebeck coefficient vs. carrier concentration. 54

Figure 4.5 High temperature power factor of $Yb_zFe_{4-y}Co_ySb_{12-x}Sn_x$ samples. 55

Figure 4.6 (a) Thermal conductivity from 300 K to 800 K. (b) Lattice thermal conductivity from 300 K to 800 K..... 56

Figure 4.7 High temperature thermoelectric figure of merit..... 57

Figure 5.1 Powder XRD patterns of 5 typically selected samples, GT-100, GT-90, GT-70, GT-30, and GT-10. 63

Figure 5.2 (a): Back scattered electron (BSE) image of the GT-98 sample with 10000× magnification. (b): BSE image of the GT-95 sample with 10000× magnification. (c): BSE image of the GT-90 sample with 800× magnification. (d): BSE image of GT-70 sample with 800× magnification. 65

Figure 5.3 (a): EDS mapping of Ge, Cu, In, and Te elements on the GT-70 sample.(b): High resolution TEM image on a small region of the GT-70 sample. (c): UPS results on the GT-100, GT-95, and GT-00 samples. (d): XPS Te-3d core levels..... 67

Figure 5.4 EDS mapping of Cu, Ge, In, and Te on a small region in the GT-70 sample. 68

Figure 5.5 (a): Room temperature carrier concentration change, electric field, and electrostatic potential distribution near the interface between GeTe and $CuInTe_2$ phases. (b): Average room temperature carrier concentration depletion over the bulk region as a function of secondary phase

concentration with various secondary phase geometries of different surface area to volume ratio. (The size of the secondary phase is set to be 3 nm) (c): Average carrier concentration depletion over the bulk region as a function of valence band offset. (The size of the secondary phase is set to be 3 nm and the doping ratio is set to be 5 mol%) (d): Average room temperature carrier concentration depletion over the bulk region as a function of the size of the $CuInTe_2$ inclusions. (The doping ratio is set to be 5 mol% and the surface to volume ratio is set to be 10 times larger than that of spheres) 73

Figure 5.6 (a)-(c): Normalized power factor as a function of carrier concentration and temperature for single parabolic bands of various effective masses. (d): Temperature-dependent power factor with carrier concentration following the trajectories shown in (c). 76

Figure 5.7 Specific heat capacity data of the GeTe-$CuInTe_2$ samples. Results of 3 consecutive measurements on the GT-87.5 sample are shown as the inset. 78

Figure 5.8 High temperature (a) electrical conductivity, (b) Seebeck coefficient, and (c) power factor of 8 GeTe-$CuInTe_2$ samples. 81

Figure 5.9 Schematics of the band alignment on the interface between GeTe and $CuInTe_2$ phases in GeTe-rich composites (a) 300 K before contact, (b) 300 K after contact, (c) 600 K before contact, (d) 600 K after contact, (e) 800 K before contact, and (f) 800 K after contact. 82

Figure 5.10 (a) High temperature inverse Hall coefficient of 5 GeTe-rich composites, (b) High temperature Fermi energy of pure $CuInTe_2$ and pure GeTe referred to the valence band maximum of $CuInTe_2$ calculated from the measured transport coefficients, and (c) High temperature power factor of the GT-100 and GT-95 samples for comparison. The carrier concentration dependent power factor at various temperatures for a single parabolic band with an effective mass of 0.5 m_e is shown as the inset of (c). The black and red lines in the inset of (c)

schematically correspond to the temperature dependence of the carrier concentration of GT-100 and GT-95 samples, respectively. 85

Figure 5.11 Schematics of the band alignment at the interface between GeTe and $CuInTe_2$ phases in $CuInTe_2$-rich composites at (a) 300 K before contact, and (b) 300 K after contact. 88

Figure 5.12 (a) High temperature carrier concentration of 3 $CuInTe_2$-rich composites, (b) High temperature Seebeck coefficient and electrical conductivity of the GT-15 sample, and (c) high temperature power factor of the GT-15 sample. 90

Figure 5.13 Low temperature (a) electrical conductivity, (b) carrier concentration, (c) Hall mobility, and (d) thermal conductivity of GeTe-$CuInTe_2$ composites. The inset of (c) is the comparison of room temperature mobility between GeTe-$CuInTe_2$ composites in this work and GeTe-In_2Te_3 solid solutions. 94

Figure 5.14 High temperature (a) thermal conductivity and (b) thermoelectric figure of merit ZT of 8 GeTe-$CuInTe_2$ composites. 96

Figure 6.1 Carrier concentration dependent (a) Fermi level, (b) Seebeck coefficient, (c) electrical conductivity, and (d) power factor for various band dispersions with acoustic phonon scattering parameter at 300 K. 116

Figure 6.2 (a) Density of states and (b) its energy dependence for various band dispersions. ... 119

Figure 6.3 Energy-dependent mobility for various band dispersions of carrier concentration of (a) 5×10^{27} m^{-3} and (b) 5×10^{28} m^{-3} 120

Figure 6.4 The mobility multiplied by the density of states as a function of carrier energy. 121

Figure 6.5 (a) Room temperature mobility of various band dispersions at different carrier concentrations. (b) Carrier concentration dependent power factor for a single parabolic band with various effective mass. 122

List of Tables

Table 3.1 Density, actual matrix composition, and lattice parameter of $CoSb_{3-x}Sn_x$ samples. 23

Table 4.1 Nominal composition, density measured by Archimedes method, actual matrix composition measured by electron microprobe analyzer (EMPA), lattice parameters calculated from the Rietveld analysis of the powder XRD data, and estimated carrier concentration calculated from the nominal composition. 46

Table 5.1 Measured densities, theoretical densities, and relative densities of $(Ge_2Te_2)_{x\%}(CuInTe_2)_{1-x\%}$. 63

Chapter 1 Introduction

With recent rising demand for energy all over the world, renewable energy resources are considered as necessary alternatives for the traditional fossil fuels since the oil reserves on the earth are shrinking. Another widely accepted issue of using petroleum, coal, or natural gas is global warming, which is caused by the emission of CO_2. Renewable energy resources include solar, wind, biomass, hydropower, geothermal, and etc. These energy resources are constantly replenished and generate almost zero CO_2 during the energy conversion process. As a result, renewable energy resources can help replace the finite-lifetime and polluting fossil fuels. Based on the latest U.S. energy consumption report published by the Lawrence Livermore National Laboratory,[1] which is also known as the energy flow chart, renewable energy resources contribute to approximately 10% of the total usable energy generated. This number is still increasing since a great many scientists and engineers in both academia and industry dedicate themselves to enhancing the efficiency of renewable energy conversion and reducing the cost. The energy flow chart does not take energy conversion efficiency into account; however, it quantitatively illustrates the efficiency of energy consumption. It is important to note that more than 60% of the total usable energy dissipates as waste heat. While improving the efficiency of energy consumption is an effective approach, directly converting waste heat energy into electricity is also appealing. Unfortunately, most of the traditional heat engines are not capable of making use of waste industrial heat energy effectively.

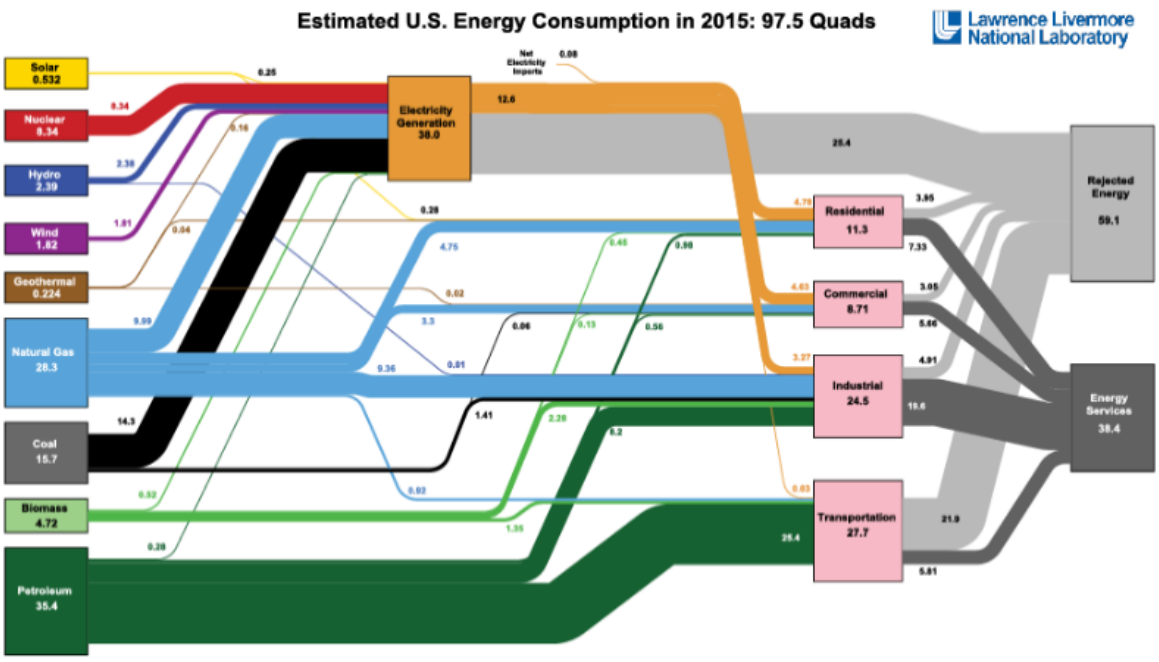

Figure 1.1 Energy flow chart 2016. Source: LLNL March, 2016. Data is based on DOE/EIA MER (2015). The work was performed by Lawrence Livermore National Laboratory and the Department of Energy. LLNL-MI-410527

An interesting phenomenon related to heat conversion was discovered by German physicist Thomas Johann Seebeck more than two centuries ago, and is now known as the Seebeck effect. It is a fundamental material property that a temperature gradient across a piece of material leads to an electrical potential difference between the hot end and the cold end. Such a property opens up a possibility to directly convert waste heat energy to electricity, the process referred to as the thermoelectric energy conversion. The direct application of the Seebeck effect was restricted to accurate temperature measurement using thermocouples until the mid of last century, when NASA successfully implemented thermoelectric generators (TEG) on spacecraft for reliable electricity generation.[2] Containing no moving parts makes thermoelectric generators are much more reliable and maintenance free compared to traditional heat engines.

Because of the advantages mentioned above, thermoelectric generators stood out among other heat engines and were selected to serve in deep space missions.

With the success of thermoelectricity in deep space missions, it is natural to extend its potentials to daily life. As mentioned at the beginning of the chapter, more than 60% of the total usable energy generated dissipates in the form of waste heat. If only 15% of waste heat energy was recovered by thermoelectricity, it would be equal to the total energy generated by all other renewable resources. Alphabet Energy, a thermoelectrics startup, has developed thermoelectric generators recovering exhaust-gas heat to optimize its use with large engines.[3] Such generators can also be rescaled for waste heat recovery in vehicles to save gasoline. Thus, thermoelectricity has held scientists' and engineers' attention during the past two decades.

Fortunately, the University of Michigan led a project funded by both the U.S. and China Department of Energy. As part of the team, we focus on engineering bulk polycrystalline inorganic materials for thermoelectric energy conversion efficiency enhancement. The engineered materials will eventually be used for thermoelectric generators fabrication. The project created an opportunity for us to make an improvement in the fundamental material-wise problem, which plays a crucial role in the commercialization of thermoelectricity.

1.1 Basic Concepts

As mentioned above, the Seebeck effect is a fundamental material phenomenon that a temperature gradient results in an electrical potential difference. A coefficient quantifying the ratio of the electric field and the temperature gradient is defined as the Seebeck coefficient S:

$$S = \frac{dV/dx}{dT/dx} = \frac{dV}{dT} \qquad \textit{Equation 1.1}$$

The Seebeck coefficient depends on other properties of the material, such as band structure and scattering processes of the carriers, and thus can be used to characterize the fundamental properties of materials in many areas of condensed matter physics, including superconductivity, for example. In the field of thermoelectricity, the Seebeck coefficient is a material-dependent parameter directly measuring the voltage generated by a unit temperature difference. Obviously, high Seebeck coefficient is desired for thermoelectric applications because high electrical voltage is desired. The Seebeck coefficient can be either positive or negative, corresponding to holes or electrons as the majority carriers, respectively.

The efficiency of thermoelectric energy conversion does not only depend on the Seebeck coefficient. Insulators usually have large Seebeck coefficients; however, it is not hard to imagine that insulators cannot be used for thermoelectricity since the carriers hardly move in these materials. This leads to another material-dependent property, the electrical conductivity or resistivity, which quantifies how conductive the materials are. High electrical conductivity (or low resistivity) is desired for thermoelectric applications. Another important material-based property that affects thermoelectric performance is thermal conductivity, which characterizes how much heat conducts through the materials per unit temperature gradient without being converted into electricity. Low thermal conductivity is desired since it prevents heat from "escaping". It can be understood in another way that a low thermal conductivity results in a large

temperature gradient per unit heat flow, hence a large voltage. In summary, combining the three factors discussed above, we define a material-wise thermoelectric figure of merit as:

$$ZT = \frac{S^2 \sigma T}{\kappa} \qquad \textit{Equation 1.2}$$

where σ is the electrical conductivity, κ is the thermal conductivity, and T is the absolute temperature. The thermoelectric figure of merit ZT is directly related to the thermoelectric energy conversion efficiency as:[4]

$$\phi_{max} = \frac{T_H - T_C}{T_H} \cdot \frac{\sqrt{1+Z\overline{T}}-1}{\sqrt{1+Z\overline{T}}+\frac{T_C}{T_H}} \qquad \textit{Equation 1.3}$$

where ϕ_{max} is the maximum thermoelectric conversion efficiency, assuming energy loss in other forms to be zero, T_H is the hot-end temperature, T_C is the cold-end temperature, and $\overline{T}$ is the average temperature of the thermoelectric material. A high thermoelectric figure of merit leads to high thermoelectric energy conversion efficiency and it is only a material-dependent parameter. Thus, increasing ZT is the main goal of engineering materials for thermoelectric applications.

Besides power generation at high temperatures, thermoelectricity also possesses a great potential for cooling applications at room or lower temperatures. The inverse Seebeck effect, also known as the Peltier effect, describes that passing an electric current through a junction between two different semiconductors will result in absorption of heat, which is different from the normal irreversible Joule heating associated with charge carrier scattering. Since thermoelectric cooling systems require neither Freon refrigerants nor moving parts, they are exceptionally reliable and quiet. Similarly, the thermoelectric cooling coefficient of performance is positively related to the thermoelectric figure of merit. Thus, engineering thermoelectric materials to enhance ZT is beneficial for both power generation and cooling.

1.2 Challenges and Approaches

The major challenge for enhancing the thermoelectric figure of merit is the three interrelated material-dependent parameters. A high Seebeck coefficient usually results in a low electrical conductivity, and vica versa. A high electrical conductivity also leads to a high thermal conductivity, since charge carriers also carry heat energy during the electrical conduction. Extensive research has been carried out to reduce the thermal part of the total thermal conductivity by scattering phonons; however, few significant progresses on the enhancement of the power factor, defined as $S^2\sigma$, have been made. Since the Seebeck coefficient and electrical conductivity are closely related to the details of the band structure and scattering processes, the work in this thesis focuses on engineering the band structure and scattering processes to enhance the power factor. In the following chapters, I will demonstrate the detailed approach and discoveries of my Ph.D. research. The contents of the following chapters are summarized as follows: in Chapter 2, I will discuss experimental aspects of the work including sample synthesis and measuring techniques; in Chapter 3, I will demonstrate the approach and discoveries of enhancing the thermoelectric figure of merit in *p*-type binary skutterudite $CoSb_3$ *via* incorporation of Sn dopants; in Chapter 4, thermoelectric properties of *p*-type filled skutterudites are discussed; in Chapter 5, a novel doping method to improve the average thermoelectric performance over a wide temperature range is proposed and its application in GeTe-$CuInTe_2$ composites is presented. in Chapter 6, I will present the numerical calculation results on the relation between the power factor and band dispersion index and a high dispersion index is

suggested for improving power factor; Chapter 7 will present the conclusion and suggestions for future work.

Chapter 2 Synthesis and Measurement Setup

In this chapter, I will demonstrate the experimental setups for thermoelectric materials synthesis and characterization.

2.1 Thermoelectric Materials Synthesis

An OmniLab glovebox provides an inert gas (N_2 or Ar) environment to minimize oxidation during sample preparation, such as raw elements weighing and mixing. The oxygen and moisture levels are maintained below 0.12 ppm and 0.5 ppm, respectively. A quartz sealing station provides a vacuum environment (~10^{-4} Torr) for ampoule creation to minimize oxidation during the process of high temperature heat treatment. Programmable high temperature furnaces calibrated beforehand are used for the synthesis and heat treatment of thermoelectric materials. Powders ground from the as-cast ingots are densified using spark plasma sintering (SPS) apparatus, with the sintering pressure and temperature programmable. An SPS and a homemade hot press setup are installed at the General Motors Research Labs and at the Michigan State University for pellet sintering, respectively.

2.2 Crystallographic and Microstructural Characterization

Powder X-ray diffraction (XRD) characterization was carried out using Rigaku and Scintag XRD diffractometers at the Electron Microbeam Analysis Laboratory – Central Campus (EMAL) at the University of Michigan. Phase identification and lattice parameters were determined by analyzing the diffraction peak patterns using the Rietveld method with the Maud.[5] The XRD equipment generally has a detection limit of ~5%. Backscattered Electron (BSE) Microscopy, Energy Dispersive X-ray Spectroscopy (EDS), and Secondary Electron Microscopy (SEM) were carried out with an FEI Helios and a JEOL – 7800FLV FE scanning electron microscope at the Michigan Center for Materials Characterization (MC^2) at the University of Michigan for micron-scale phase identification and structural analysis. Actual elemental composition and its distribution were characterized with an SX-100 Electron Microprobe at EMAL. Transmission electron microscopy (TEM) was performed by Dr. Douglas Medlin at the Sandia National Laboratory and Dr. Wenpei Gao at the Oak Ridge National Laboratory for the determination of nano-scale phase identification and structural analysis. Ultraviolet and X-ray photoemission spectroscopy (UPS and XPS) were performed in Professor Stephen Forrest's Lab at the University of Michigan for Fermi level detection.

2.3 Transport Measurements

2.3.1 High Temperature Electrical Properties Measurement

High temperature measurements of the Seebeck coefficient and electrical conductivity were performed from room temperature to 800 K using a custom setup. $3 \times 3 \times 10$ mm^3 specimens were cut from sintered pellets and the measurement configuration shown schematically in Figure 2.1 was used. A heater was attached on top of the bar-shaped sample to generate a temperature gradient. Two Type-R (Platinum-Platinum/Rhodium) thermocouples were attached with silver epoxy on the side of the sample to measure the temperature. The platinum wires of the thermocouples were also used to measure the voltage signal across the sample between the tips of the two thermocouples. Two copper wires were connected to the bottom and the top of the sample to generate a current through the sample. The whole setup was placed in a high temperature furnace, which can reach a temperature of 1000 K. The Seebeck coefficient was measured by fitting the voltage vs. temperature curve, the data taken continuously after the heater was turned on. Electrical conductivity was measured by fitting the voltage vs. current curve. The furnace, together with the sample, was installed in an argon environment with a constant argon flow to prevent oxidation at high temperatures.

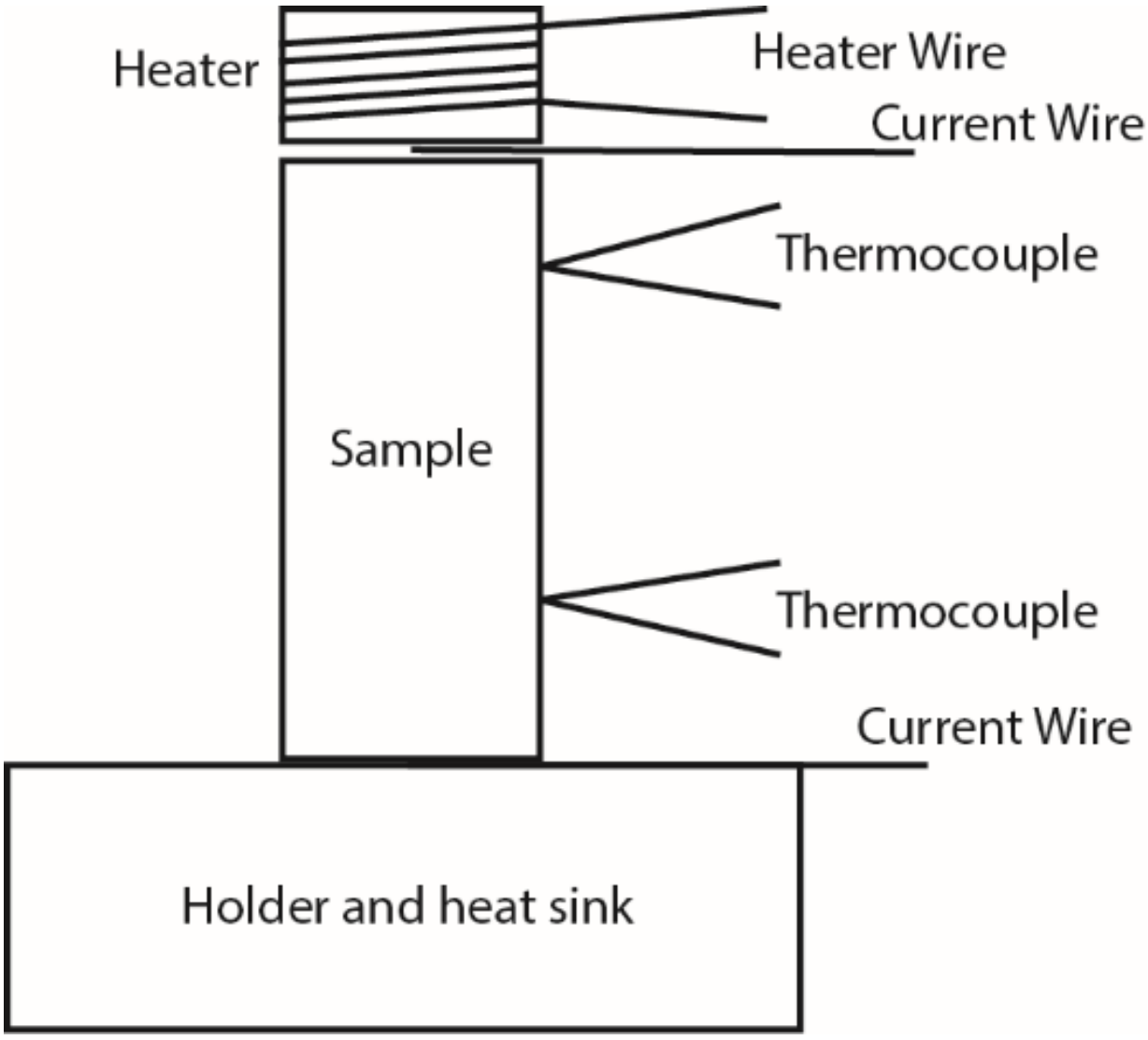

Figure 2.1 Schematic of the high temperature Seebeck coefficient and electrical conductivity measurement setup.

2.3.2 Low Temperature Thermoelectric Transport Properties Measurement

Low temperature measurements of the Seebeck coefficient and electrical conductivity were very similar to those at high temperature. In addition, low temperature thermal conductivity was measured at the same time in our setup. $3\times3\times10$ mm^3 bars were cut from sintered pellets. A

strain gauge heater was attached on top of the bar-shaped sample using varnish as the glue to build up a temperature gradient across the sample for Seebeck coefficient and thermal conductivity measurements. To provide an electrical current for resistivity measurements, a copper wire was also attached on top of the sample, under the heater, using indium. The sample was placed on a bronze holder used as the heat sink and electrical conductor. Two Type-T thermocouples (Constantan-Copper) were attached on the side of the sample using indium as contact points and the copper wires were used to read the voltage signal. A steady-state method was used to measure the Seebeck coefficient and thermal conductivity. The voltage and the temperatures of the two thermocouples were read when they stabilized at a certain heating power. Taking the temperatures of the hot and cold end of the sample as T_h and T_c, the Seebeck voltage as V_s, the power generated in the heater as $W_h = I_h V_h$, the cross-sectional area of the sample to be A and the distance between the two thermocouple tips as l, then the thermal conductivity and Seebeck coefficient can be expressed as, respectively:

$$Seebeck = \frac{V_s}{T_h - T_c} \qquad \textit{Equation 2.1}$$

$$Thermal\ Conductivity = \frac{W_h \cdot l}{(T_h - T_c) \cdot A} \qquad \textit{Equation 2.2}$$

The sample with the holder was placed in a cryostat, and liquid nitrogen or liquid helium was used to cool the samples to ~70 K or 4 K, respectively. The sample was surrounded by a radiation shield to reduce thermal radiation induced measurement error, and the cryostat was pumped down to 10^{-6} Torr to suppress convection induced measurement error. The temperatures of the holder and the radiation shield were kept at a known temperature using a heater controlled by a Cernox thermometer. The measurement setup is schematically shown in Figure 2.2a.

Although thermal conductivity can be measured at room temperature or below, thermal radiation losses introduce a large error especially near room temperature, for low thermal conductivity materials. Thus, it is crucial to correct for radiation loss. Taking the holder and the radiation shield to be at temperature T_0, the temperatures of the cold and hot thermocouple tips to be T_c and T_h, the emissivity to be ε_e, and Stefan's constant to be σ_r, the radiation loss in steady state is:

$$W_{radiation\ loss} = \sigma_r \varepsilon_e \left\{ \left(\frac{T_h + T_c}{2} + T_0 \right)^4 - T_0^4 \right\} \qquad \textit{Equation 2.3}$$

Since we cannot accurately determine the value of $\sigma_r \varepsilon_e$, this amount of heat must be measured experimentally. Each time after the regular measurement (with the samples attached to the holder), we detached the sample from the holder with all of the other wires untouched. The detached sample was then suspended in the chamber using a thin thread (a thermal and electrical isolator). The radiation loss power was then measured by adjusting the heater power to make the average temperature rise of the sample identical with the previous value during the regular measurement:

$$T_h + T_c = T_h' + T_c' \qquad \textit{Equation 2.4}$$

where T_h' and T_c' are the temperatures of the hot and cold tips of the two thermocouples during the radiation loss measurement. Then the heater power will be equal to the radiation loss power and the value of $\sigma_r \varepsilon_e$ solved by Eqn. 2.3 will be used to estimate the radiation loss at lower temperatures. The radiation loss measurement setup is schematically shown in Figure 2.2b.

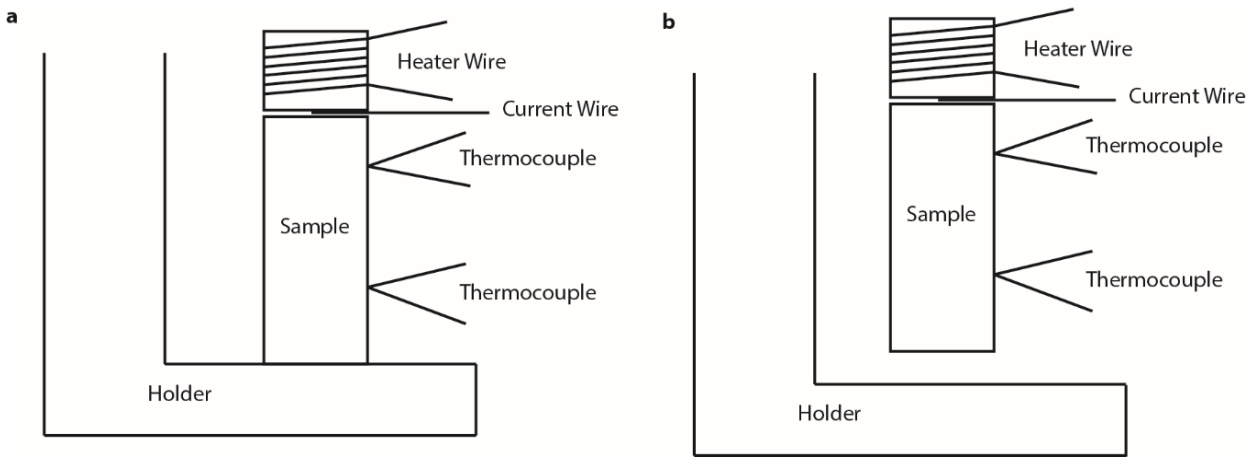

Figure 2.2 Low temperature thermoelectric transport measurement setup for (a) normal measurement and (b) radiation loss

2.3.3 High Temperature Thermal Conductivity Measurement

High temperature thermal conductivity cannot be measured using the steady state method due to the much larger radiation loss at elevated temperatures. Instead, high temperature thermal conductivity is measured using an indirect method, according to the relation:

$$\kappa = D \cdot C_p \cdot \rho \qquad \textit{Equation 2.5}$$

where D is the thermal diffusivity, C_p is the specific heat capacity, and ρ is the density. Thermal diffusivity was measured using the laser flash method [6] on a disc-shaped sample of thickness from 1 mm to 3 mm. The time-dependent temperature profiles of the bottom of the sample were detected after a laser pulse hit on the top of the sample. Thermal diffusivity was then determined by fitting the temperature profile with the solution of the thermal diffusion equation. Specific heat capacity was measured using differential scanning calorimetry (DSC). Density was then measured using the Archimedes method.

2.3.4 Hall Effect Measurement

The high temperature Hall coefficient was measured using a custom setup with a superconducting magnet cooled to 4.2 K to generate a steady magnetic field up to 1T. Low temperature Hall coefficient was measured using a Quantum Design Magnetic Properties Measurement System (MPMS). For both high temperature and low temperature Hall characterization, an AC resistance bridge was implemented to measure the Hall signal.

Chapter 3 Resonant Density of States in p-type CoSb3

3.1 Background

As discussed in Chapter 1, thermoelectric technology has been recognized as a promising technique to make use of waste heat energy. Since many applications of high temperature thermoelectric power generation occur in environments with significant vibrations, such as car electricity recovery, thermoelectric devices should possess good mechanical properties to survive occasional mechanical vibrations. Among many promising thermoelectric materials, skutterudites have attracted a lot of attention during the past several decades not only due to their excellent electrical properties, but also their outstanding mechanical properties. Both measurements and calculations have verified that $CoSb_3$, a binary paradigm of this large class, is a narrow-gap semiconductor possessing high mobility.[7-11] However, the high thermal conductivity (on the order of 10 $Wm^{-1}K^{-1}$ at room temperature) is too high for practical thermoelectric applications.[9, 10] The special crystal structure of this class of materials opens the possibility of reducing its intrinsic thermal conductivity by filling the structure with guest elements. The near square planar rings composed of 4 pnicogen atoms fill up 6 out of the 8 cubes formed by the M atoms in the binary skutterudites MX_3, where M stands for Co, Rh, or Ir while X represents P, As, or Sb.[12] Guest elements with small ionic radius can then be filled in the two remaining "empty" cubes in the unit cell, which are often referred to as "voids" or "cages".

These guest elements are often denoted as “fillers”, and the resulting filled lattice structure is known as a filled skutterudite. The weakly bonded fillers significantly reduce thermal conductivity by resonantly scattering phonons without dramatically affecting the electrical properties; this effect has been studied using a variety of elements.[13-21] A *ZT* as high as 1.7 was reported in the *n*-type filled skutterudites $Ba_{0.08}La_{0.05}Yb_{0.04}Co_4Sb_{12}$,[18] which is a dramatic enhancement compared to the binary $CoSb_3$ compound (~0.1). Unfortunately, due to an unfavorable valence band structure, *p*-type skutterudites, even filled with guest elements, have proven to be a challenging area of study to achieve a *ZT* value above 1.[19-21]

On the one hand, introducing dopants to create mass disorder or “rattling” states to reduce the lattice thermal conductivity is an effective means to improve the thermoelectric performance of $CoSb_3$-based materials. On the other hand, the numerator of *ZT*, known as the thermoelectric power factor $S^2\sigma$, offers a complementary approach in which electronic transport properties are improved. Here, the Seebeck coefficient S and the electrical conductivity σ are both determined by the band structure, the Fermi level position, and the scattering processes. Usually, S and σ are closely interdependent, and increasing both factors simultaneously is very difficult. A promising approach to improve the power factor given the trade-off between S and σ is to explore dopants that may form resonant density of states that can increase the density of states over a small range of carrier energies.[22-24] In order to realize an increase in Seebeck coefficient over typical dopant concentrations without sacrificing electrical conductivity, the Fermi level must also fall in the range of energies at which the band experiences a distortion due to the impurity. This approach has been successfully demonstrated using the dopant Tl in PbTe[25] and the dopant Sn in Bi_2Te_3.[26]

In this chapter, I report the exploration on Sn substitution for Sb as a potential means to form a resonant contribution to the density of states of $CoSb_3$. I predicted by band structure calculations that Sn, when substituted for Sb, should distort the density of states in a way that is reminiscent of the behavior of Tl in PbTe and Sn in Bi_2Te_3. I then conducted experiments where we substitute Sn for Sb, and find that the solubility limit of Sn in $CoSb_3$ is too low to achieve hole concentrations sufficient to make the Fermi level reach the energies at which the valence band is distorted.

3.2 Prediction of Resonant Density of States in $CoSb_3$ through incorporation of Sn by Band Structure Calculation

Ab initio calculations were carried out at AGH University of Science and Technology by Dr. Janusz Tobola. Electronic structure calculations of skutterudite-type (space group Im-3, No. 204) $CoSb_{3-x}Sn_x$ (x=0, 0.01, 0.025, 0.05 and 0.1) were performed using the all-electron self-consistent Korringa-Kohn-Rostoker (KKR) method, combined with the coherent potential approximation (CPA), which allows us to model the chemical disorder on the Sb site.[27, 28] In all computations, experimental values of the lattice constants and atomic positions, determined from XRD, were used. A self-consistent crystal potential of muffin-tin form was constructed with the local density approximation (LDA) framework and employed the Perdew-Wang expression for the exchange-correlation part.[29] For well-converged atomic charges (below 10^{-3} e) and potentials (below 1 mRy), the total and partial density of states (DOS) decomposed according to site (atoms) and angular momentum (s orbit, p orbit, d orbit, etc.) were computed

using the integration tetrahedron method in reciprocal space (~130 k-space points in the irreducible part of the Brillouin zone). The Fermi level (E_F) was precisely determined from the generalized Lloyd formula,[30] which appears to be particularly important in systems on the verge of semiconductor-metal crossovers. Core states were calculated fully relativistically, while valence states were treated in a nonrelativistic approach.

The calculated density of states (DOS) is shown in Fig. 3.1. The figure clearly shows that Sn shifts the Fermi level into the valence band, and thus it should act as a *p*-type acceptor impurity. Fig. 3.1c shows a maximum in the DOS due to Sn impurity at approximately 0.3 eV below the valence band edge, and 0.05 eV below the Fermi energy. Fig. 3.1d suggests that substituting 3% of the Sb atoms with Sn atoms (x=0.1) should bring the Fermi level into the region of the valence band that is distorted by the presence of Sn. The *ab initio* calculations clearly predict that Sn impurities should enhance the Seebeck coefficient without sacrificing too much electrical conductivity by generating the resonant density of states and moving the Fermi level to their vicinity simultaneously.[24] In the following sections, I explore this possibility experimentally.

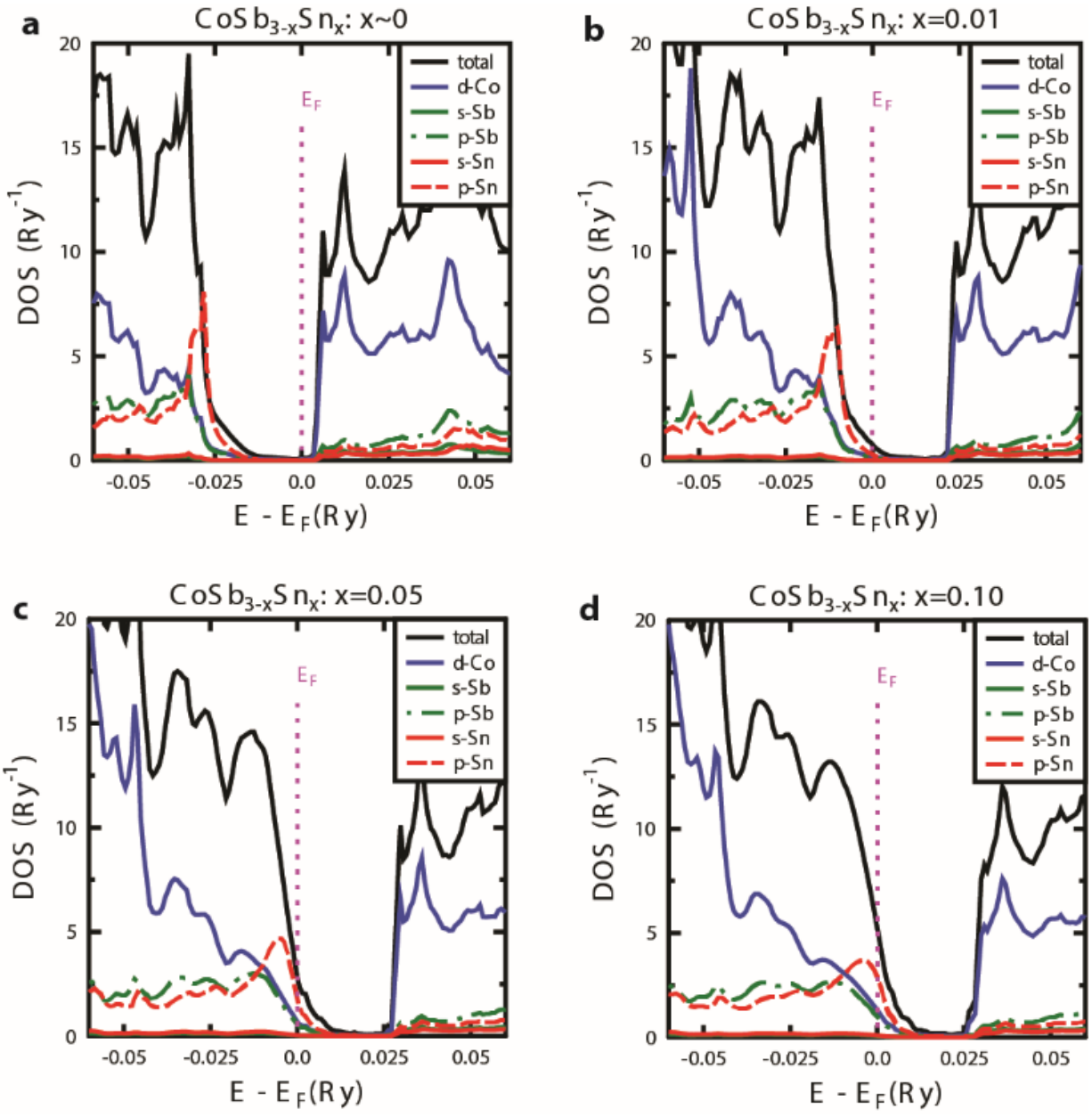

Figure 3.1 Density of electronic states (DOS) calculation results as a function of energy for $CoSb_{3-x}Sn_x$ for (a) x~0, (b) x=0.01, (c) x=0.05, and (d) x=0.1 samples.

3.3 Sample Synthesis and Pellet Sintering

Polycrystalline $CoSb_{3-x}Sn_x$ samples with various Sn doping concentrations (x = 0, 0.01, 0.025, 0.05, 0.1 and 0.15) were prepared for this study. Cobalt (powder, 99.998%), antimony (shot, 99.9999%), and tin (99.995% pure powder for x>0.01 and 99.9999% pure shot for x=0.01) were weighed and mixed in quartz tubes in the OmniLab glovebox to minimize oxidation. The tubes were then evacuated to a pressure below 10^{-3} Torr and sealed to prevent oxidation during the high temperature heat treatment. The materials were melted at 1373 K for 12 hours followed by annealing at 1023 K for 7 days. The annealed ingots were ground by hand to micron-size powders, of which a portion was examined by powder XRD. The remaining powders were sintered to high density ingots (cylinders of 12 mm diameter and 10 mm height) using SPS at 923 K and 50 MPa for 5-10 min. Ingot density was measured using the Archimedes method, after which the ingots were cut into various sizes for transport measurements. Small ingot pieces were reserved for high-temperature heat capacity measurements, and others were polished for electron microprobe analysis (EMPA), scanning electron microscopy (SEM), and transmission electron microscopy (TEM) studies. Certain pieces that contained secondary phases of Sb or Sn (based on the results of XRD before SPS), were ground to powders again for XRD after SPS to study whether SPS suppressed the formation of Sb or Sn secondary phases with low melting point.

3.4 Crystallographic and Microstructural Characterization

Powder XRD results before and after the SPS process are shown in Fig. 3.2a and Fig. 3.2b, respectively. Three $CoSb_{3-x}Sn_x$ with x=0.01, 0.05, and 0.1 were selected in particular to

clearly show the trend. The majority phase was confirmed to be $CoSb_3$. Secondary phases were identified as Sb for lightly and moderately doped samples (x=0.01 and 0.05) and Sn and $CoSb_2$ for the heavily doped one (x=0.1). Powder elements adhering to the inner walls of the ampoules caused the unavoidable loss of cobalt powder during the preparation process. This resulted in an excess of Sb in lightly and moderately doped samples, while the appearance of Sn and $CoSb_2$ phases in the heavily doped sample (x=0.1) were due to the small solubility limit (x<0.1 for $CoSb_{3-x}Sn_x$) of Sn on the Sb sites. The moderately doped sample (x=0.05) was verified to be free of Sn or $CoSb_2$ secondary phases, suggesting a solubility limit larger than 0.05 for the $CoSb_{3-x}Sn_x$ compounds. A decrease in the concentration of the secondary phases was observed after the samples were subjected to SPS, suggesting that SPS significantly suppressed the formation of Sb and Sn secondary phases. The Rietveld refinement results performed using the MAUD program are shown in Table 3.1.[5] The lattice parameter was verified to increase with Sn concentration for x<0.15, which is consistent with the fact that Sn ions have a larger atomic radius [31] (0.294nm) than Sb atoms (0.245nm). The most heavily doped sample (x=0.15) constitutes an exception: it has a smaller lattice parameter than the x=0.1 sample, indicating that not all the Sn went into solution.

Nominal Composition	Density (g/cm^3)	Actual matrix composition	Lattice parameter (Å)
$CoSb_3$	7.04	$CoSb_{3.0487}$	9.0323
$CoSb_{2.99}Sn_{0.01}$	7.14	$CoSb_{3.0419}Sn_{0.0028}$	9.0394
$CoSb_{2.975}Sn_{0.025}$	7.2	$CoSb_{3.0284}Sn_{0.0059}$	9.0437
$CoSb_{2.95}Sn_{0.05}$	7.65	$CoSb_{3.0122}Sn_{0.0158}$	9.0462
$CoSb_{2.9}Sn_{0.1}$	7.69	$CoSb_{2.9719}Sn_{0.0772}$	9.0462
$CoSb_{2.85}Sn_{0.15}$	7.62	$CoSb_{2.9737}Sn_{0.0867}$	9.0443

Table 3.1 Density, actual matrix composition, and lattice parameter of $CoSb_{3-x}Sn_x$ samples.

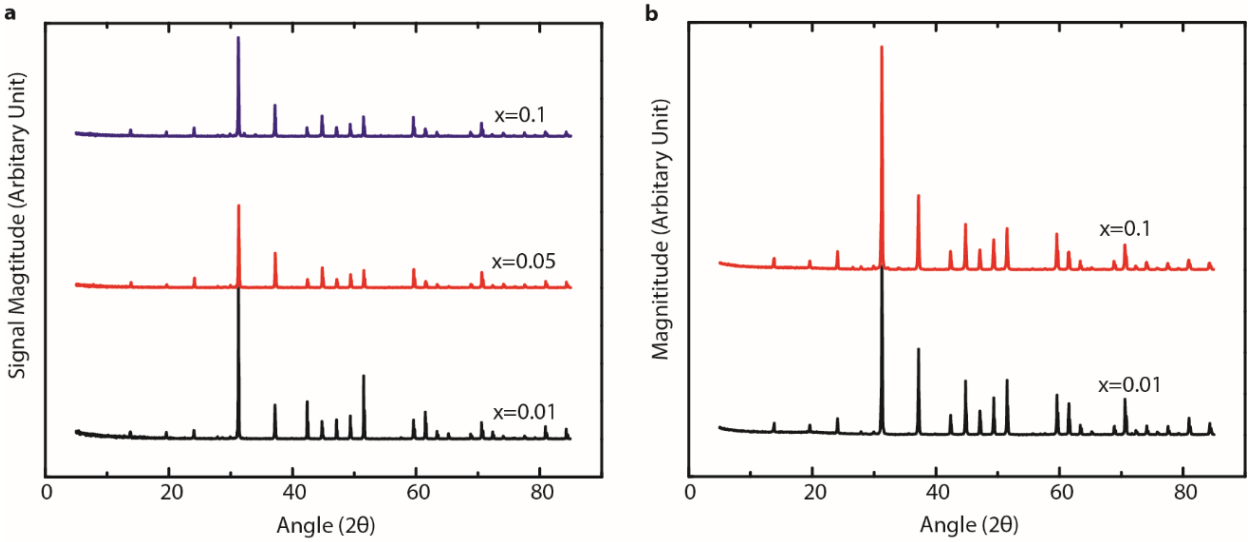

Figure 3.2 (a) Powder XRD patterns of three samples ($CoSb_{3-x}Sn_x$ with x=0.01, 0.05, and 0.1) before SPS. (b) Powder XRD patterns of two samples (with x=0.01 and 0.1) after SPS.

The results of the density and actual matrix elemental compositions are also included in Table 3.1 to show the quality of the polycrystalline (with micron-size grains) $CoSb_{3-x}Sn_x$ samples synthesized in this work. $CoSb_{3-x}Sn_x$ samples with x=0, 0.01, and 0.025 have densities only 92%

of the theoretical value that was calculated from the lattice parameter determined from the Rietveld analysis of the powder XRD results. Heavily doped samples (x=0.05, 0.1 and 0.15) exhibit larger densities in excess of 98%. Taken from at least 5 random positions selected within the matrix region for each sample, the results from Electron Microprobe Analysis (EMPA) reflect the actual composition of the matrix instead of the total composition that counts the sediments between the grains. The pure, lightly and moderately doped samples with x=0.01, 0.025, and 0.05 still exhibit an excess of Sb. This is consistent with the XRD observation of the Sb peak after SPS, indicating that the SPS process cannot eliminate the secondary phases that have already segregated in the matrix. The actual Sn concentration is lower than the nominal values for all of the samples, due to the unavoidable loss of Sn powder during the preparation process (similar to cobalt), evaporation during the melting process, and sedimentation of Sn between the grains. Yet, except for the x=0.15, the actual Sn concentration in solid solution increases with the nominal concentration x as expected.

More accurate phase information from backscattered electron microscopy (BSE) for three lightly and moderately doped samples (x=0.01, 0.05 and 0.1) is shown in Fig. 3.3a-c. Since BSE images are more sensitive for detecting secondary phases than SEM images, we used BSE instead of SEM to show the phase composition more accurately. In Fig. 3.3a, many dark spots were present, verifying that the low density of the lightly doped samples (x=0.01) was caused by severe porosity, which is also shown by SEM in Fig. 3.3d. Heavily doped samples (x=0.05 and 0.1) are much denser than the lightly doped ones as much fewer dark spots are present in Fig. 3.3b and Fig. 3.3c. Secondary phases with the size of approximately 50 μm (gray spots) in the heavily doped sample (x=0.1) were observed, which is consistent with the conclusion drawn from powder XRD that the solubility limit of Sn on Sb sites is below x=0.1. Similar gray spots

observed in the $CoSb_{2.9}Sn_{0.1}$ sample are barely visible in the $CoSb_{2.95}Sn_{0.05}$, suggesting that the solubility limit is still larger than x=0.05. I believe that the porosity of the lightly doped sample was due to the fact that the SPS condition used in this work was only optimized for high Sn concentration. This suggested explanation is consistent with a previous study using SPS for ceramics,[32] which also found that an additional low melting impurity (Sn in this case) can improve densification during SPS.

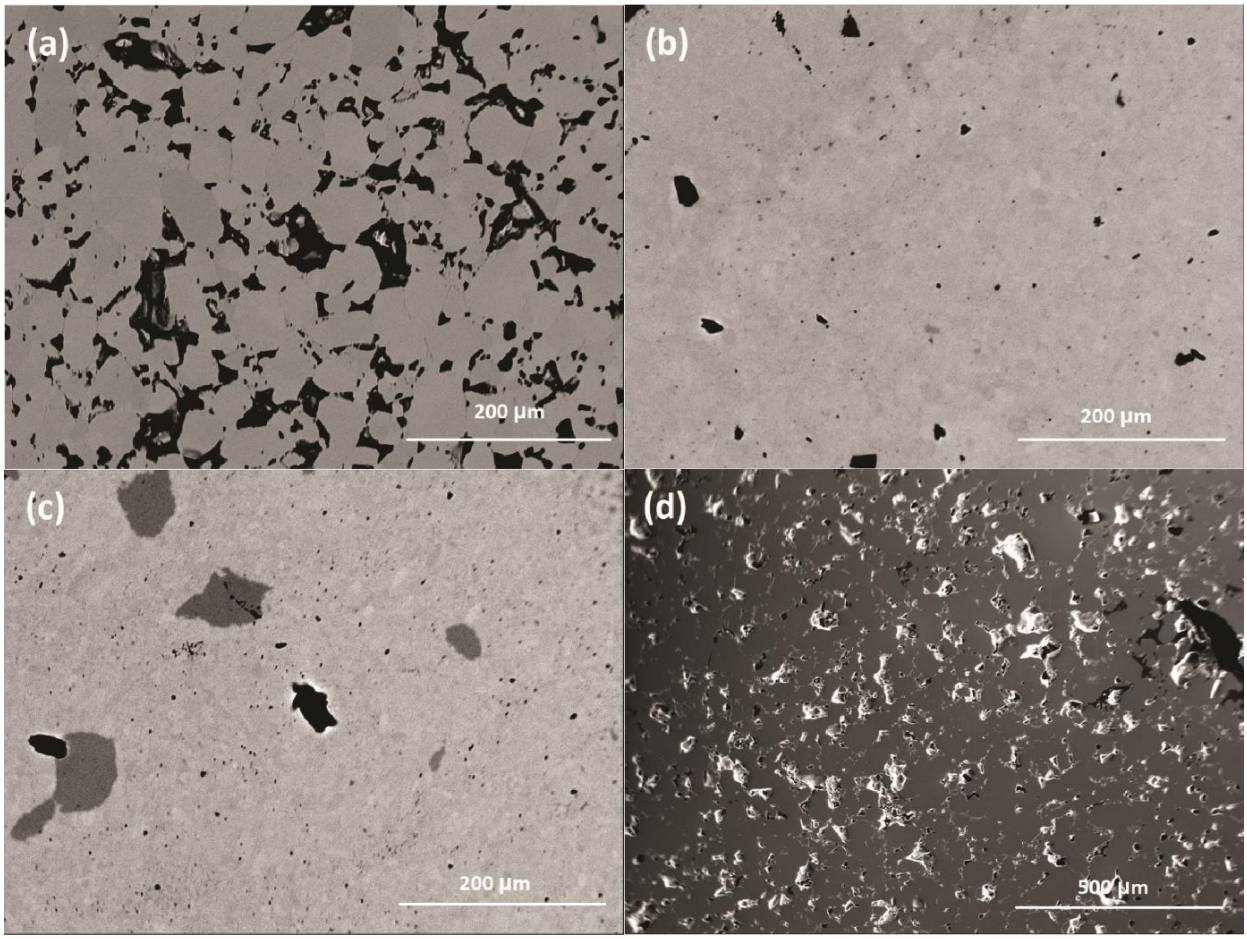

Figure 3.3 (a) BSE image of the x=0.01 sample. (b) BSE image of the x=0.05 sample. (c) BSE image of the x=0.1 sample. (d) SEM image of the x=0 sample.

Scanning transmission electron microscopy (STEM) images from three samples (x=0, 0.05 and 0.15) are shown in Fig. 3.4 to show finer microstructure down to nanometer scale. Energy dispersive x-ray spectroscopy (EDS) measurements in STEM identified Sb as a secondary phase at grain boundaries in the undoped sample, which further confirmed the results obtained from the powder XRD and EMPA. An example of one such inclusion is shown in Figure 3.4a. A small amount of Sn-rich inclusions was also observed at grain boundaries in the moderately doped sample (x=0.05) and heavily doped sample (x=0.15). These cannot be detected by either powder XRD due to its detection limit or BSE because of its limit in spatial resolution. These observations suggest that the solubility limit is close to x=0.05 and that the precipitation of a small amount of Sn or Sn-rich phase is due to local inhomogeneity. Analysis of diffractograms from high resolution high angle annular dark field STEM images obtained at several different orientations, an example of which is shown in Figure 3.4d, were consistent with SnO_2.[33] The presence of SnO_2 impurities explains why the Sn concentration of the x=0.15 sample is larger than that of the x=0.1 sample in the matrix, even though x=0.1 is already greater than the solubility limit. An imperfect vacuum during annealing or SPS likely caused the formation of the SnO_2 impurities.

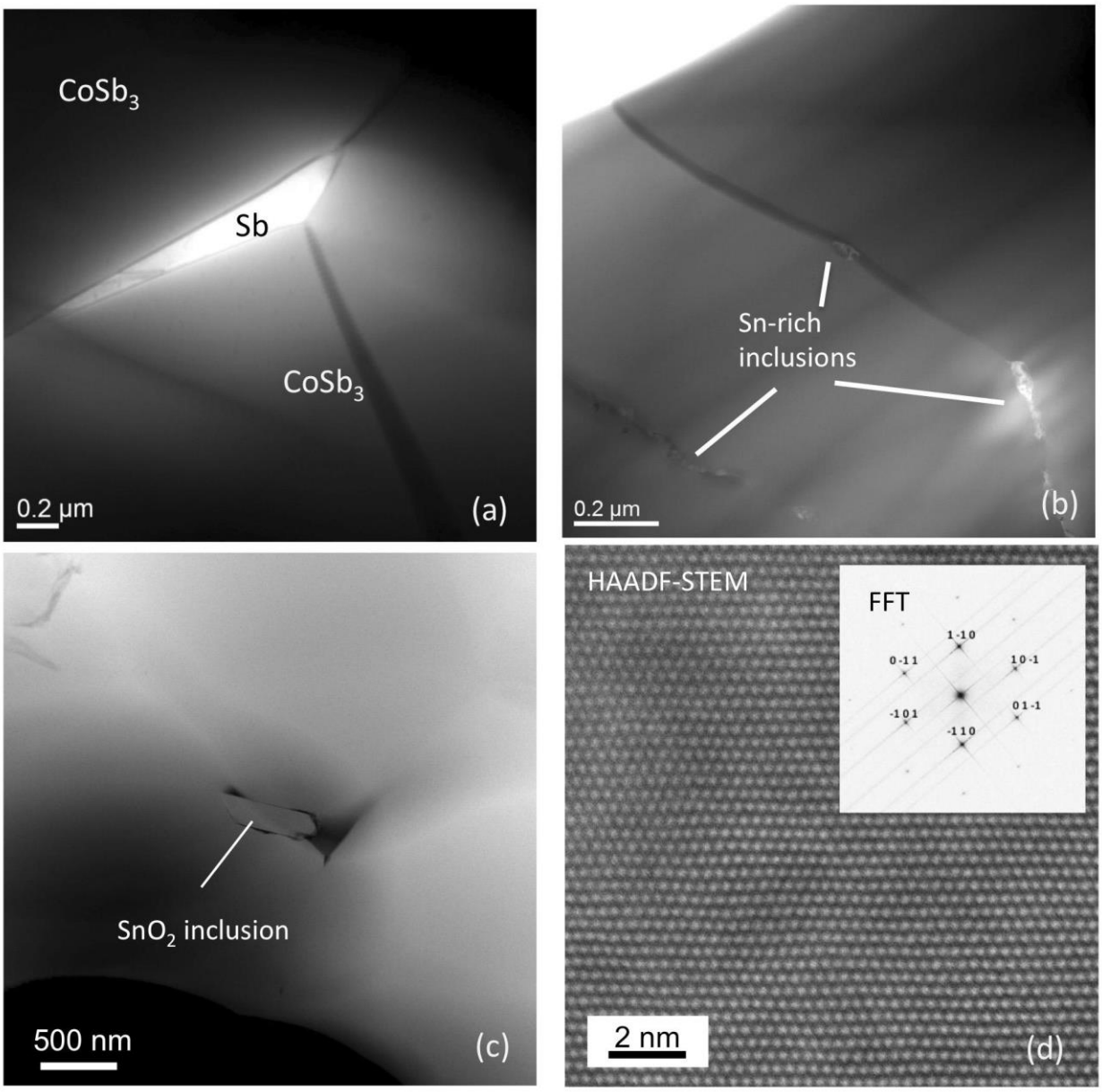

Figure 3.4 STEM analyses found the presence of some secondary phases localized to intergranular regions. (a) x=0 sample: example of Sb-rich intergranular phase. (b) x=0.05 and (c) x=0.15 samples show Sn-rich inclusions at grain-boundaries. (d) High resolution HAADF-STEM image of inclusion in (c). Inset shows diffractogram calculated from Fourier transform of STEM image. Spacings and angular relationships from this and other orientations identify the phase as SnO_2 (Cassiterite). The image in (d) is oriented along a [111] zone axis.

To summarize the structural characterization of the samples, I observed that the solubility limit for Sn is between x=0.05 and 0.1 for $CoSb_{3-x}Sn_x$, and probably more toward the lower end

of that range, as the TEM results suggest that the solubility limit is close to 0.05. This value falls within the range from 0.0045 reported by Zobrina et al.[34] to 0.3 reported by Kim et al.[35] and comparable to the value of 0.14 by Tobola et al.[36] Moderately doped samples were confirmed to be homogenous and dense, lightly doped samples were found to be porous and heavily doped samples were found to contain Sn-rich impurities.

3.5 Thermoelectric Properties

Before I move to the discussion of the thermoelectric transport properties, the possibility that the secondary phases observed in the previous chapter will influence the transport coefficients needs to be ruled out. Indeed, the type and size of the inclusions observed in Fig. 3.3 and Fig. 3.4 were not expected to affect the Seebeck coefficient of the samples significantly, which is the most sensitive probe of the presence of a resonant state. The thermoelectric properties of composites have been theoretically studied by Bergman and co-workers,[34,35] who showed that spherical or cube-like inclusions of a metallic phase with a low Seebeck coefficient in a matrix of a more insulating semiconductor material with a high Seebeck coefficient reduces the Seebeck coefficient only slightly at inclusion concentrations below the percolation limit. Experimentally[37] adding metallic silver ($S \sim +2$ μV/K at 300 K) into polycrystalline Bi ($S \sim -72$ μV/K at 300 K) reduces the absolute value of the Seebeck coefficient of the composite ($S \sim -60$ μV/K at 300 K) by only 15% when the Ag concentration is 40% by volume, and much less for the concentrations observed in Fig. 3.3. The electrical conductivity is expected to be linearly dependent on the volume percentage of the inclusions or pores, which can be seen to be small in

Fig. 3.3. So, we do not need to worry about the influence of the secondary phases on the Seebeck coefficient and electrical conductivity.

High temperature Hall measurement results for all samples are shown in Fig. 3.5. For a single band with only one type of carrier (here holes), the Hall coefficient can be expressed as:[38]

$$R_H = \frac{A}{pe} \qquad \textit{Equation 3.1}$$

where R_H is the Hall coefficient, p is the hole concentration, e is the elementary charge (of a hole), and A is the Hall factor, a parameter accounting for the anisotropy of the Fermi surface and the dominant scattering mechanism. The positive Hall coefficients of all samples and the greatly reduced Hall coefficients of the doped $CoSb_{3-x}Sn_x$ samples compared to pure $CoSb_3$ verify that Sn is an effective *p*-type dopant in $CoSb_3$. The Hall coefficient peaked at a certain temperature, presumably due to the interband excitation of minority electrons at high temperatures, and the peaks occur at progressively higher temperatures with increasing Sn content. An interesting feature of the Hall data for samples with $x>0$ is the rising magnitude of R_H from room temperature to a peak value between 673K and 773K. Under the assumption of $A = 1$ (valid for simple bands with parabolic band dispersion) in Eqn. 3.1, carrier concentration decreases as temperature increases. Because this is not physically reasonable, a more complex band dispersion is warranted. Singh and Pickett[8] have shown previously that the top of the valence band of $CoSb_3$ exhibits linear dispersion. Replacing parabolic band dispersion with a linearly dispersing valence band, the carrier concentration deduced from the Hall coefficient indeed rises with temperature at high temperatures, as shown in Fig. 3.5b, up to the temperature at which minority electrons are thermally excited and R_H decreases again.

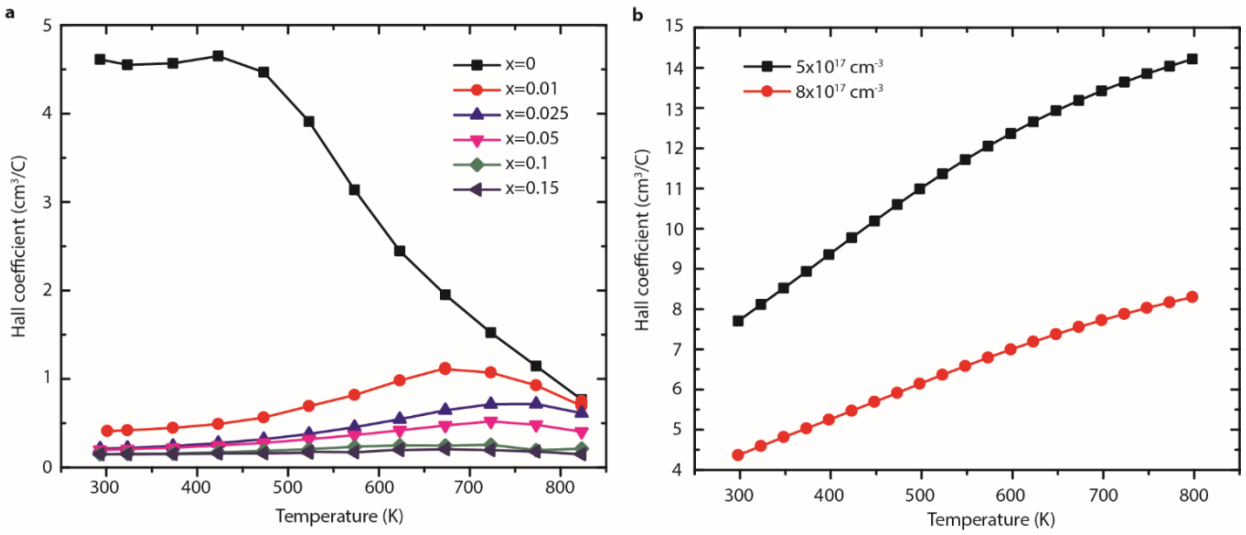

Figure 3.5 (a) Hall coefficients measured in all of the samples from room temperature to 800 K. The x values in the legend correspond to the Sn fraction in $CoSb_{3-x}Sn_x$. (b) The calculated temperature dependence of the Hall coefficient using a linearly dispersing valence band, assuming two constant carrier concentrations and a constant scattering parameter.

The Seebeck coefficient was measured over a wide temperature range from 300 K to 800 K, as shown in Fig. 3.6a-b. The positive Seebeck coefficient measured confirms hole conduction in all samples. At low temperatures before the onset of interband excitation, S increases with T, confirming that the samples are degenerately doped and have metallic behavior. At higher temperatures above the appearance of minority electron thermal excitation, a negative slope for dS/dT sets in at temperatures coinciding with the Hall coefficient peaks. For a degenerate carrier system, the Seebeck coefficient can be described by the Mott relation:[39]

$$S = -\frac{\pi^2}{3}\frac{k}{e}kT\left[dln\left(\mu g(E)\right)/dE\right]\Big|_{E=E_F} \qquad \textit{Equation 3.2}$$

where μ is the carrier mobility and $g(E)$ is the carrier density of states. If the term in brackets remains temperature-independent, the Seebeck coefficient is then expected to be linearly

dependent on temperature. This linear dependence was observed in the two most heavily doped samples (x=0.1 and 0.15) at high temperatures. Figure 3.6b shows that the Seebeck coefficients of the $CoSb_{3-x}Sn_x$ samples typically follow the conventional Pisarenko relation at low temperatures. The deviation from the conventional Pisarenko relation at high temperatures originate from the intrinsic excitation of the minor carriers in the lightly doped samples. The Pisarenko relation at low temperatures will also be discussed in detail later in this section.

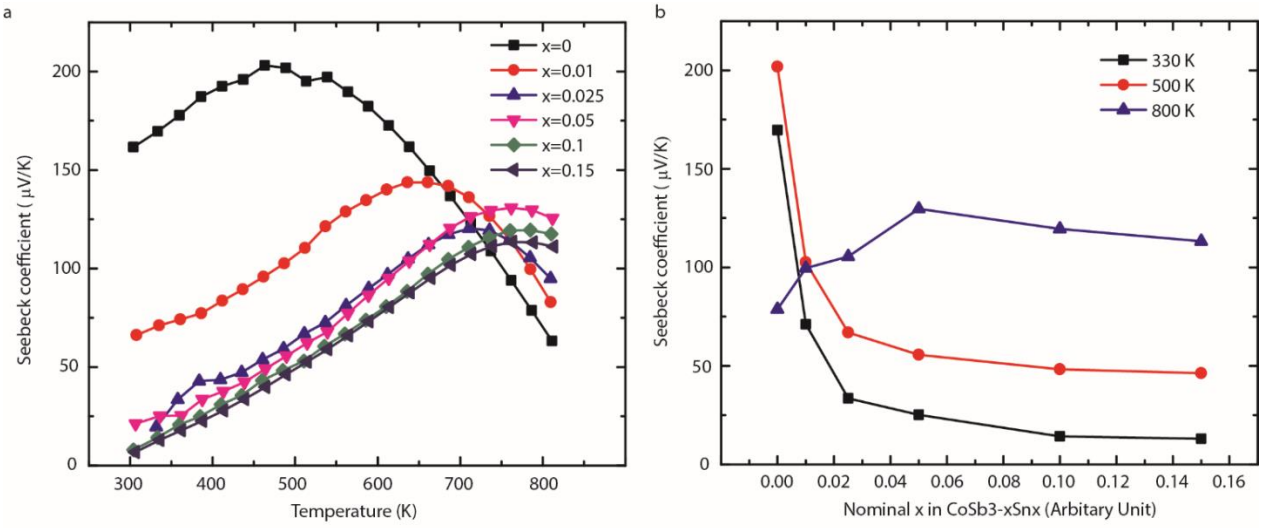

Figure 3.6 (a) Seebeck coefficients measured in all of the samples from room temperature to 800 K. The x values in the legend correspond to the Sn fraction in $CoSb_{3-x}Sn_x$. (b) Seebeck coefficients as a function of nominal Sn concentration x at 330 K, 560 K, and 800 K.

Electrical conductivity was measured from 300 K to 800 K, as shown in Fig. 3.7. The increase in hole concentration introduced by Sn dopants results in an enhanced electrical conductivity at room temperature. Electrical conductivity was observed to be highest for the x=0.025 sample and decreases with a further increase in Sn concentration beyond x=0.025 due to deterioration of carrier mobility. All Sn-doped samples exhibit a decreasing electrical

conductivity with temperature, reflecting metallic behavior. At high temperatures, all samples tend to converge to a similar value of approximately 375 S/cm.

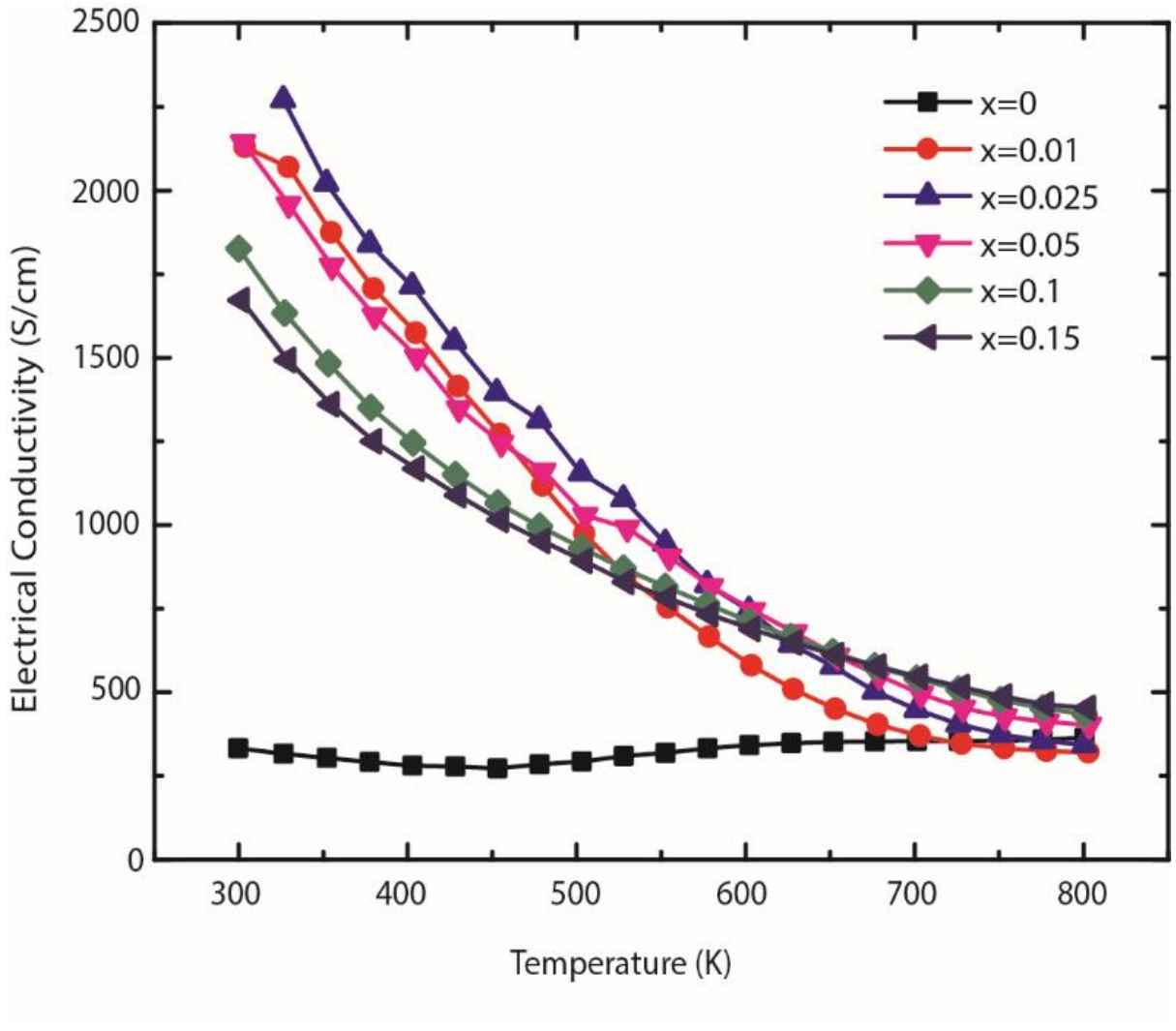

Figure 3.7 Electrical conductivity measured in all of the samples from room temperature to 800 K. The x values in the legend correspond to the Sn fraction in $CoSb_{3-x}Sn_x$.

The thermoelectric power factor ($S^2\sigma$) is shown in Fig. 3.8. Below 573 K, the highest power factor is achieved with pure $CoSb_3$, confirming that such binary compounds possess

excellent electrical properties. At higher temperatures (above 673 K), the best power factor is obtained for x=0.05, reaching a value of 9 $\mu Wcm^{-1}K^{-2}$, due to the carrier concentration enhancement with the introduction of Sn dopants.

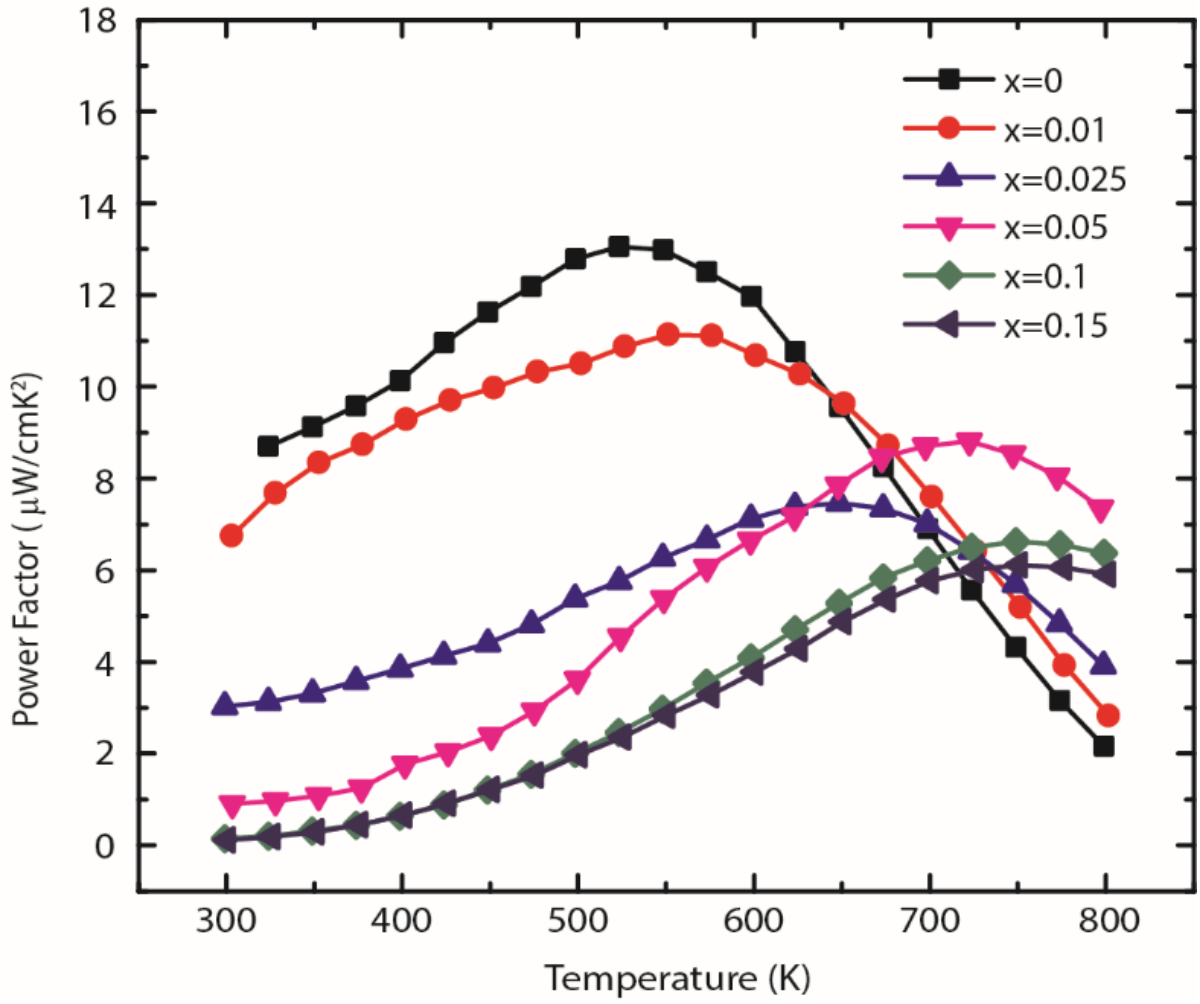

Figure 3.8 Power factor from room temperature to 800 K. The x values in the legend correspond to the Sn fraction in $CoSb_{3-x}Sn_x$.

A Pisarenko plot, which illustrates the relationship between Seebeck coefficient and carrier concentration, is shown in Fig. 3.9 to determine whether or not any improvement in the

Seebeck coefficient due to the presence of band resonant states is realized. If the parabolic band structure is not altered (no resonant levels present near Fermi level), the relationship between Seebeck coefficient and carrier concentration should simply follow the solid line of *S(p)* plotted in Fig. 3.9, which is calculated using:[9]

$$S = \left(\frac{2\pi k_B^2 T}{3ea}\right)\left(\frac{\pi}{3p}\right)^{\frac{1}{3}} \qquad \textit{Equation 3.3}$$

Unfortunately, at room temperature and above, no significant improvement due to the presence of resonant impurity levels can be observed. The experimental data points generally lie on the calculated solid line without any distortion.

We now show that our experimental findings are consistent with the theory, and no enhancement of the Seebeck coefficient was observed because the Fermi energy simply never reaches the valence band distortion predicted in Fig. 3.1, because the solubility limit of Sn precludes the introduction of more carriers.

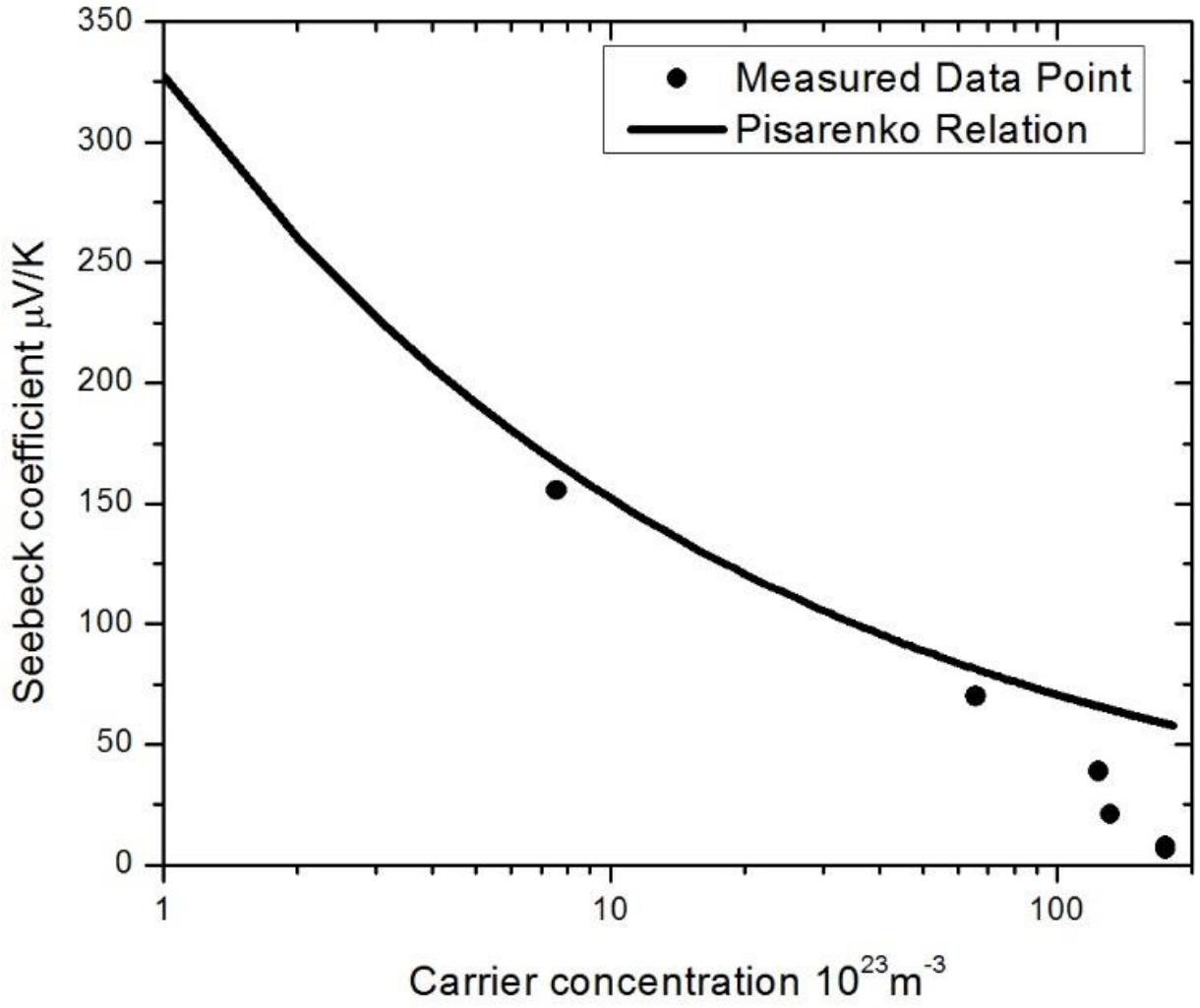

Figure 3.9 Measured data points compared to the Pisarenko relation at room temperature.

In order to calculate the Fermi energy E_F (with respect to the valence band edge) from the Hall carrier concentration, we assume a linear band dispersion and primarily acoustic phonon scattering at room temperature. We write the Hall coefficient by solving the Boltzmann transport equation within the relaxation time approximation as:

$$R = \frac{3}{[1+exp(-\eta^*)]\frac{9}{4}q(kT)^3F_{1/2}^2(\eta^*)\frac{\pi}{(\pi a)^3}} \qquad \textit{Equation 3.4}$$

where $\eta^* = {E_F}/{kT}$ is the reduced Fermi level, $F_j(x)$ is the j-th order Fermi integral and a is the proportionality constant of the linear band dispersion $E = a|\vec{k}|$ with a value of 3.1eVÅ from the literature.[9] From the Hall coefficient, we can calculate E_F for various samples at room temperature and then calculate the carrier concentration through the equation I derived:

$$p = \frac{\pi}{(\pi a)^3}(kT)^3 F_2(\eta^*) \qquad \textit{Equation 3.5}$$

The results are shown in Fig. 3.10. Here, the energy of holes increases as they move deeper into the valence band, and so does Fermi level. It is obvious that as the Sn concentration increases, the Fermi level is pushed deeper into the valence band, and reaches E_F = 0.3 eV for the most heavily doped samples. This should have been sufficient to observe the effect of Sn as a resonant level according to Fig. 3.1. It is possible that the overestimation of the Fermi level assuming only one linear band over the whole energy range in all the model calculations is such that the resonant levels are much deeper, and in the end, it is impossible to add enough Sn in solid solution into the Sb sites of $CoSb_3$ to enhance the Seebeck coefficient at high temperature. Indeed, the fact that the Fermi level does not change when the Sn concentration increases from 0.1 to 0.15 suggests that the solubility limit of Sn in $CoSb_3$ is less than x=0.1, consistent with the microscopy data in Figs 3.3 and 3.4 and indicative of the inability to further push down the Fermi level.

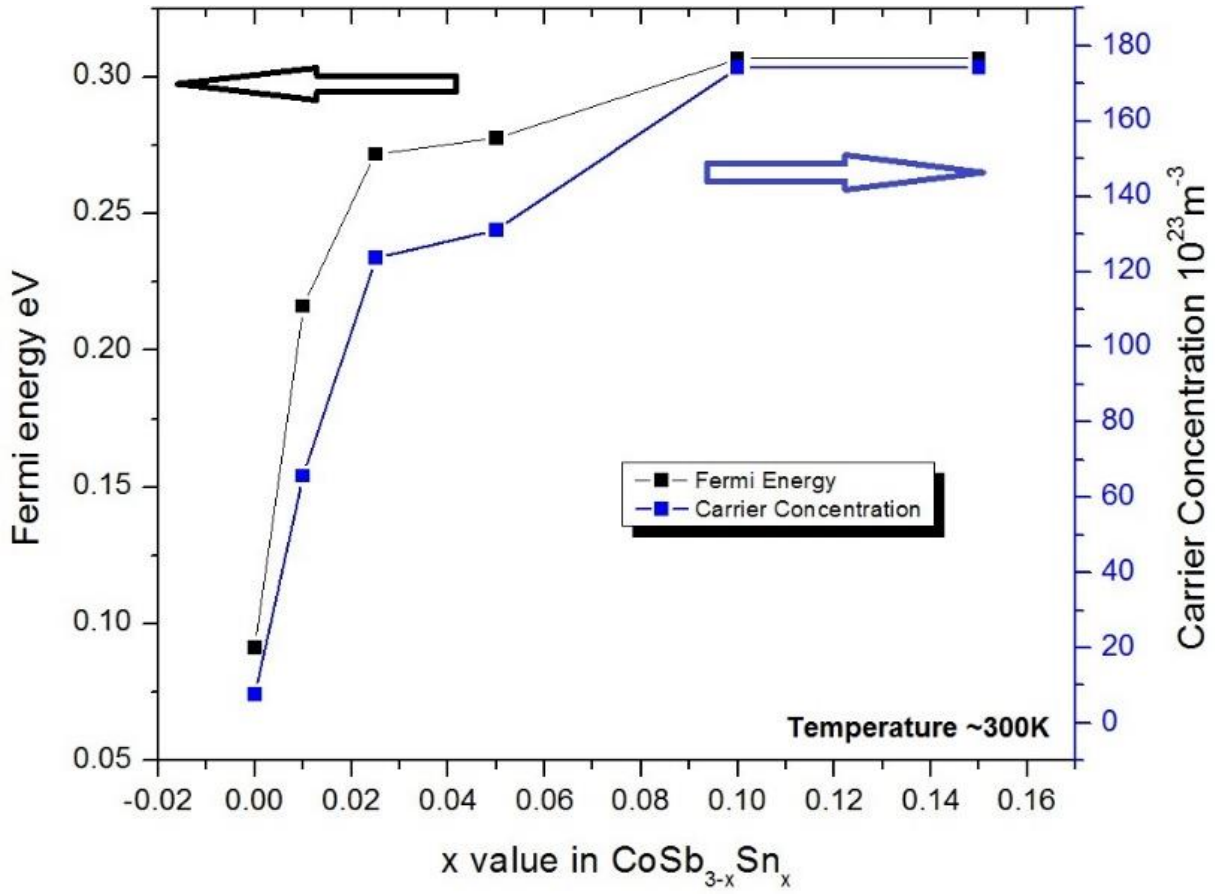

Figure 3.10 Fermi energy and carrier concentration as a function of x in $CoSb_{3-x}Sn_x$.

Thermal conductivity data above room temperature, presented in Fig. 3.11a, exhibit a decrease as Sn dopant concentration increases. The lowest room-temperature thermal conductivity of approximately 2 W/m-K was achieved in the most heavily doped sample (x=0.15), presumably due to strong impurity scattering of acoustic phonons. The temperature dependence of the thermal conductivity is indicative of Umklapp scattering. A slight upturn in the high-temperature thermal conductivity (T>770 K) is likely due to an electronic contribution from the onset of the minority electrons, which also contributes to downturns in the Seebeck coefficient and Hall coefficient. Using the Wiedemann-Franz law (with a fully degenerate value of the Lorenz number of 2.44×10^{-8} $W\Omega K^{-2}$) to approximately separate the electronic and lattice

contributions to thermal conductivity, the lattice contribution is plotted in Fig. 3.11b. The fact that this value does not decrease monotonically with temperature is an indication that the assumption of a constant Lorenz number was only very approximate, and it does not account for a bipolar contribution one might expect in the presence of minority electrons. The lattice thermal conductivity is reduced quite effectively by Sn dopants; at room temperature, the samples with highest Sn doping have a lattice thermal conductivity that is lower than that of pure $CoSb_3$ by a factor of more than five. Because Sn and Sb are neighboring elements in the periodic table and their atomic masses (118.69 for Sn and 121.75 for Sb) are similar, it is unlikely that this arises from alloy scattering alone. Rather, Sn may also be filling voids in the crystal structure and scatter acoustic phonons by rattling. The filler (Sn in voids) together with the dopant (Sn substituting for Sb) may also cause a change in the temperature dependence of the lattice thermal conductivity from negative to temperature-independence, as has also been observed elsewhere (Yb filler together with Sn dopant).[40] However, the fraction of Sn dopants that acts as fillers is believed to be small, since it does not influence electronic transport as dramatically as thermal transport.

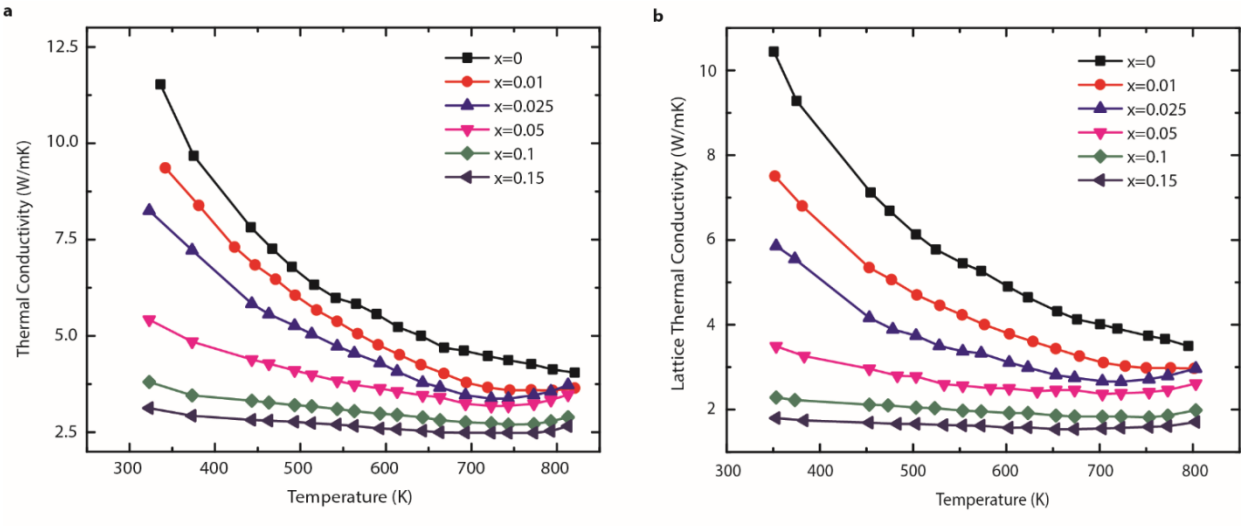

Figure 3.11 (a) Total thermal conductivity from room temperature to 825 K. The x values in the legend correspond to the Sn fraction in $CoSb_{3-x}Sn_x$. (b) Lattice thermal conductivity from room temperature to 825 K derived by subtracting the electronic thermal conductivity (approximated using the Wiedemann-Franz law) from the total measured thermal conductivity. x values in the legend correspond to the Sn fraction in $CoSb_{3-x}Sn_x$.

Calculated ZT values are shown in Fig. 3.12. The highest ZT (~0.2) was achieved for the x=0.05 sample at 723 K. Improvements in ZT arise primarily from reductions in thermal conductivity rather than improvements in power factor.

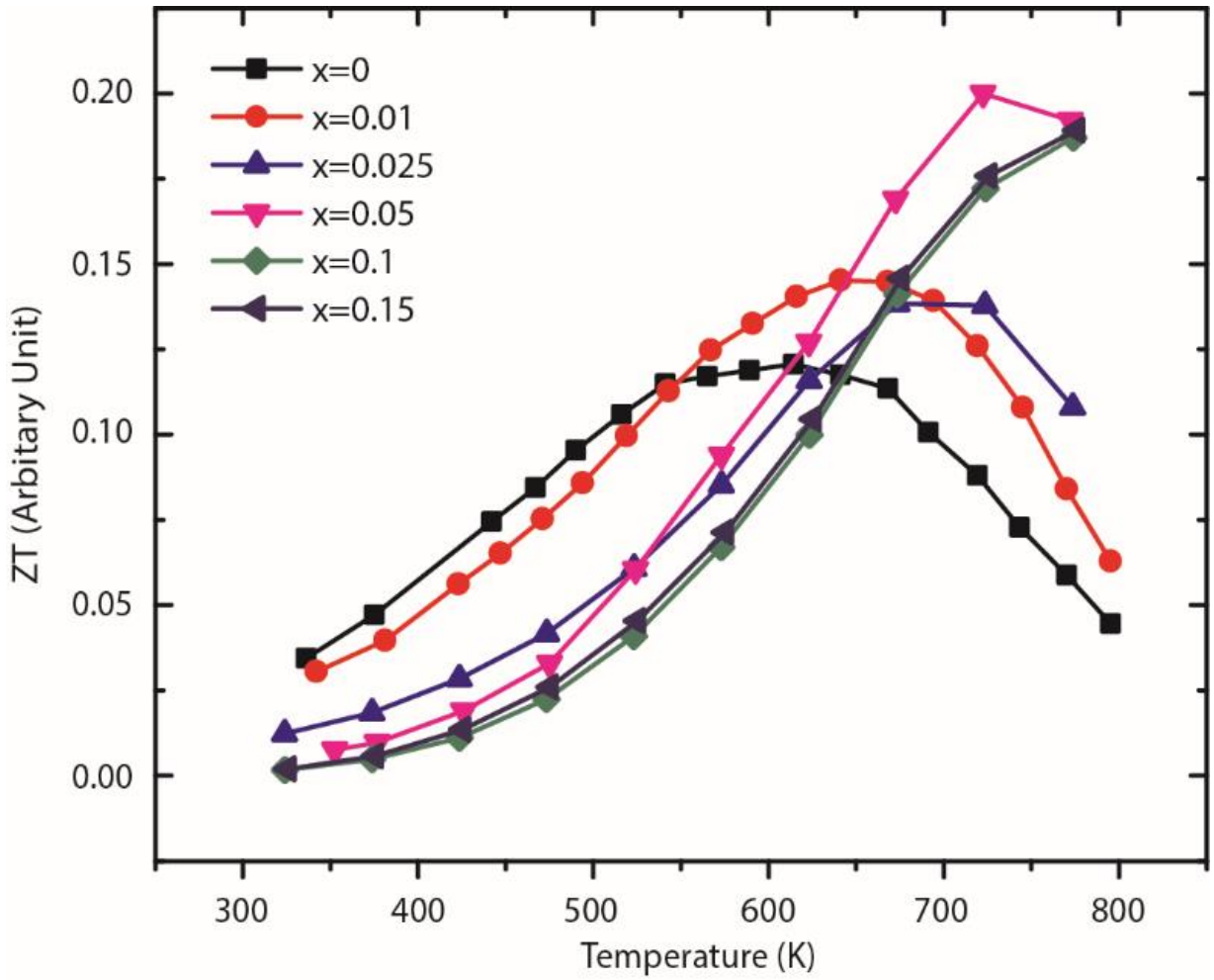

Figure 3.12 ZT values from room temperature to 800 K. x values in the legend correspond to the Sn fraction in $CoSb_{3-x}Sn_x$.

3.6 Summary

By using spark plasma synthesis, I successfully made Sn-doped $CoSb_{3-x}Sn_x$ materials with various *x* values. The solubility limit was determined to be x≈0.05. Based on transport measurements and calculations, I did not observe any significant evidence of band resonant states in Sn-doped $CoSb_3$ within the dopant concentration range explored. I explained this by the fact that the Sn solubility limit is too low to achieve the hole concentration levels needed to put

the Fermi level near the Sn resonant state as calculated *ab-initio*. As a consequence, the figure of merit was enhanced only slightly; this enhancement is primarily due to a reduction in thermal conductivity potentially caused by a small portion of Sn filling voids in the crystal structure. My study indicates that the doping limit of Sn in $CoSb_3$ is below 2% and that the synthesis of samples with very low Sn concentrations is difficult because of porosity and inhomogeneous dopant distribution. Other approaches to enhance the thermoelectric properties in *p*-type skutterudites are desired.

Chapter 4 Thermoelectric Properties of *p*-type Filled Skutterudites $Yb_zFe_yCo_{4-y}Sb_{12-x}Sn_x$

4.1 Background

In Chapter 3, I have shown by both calculation and experiment that low solubility of Sn dopants on Sb sites in $CoSb_3$ is not capable of introducing enough charge carriers to push the Fermi level deep into the valence band to the vicinity of the generated resonant levels. A straightforward approach to solve such problem is to further push the Fermi level by introducing a second *p*-type dopant. The solubility limit of a second *p*-type dopant on Sb sites is likely to be low, and thus incorporating Fe on Co sites is selected. Indeed, numerous previous work indicates that Fe is able to substitute all Co, though adding interstitial fillers is required for stabilizing the crystal structure.[41, 42] In this chapter, Yb was selected as the filler and Fermi level is tuned by varying both Yb and Fe concentrations. Sn concentration is fixed at ~1%. In addition to experiments, numerical thermoelectric transport coefficient fitting is attempted. Thermoelectric measurements suggest that substituting Co by Fe is able to increase the carrier concentration; however, the Fermi level is still pinned above the energy vicinity of the generated resonant states by Sn. Such Fermi level pinning is caused by the moving Fe heavy band as the Fe concentration increases. Though transport coefficient fitting fails probably due to the unknown temperature dependence of the scattering processes, I am still able to conclude that the convergence of the

Fe-d band and the Sb-p band is beneficial for thermoelectric performance. An approach to further improve the thermoelectric performance of *p*-type filled skutterudites is also proposed.

4.2 Materials Synthesis and Pellets Sintering

Ytterbium (99%, Alfa Aesar), iron (99.98%, Alfa Aesar), cobalt (99.98%, Alfa Aesar), antimony (99.9999%, Alfa Aesar), and tin (99.9999% Alfa Aesar) elements were weighed based on the chemical formula of 6 various compositions: $Yb_{0.3}FeCo_3Sb_{12}$, $Yb_{0.3}FeCo_3Sb_{11.9}Sn_{0.1}$, $Yb_{0.6}Fe_2Co_2Sb_{12}$, $Yb_{0.6}Fe_2Co_2Sb_{11.9}Sn_{0.1}$, $Yb_{0.8}Fe_3CoSb_{12}$, and $Yb_{0.8}Fe_3CoSb_{11.9}Sn_{0.1}$ in the glovebox. The reason I selected these 6 particular compositions will be discussed in the following sections. The weighed elements are then mixed and sealed in the evacuated quartz tubes. The mixed raw elements are heated up to 1373 K at a rate of 0.5 K/min, held at 1373 K for 6 hours, and then quenched in cold salt water. The quenched ingots were then sealed again in quartz tubes and annealed at 923 K for 4 days. Following annealing, the as-cast ingots were hand-ground to powders, after which SPS was performed under 50 MPa pressure and 873 K temperature for ~15 min.

4.3 Crystallographic and Microstructural Characterization

Powder XRD patterns of 6 $Yb_zFe_{4-y}Co_ySb_{12-x}Sn_x$ samples are shown in Fig. 4.1. The major phase is identified as skutterudite with minor secondary phases identified as $FeSb_2$, Yb_2O_3,

and Sb. The existence of the secondary phases in *p*-type filled skutterudites seems unavoidable and these microscale secondary phases do not influence the thermoelectric properties much.[40-43] The measured density, actual elemental composition of the matrix, lattice parameters determined by the Rietveld analysis of the powder XRD patterns, and the calculated carrier concentration for the nominal composition of $Yb_zFe_{4-y}Co_ySb_{12-x}Sn_x$ are listed in Table 4.1. The valence state of Yb is taken to be 2.62 in filled skutterudites.[44] All samples are well densified and have densities greater than 94% of the theoretical value. The actual elemental composition only deviates slightly from the nominal value, probably due to the unavoidable oxidation of the elements or segregation of the secondary phases. The lattice parameter increases with Yb and Fe concentration, caused by the larger Fe ionic radius with respect to Co and the interstitial Yb incorporation. The effect of Sn dopants on the lattice parameter is observed to be negligible. The calculated carrier concentration from the nominal composition shows that the carrier concentration increases as the Fe concentration increases.

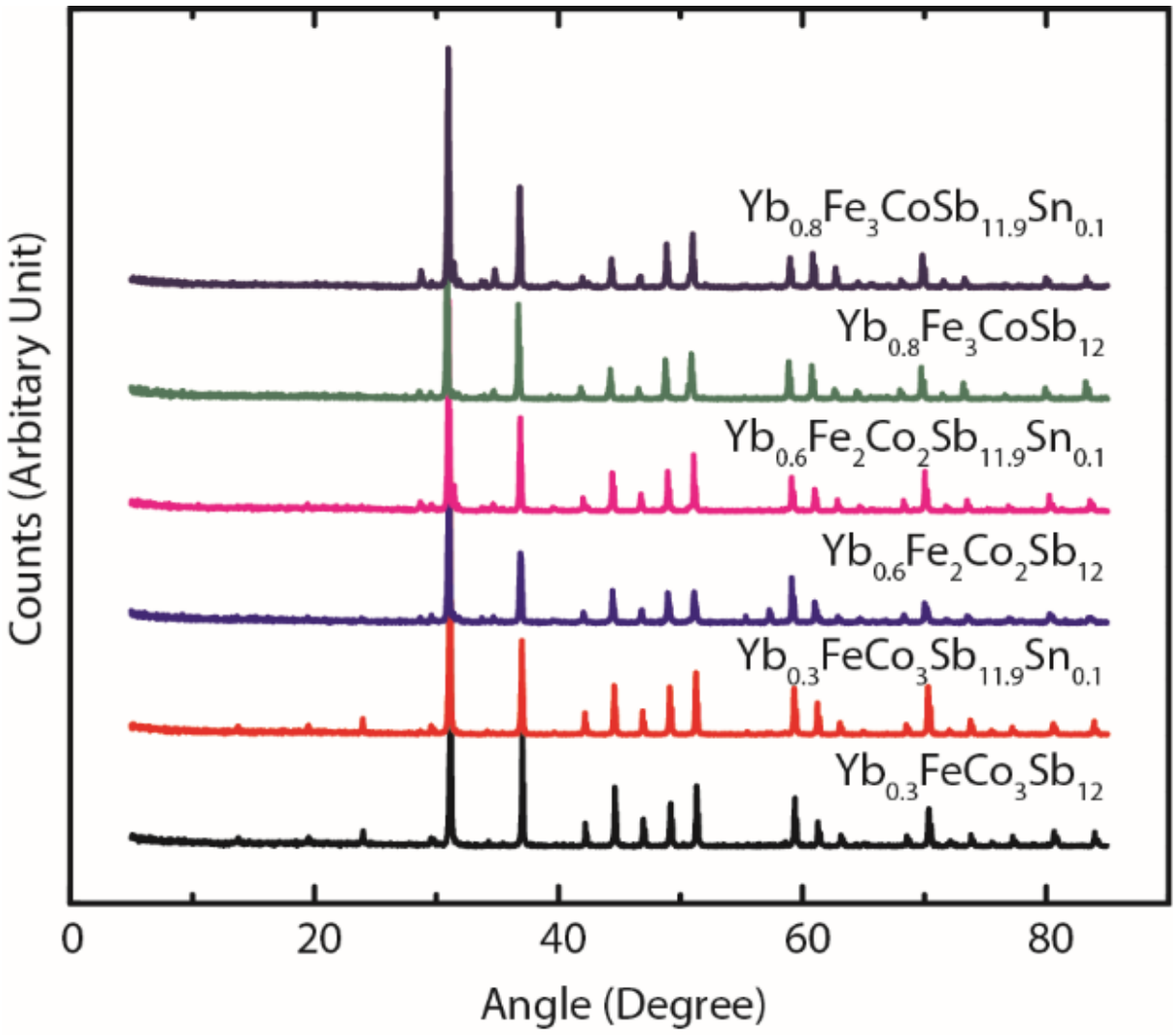

Figure 4.1 Powder XRD results of all the skutterudite samples from 5^o to 85^o. Secondary phases in the skutterudites samples can be identified by comparing the powder XRD results of the samples to the powder XRD patterns of the references

Nominal Composition	Density (g/cm^3)	Actual matrix composition	Lattice parameter (Å)	Estimated carrier concentration based on nominal composition(cm^{-3})
$Yb_{0.3}FeCo_3Sb_{12}$	7.55	$Yb_{0.23}Fe_{1.03}Co_{2.99}Sb_{12}$	9.068	5.740×10^{20}
$Yb_{0.3}FeCo_3Sb_{11..9}Sn_{0.1}$	7.59	$Yb_{0.21}Fe_{0.94}Co_{3.05}Sb_{11.9}Sn_{0.07}$	9.073	8.408×10^{20}
$Yb_{0.6}Fe_2Co_2Sb_{12}$	7.36	$Yb_{0.59}Fe_{2.00}Co_{2.04}Sb_{12}$	9.102	1.135×10^{21}
$Yb_{0.6}Fe_2Co_2Sb_{11.9}Sn_{0.1}$	7.84	$Yb_{0.55}Fe_{1.80}Co_{2.18}Sb_{11.9}Sn_{0.06}$	9.101	1.401×10^{21}
$Yb_{0.8}Fe_3CoSb_{12}$	7.50	$Yb_{0.84}Fe_{3.02}Co_{1.03}Sb_{12}$	9.140	2.368×10^{21}
$Yb_{0.8}Fe_3CoSb_{11.9}Sn_{0.1}$	7.69	$Yb_{0.84}Fe_{2.80}Co_{1.18}Sb_{11.9}Sn_{0.03}$	9.124	2.644×10^{21}

Table 4.1 Nominal composition, density measured by Archimedes method, actual matrix composition measured by electron microprobe analyzer (EMPA), lattice parameters calculated from the Rietveld analysis of the powder XRD data, and estimated carrier concentration calculated from the nominal composition.

4.4 Transport Fitting Theory

Ab initio band structure calculation results reported by Yang et al. suggest that three valence bands contribute to the hole conduction in *p*-type filled skutterudites $Yb_zFe_{4-y}Co_ySb_{12}$.[45] The three valence bands include a light non-parabolic Sb-p band and a heavy parabolic Fe-d band with both of their energy maximums located at Γ point, and another light parabolic band with its energy extreme located between H and N points. Electrical transport coefficients of each band will be derived in this section. The total transport coefficients will then be calculated from the contribution of each band.

For the light Sb-p band, the band dispersion relation is described by the Kane model:[46]

$$\frac{\hbar^2 k^2}{2m_{v1}^*} = E(1+\alpha E) \qquad \textit{Equation 4.1}$$

where ħ is the reduced Planck constant. k is the wave vector, m_{v1}^* is its effective mass, E is the energy, and α is the nonparabolicity parameter. The electrical transport coefficients can be written as:[46-48]

$$\sigma_{v1} = \frac{e^2}{3\pi^2}\frac{2(2m_{v1}^*)^{\frac{1}{2}}}{\hbar^3}\int_0^\infty \left(-\frac{\partial f_0}{\partial E}\right)\tau_{totalv1}(E+\alpha E^2)^{3/2}(1+2\alpha E)^{-1}dE \qquad \textit{Equation 4.2}$$

$$S_{v1} = \frac{1}{eT}\left[\frac{\int_0^\infty\left(-\frac{\partial f_0}{\partial E}\right)\tau_{totalv1}E\left(E+\alpha E^2\right)^{3/2}(1+2\alpha E)^{-1}dE}{\int_0^\infty\left(-\frac{\partial f_0}{\partial E}\right)\tau_{totalv1}(E+\alpha E^2)^{3/2}(1+2\alpha E)^{-1}dE} + E_F\right] \qquad \textit{Equation 4.3}$$

$$R_{Hv1} = \frac{\int_0^\infty\left(-\frac{\partial f_0}{\partial z}\right)\tau_{totalv1}^2\left(z+\beta z^2\right)^{3/2}(1+2\beta z)^{-2}dz\int_0^\infty\left(-\frac{\partial f_0}{\partial z}\right)\left(z+\beta z^2\right)^{3/2}dz}{\left[\int_0^\infty\left(-\frac{\partial f_0}{\partial z}\right)\tau_{totalv1}(z+\beta z^2)^{3/2}(1+2\beta z)^{-1}dz\right]^2 ep_{v1}} \qquad \textit{Equation 4.4}$$

where f_0 is the Fermi distribution function, $\tau_{totalv1}$ is the total relaxation time of Sb-p band, $\beta = \alpha k_B T$, $z = \frac{E}{k_B T}$, and p_{v1} is the carrier concentration of Sb-p band. Various scattering processes contribute to the total relaxation time obeying Matthiessen's rule as:[46]

$$\frac{1}{\tau_{total}} = \frac{1}{\tau_{ac}} + \frac{1}{\tau_{npo}} + \frac{1}{\tau_{po}} + \frac{1}{\tau_{imp}} + \frac{1}{\tau_{iv}} \qquad \textit{Equation 4.5}$$

in which τ_{ac}, τ_{npo}, τ_{po}, τ_{imp}, and τ_{iv} are the relaxation times of acoustic phonon scattering, nonpolar optical phonon scattering, polar optical phonon scattering, ionized impurities scattering, and the intervalley transition scattering. The intervalley transition scattering can be broken down into two parts as:

$$\frac{1}{\tau_{iv}} = \frac{1}{\tau_{iv12}} + \frac{1}{\tau_{iv13}} \qquad \textit{Equation 4.6}$$

where τ_{iv12} and τ_{iv13} account for intervalley transitions between the Sb-p band and the Fe-d band and between the Sb-p band and the light H-N band, respectively. The detailed expressions for the relaxation time of various scattering processes are:[46-49]

$$\frac{1}{\tau_{ac}} = \frac{(2m_{v1})^{3/2}E_{acv1}^2 k_B T}{2\pi\hbar^4 \rho v_l^2}(E+\alpha E^2)^{1/2}(1+2\alpha E)F_{ac} \qquad \textit{Equation 4.7}$$

$$\frac{1}{\tau_{po}} = \frac{e^2}{4\pi}\frac{(2m_{v1})^{1/2}k_B T}{\hbar^2}\left(\frac{1}{\varepsilon_\infty}-\frac{1}{\varepsilon_s}\right)\frac{1+2\alpha E}{(E+\alpha E^2)^{1/2}}F_{po} \qquad \textit{Equation 4.8}$$

$$\frac{1}{\tau_{imp}} = \frac{\pi N_{imp}}{(2m_{v1})^{1/2}}\left(\frac{e^2}{4\pi\varepsilon_s}\right)^2\frac{1+2\alpha E}{(E+\alpha E^2)^{3/2}}F_{imp} \qquad \textit{Equation 4.9}$$

$$\frac{1}{\tau_{npo}} = \frac{1}{2}\left(\frac{E_{npo}}{E_{acv1}}\right)^2\frac{\theta_D}{T}\left(e^{\theta_D/T}-1\right)^{-1}\times\left[\left(1+\frac{k_B\theta_D}{E}\right)^{1/2}+e^{\theta_D/T}\left(1-\frac{k_B\theta_D}{E}\right)^{1/2}\right]\frac{1}{\tau_{ac}} \qquad \textit{Equation 4.10}$$

$$\frac{1}{\tau_{iv12}} = \frac{M_{v2}}{2}\left(\frac{m_{v2}}{m_{v1}}\right)^{3/2}\left(\frac{E_{iv}}{E_{acv1}}\right)^2\frac{\theta_{iv}}{T}\frac{1}{exp(\theta_{iv}/T)-1}\times\left[\left(1+\frac{k_B\theta_{iv}}{E}\right)^{1/2}+exp(\theta_{iv}/T)\left(1-\frac{k_B\theta_{iv}}{E}\right)^{1/2}\right]\frac{1}{\tau_{ac}}$$

Equation 4.11

where E_{acv1} is the acoustic-phonon deformation potential of Sb-p band, ρ is the density, v_l is the sound velocity of longitudinal acoustic phonons, ε_∞ is the high frequency dielectric constant, ε_s is the static dielectric constant, N_{imp} is the concentration of ionized impurities, E_{npo} is the nonpolar optical phonon deformation potential, θ_D is the Debye temperature, $k_B\theta_{iv} = \hbar\omega_{iv}$ with ω_{iv} being the phonon angular frequency, E_{iv} is the intervalley transition deformation potential, F_{ac}, F_{po}, and F_{imp} are the functions of E defined by Zawadzki.[49] The electrical transport coefficients shown above can easily be extended to parabolic bands (Fe-d band and light H-N band in this work) by setting the nonparabolicity parameter to be zero. θ_{iv} can be assumed to be approximately equal to the Debye temperature.[46]

The charge carrier concentration of the non-parabolic Sb-p band is expressed as:[46]

$$p_{v1} = 2\left(\frac{m_{v1}k_BT}{2\pi\hbar^2}\right)^{3/2}\frac{4}{3\sqrt{\pi}}{}^{0}L_0^{3/2}(\eta,\beta) \qquad \textit{Equation 4.12}$$

where ${}^{n}L_k^m(\eta,\beta)$ is the generalized Fermi-Dirac integral defined as:[46]

$${}^{n}L_k^m(\eta,\beta) = \int_0^\infty(-\partial f_0/\partial z)z^n(z+\beta z^2)^m(1+2\beta z)^k dz \qquad \textit{Equation 4.13}$$

For the Fe-d and light H-N parabolic bands, the charge carrier concentration is:[38]

$$p_{v2,v3} = 2\left(\frac{2\pi m_{v2,v3}k_BT}{h^2}\right)^{3/2}F_{1/2}\left(\frac{E_F-E_{g2,g3}}{k_BT}\right) \qquad \textit{Equation 4.14}$$

where $F_j(\eta) = \int_0^\infty \frac{\eta^j}{1+\exp(\eta-\eta^*)}d\eta$ is the Fermi integral of j-th order. E_{g2} and E_{g3} are the energies at the top of the Fe-d band and the light H-N band with respect to the energy at the top of the Sb-p band.

Because $Yb_zFe_{4-y}Co_ySb_{12-x}Sn_x$ samples are degenerate *p*-type semiconductors, the contribution of conduction bands is negligible. Thus, the charge neutrality condition is:

$$p_{v1} + p_{v2} + p_{v3} = N_A \qquad \textit{Equation 4.15}$$

where N_A is the concentration of the *p*-type dopants. The total electric transport coefficients can be written as:[38]

$$\sigma = \sigma_{v1} + \sigma_{v2} + \sigma_{v3} = e(n_{v1}\mu_{v1} + n_{v2}\mu_{v2} + n_{v3}\mu_{v3}) \qquad \textit{Equation 4.16}$$

$$R_H = \frac{R_{Hv1}\sigma_{v1}^2 + R_{Hv2}\sigma_{v2}^2 + R_{Hv3}\sigma_{v3}^2}{\sigma^2} \qquad \textit{Equation 4.17}$$

$$S = \frac{(\sigma_{v1}S_{v1} + \sigma_{v2}S_{v2} + \sigma_{v3}S_{v3})}{\sigma} \qquad \textit{Equation 4.18}$$

4.5 Thermoelectric Transport Properties

Actual carrier concentration at room temperature can be derived from Hall coefficient measurement as:

$$p = \frac{A}{eR_H} \qquad \textit{Equation 4.19}$$

where A is a numerical proportionality factor, which depends on the band structure and the scattering processes. In this chapter, we set A to be 1 for a rough estimation.[38] The estimated actual room temperature carrier concentrations and high temperature Hall coefficients of 6 $Yb_zFe_{4-y}Co_ySb_{12-x}Sn_x$ samples are shown in Fig. 4.2. The results confirm that varying Yb and Fe concentration effectively tunes the charge carrier concentration, except for slight deviations from the expected trend shown in the estimated carrier concentration probably caused by the formation of the defects or secondary phases.

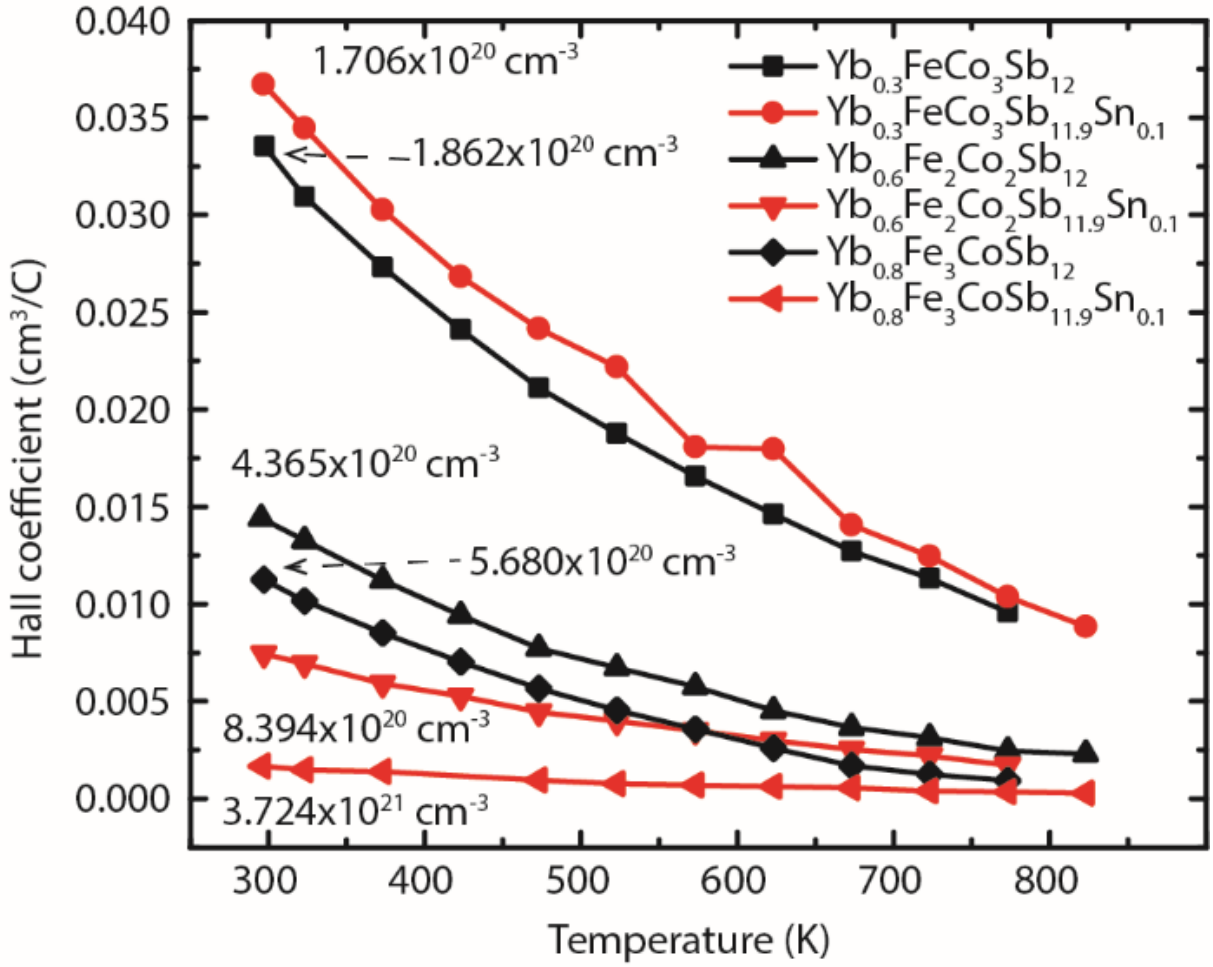

Figure 4.2 High temperature Hall coefficient of $Yb_zFe_{4-y}Co_ySb_{12-x}Sn_x$ samples. The room temperature carrier concentration of different samples is labeled in the figure.

Temperature-dependent electrical conductivity and Seebeck coefficient measured from 300 K to 800 K are shown in Fig. 4.3a-b. The electrical conductivity decreases as temperature increases for all 6 samples, suggesting that they are degenerate semiconductors. Positive Seebeck and Hall coefficients confirm that $Yb_zFe_{4-y}Co_ySb_{12-x}Sn_x$ samples are all *p*-type semiconductors. The influence of Yb, Fe, and Sn dopants on electrical conductivity is quite significant. Electrical conductivity is related to carrier concentration and mobility as:

$$\sigma = ep\mu \qquad \textit{Equation 4.20}$$

Since the Fe dopant concentration effectively tunes the carrier concentration, the electrical conductivity dramatically increases with the Fe concentration. On the contrary, Sn dopants have larger impact on the mobility than the carrier concentration, as shown in Figure 4.4a. Thus, Sn-doped samples exhibit lower electrical conductivity compared to their Sn-free counterparts. Incorporating Sn dopants does not significantly affect the Seebeck coefficient, which suggests that the approach to enhance the thermoelectric power factor by generating Sn resonant levels is not successful in $Yb_zFe_{4-y}Co_ySb_{12-x}Sn_x$ filled skutterudites. On the other hand, varying Yb and Fe doping concentration influences the Seebeck coefficient in a complex manner. In addition to modifying the magnitude of thermopower, a significant change of the temperature dependence of the Seebeck coefficient is observed, which implies a significant dependence of the band structure on the Yb and Fe concentrations. The change of the temperature dependence of the Seebeck coefficient likely originates from the energy shift of the heavy Fe-d band as the Fe concentration increases. This change of the band structure details can also be seen from the Pisarenko relation between the Seebeck coefficient and carrier concentration, as shown in Figure 4.4b. The Seebeck coefficients of the 6 $Yb_zFe_{4-y}Co_ySb_{12-x}Sn_x$ samples do not follow the Pisarenko trend in which the Seebeck coefficient decreases as the carrier concentration increases. The increasing Seebeck coefficient with increasing carrier concentration suggests that incorporating Fe dopants significantly enhance the band effective mass.

In order to corroborate this assumption, fitting of electrical transport coefficients was attempted. A least square method was applied to solve for the simultaneous best fit to the Hall coefficient, Seebeck coefficient, and electrical conductivity data. However, no satisfactory fits were found, likely due to the unknown temperature-dependent band structure and scattering

processes. Recently, an *ab initio* band structure calculation corroborated the assumption that the increasing Fe concentration indeed moves the heavy Fe-d band closer to the light Sb-p band.[50] On the one hand, the energy upshift of the heavy Fe-d band pins the Fermi level above the vicinity of the Sn resonant levels, nullifying the influence of the resonant density of states. On the other hand, the convergence of the heavy Fe-d band and the light Sb-p band is beneficial for thermoelectric power factor. The power factor is enhanced approximately 60% from $Yb_{0.3}FeCo_3Sb_{12}$ to $Yb_{0.8}Fe_3CoSb_{12}$, as shown in Figure 4.5.

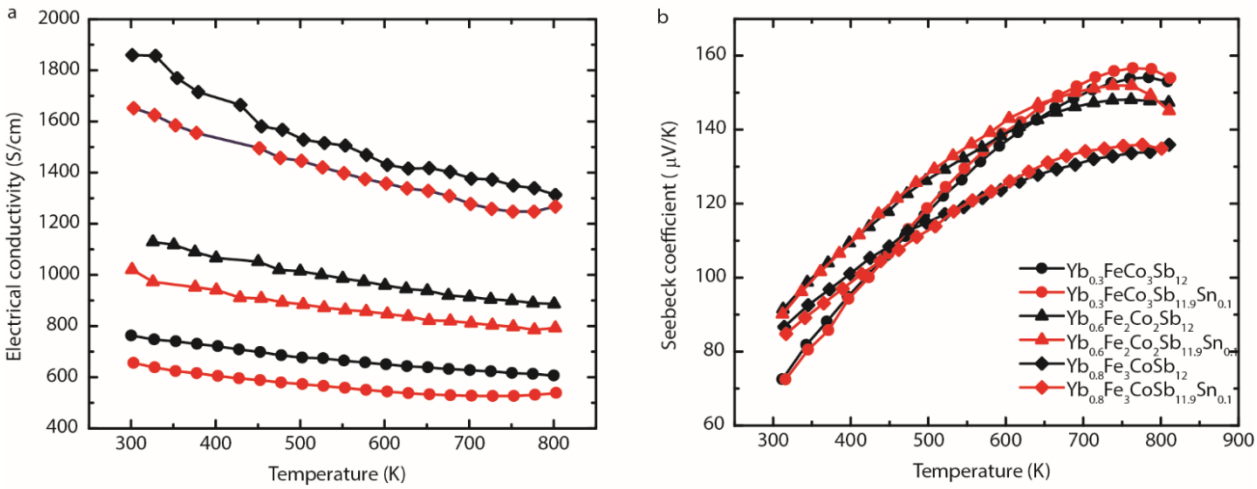

Figure 4.3 High temperature (a) electrical conductivity and (b) Seebeck coefficient from 300 K to 800 K.

Though the contribution of the heavy holes from the Fe-d band leads to a moderately high thermopower at high carrier concentration, these heavy holes are much less mobile than the light holes due to their large effective mass. This is detrimental to the mobility, as shown in Fig. 4.4a. The mobility drops significantly as the Fe concentration increases. The reduced mobility

partly negates the enhancement from the increased carrier concentration. Another drawback from incorporating large concentration of Fe dopants is the high carrier concentration. This large carrier concentration leads to a reduction on the thermopower at high temperatures, as shown in Fig. 4.3b. Such influence is not observed at low temperatures due to the narrow Fermi window. This suggests that an optimized Fermi level exists for maximum power factor. To achieve this, carrier concentration needs to be further modified. Incorporating other dopants is not promising, because extra impurities introduce too much scattering, similar with what Sn dopants do in $Yb_zFe_{4-y}Co_ySb_{12-x}Sn_x$. Novel doping methods will be demonstrated in the next chapter, which has the potential to maintain the mobility.

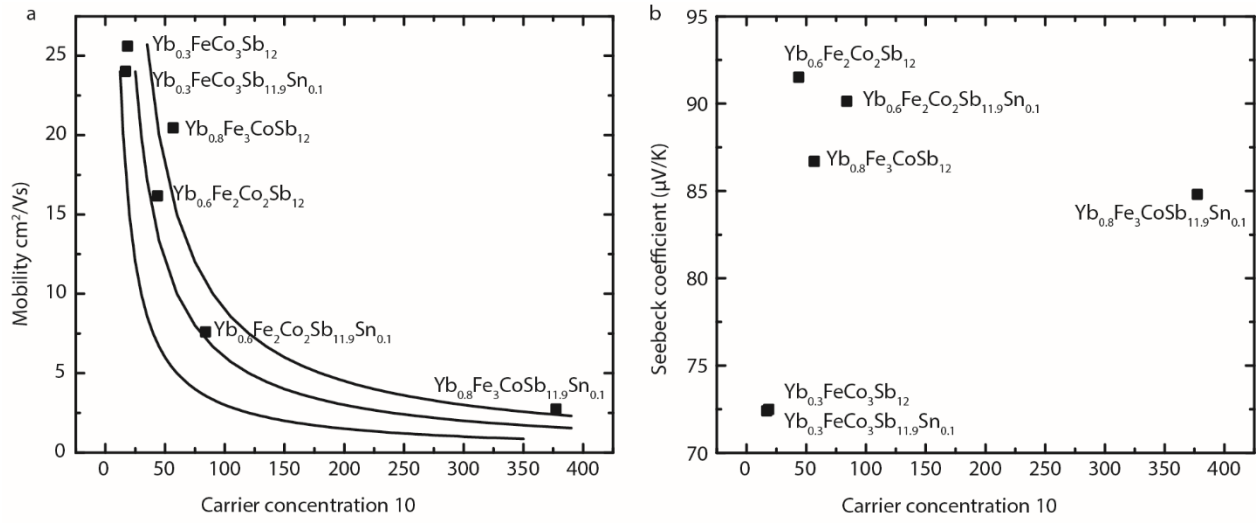

Figure 4.4 (a) Room temperature mobility vs. carrier concentration for all 6 $Yb_zFe_yCo_{4-y}Sb_{12-x}Sn_x$ samples. (b) Room temperature Seebeck coefficient vs. carrier concentration.

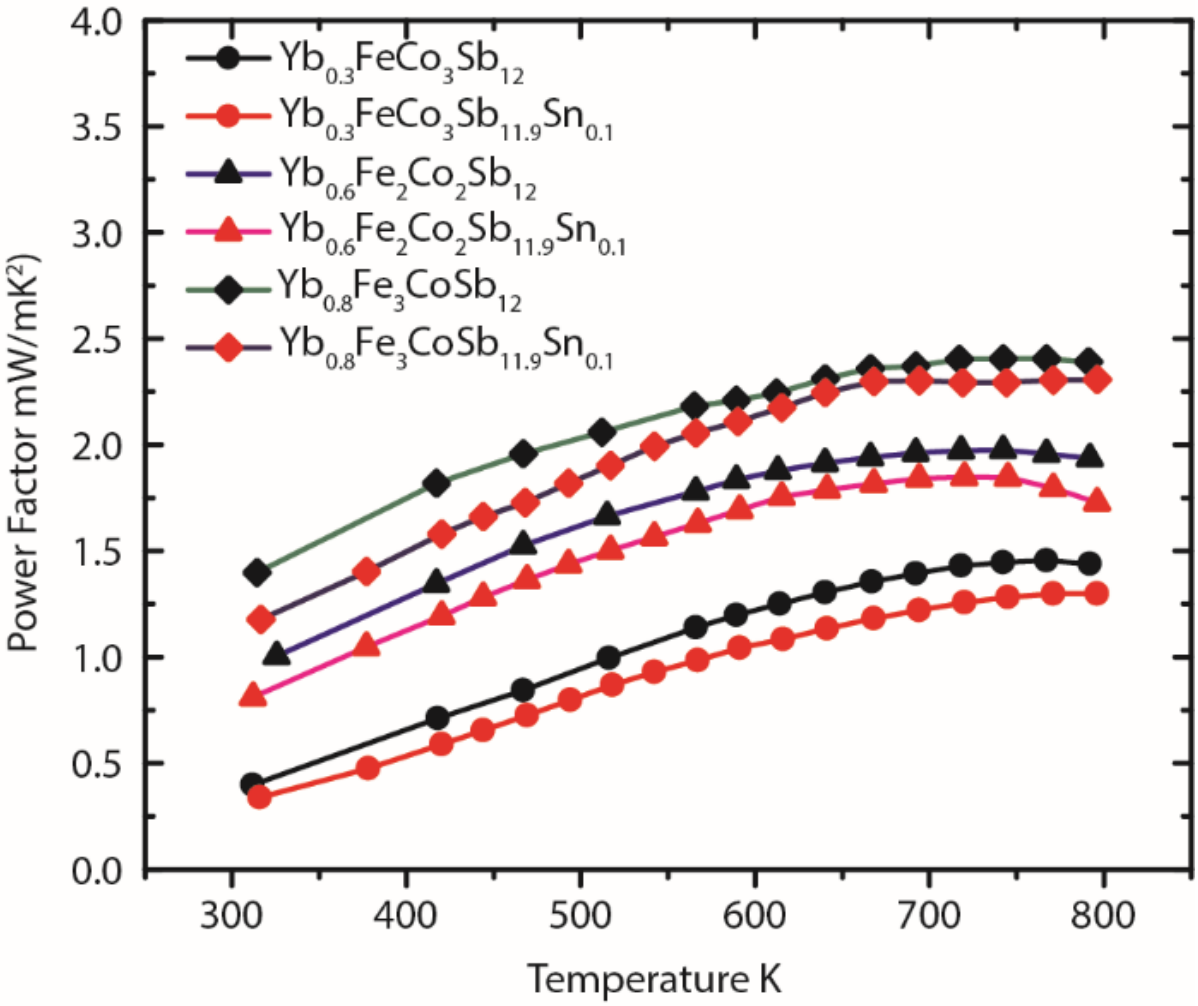

Figure 4.5 High temperature power factor of $Yb_zFe_{4-y}Co_ySb_{12-x}Sn_x$ samples.

In spite of the strong scattering on the carriers, Sn dopants significantly scatter acoustic phonons. The total and lattice thermal conductivities of the Sn-doped samples were greatly reduced compared to those of the Sn-free samples, as shown in Fig. 4.6. However, Yb and Fe dopants increase the total thermal conductivity. The independence of the lattice thermal conductivity on the Yb and Fe concentration indicates that Yb and Fe dopants mainly contribute

to the electronic part of the total thermal conductivity. A slightly enhanced thermoelectric figure of merit was achieved using Sn dopants, as shown in Fig. 4.7.

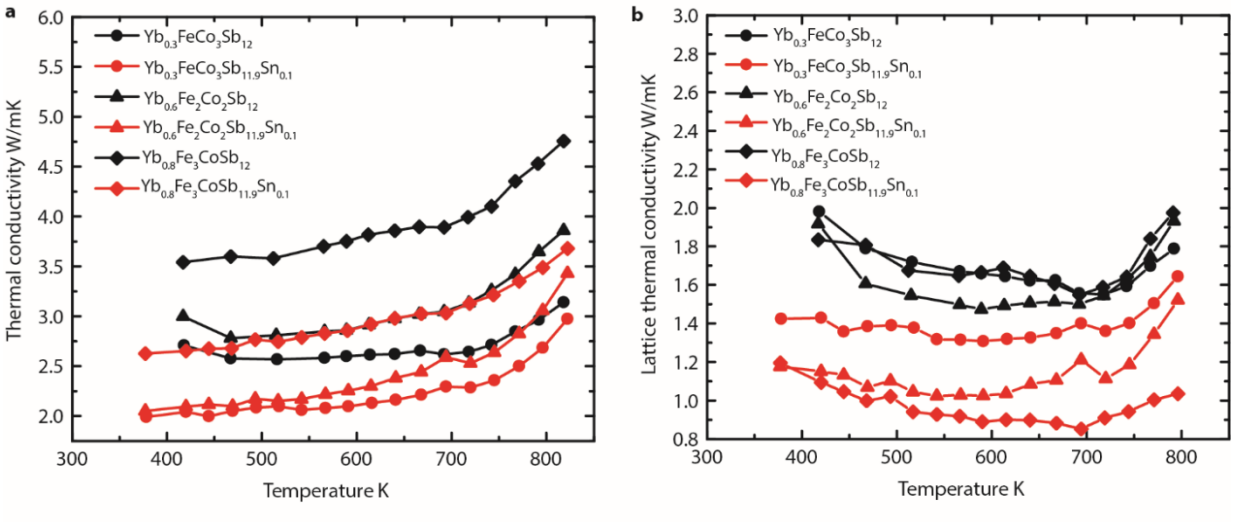

Figure 4.6 (a) Thermal conductivity from 300 K to 800 K. (b) Lattice thermal conductivity from 300 K to 800 K.

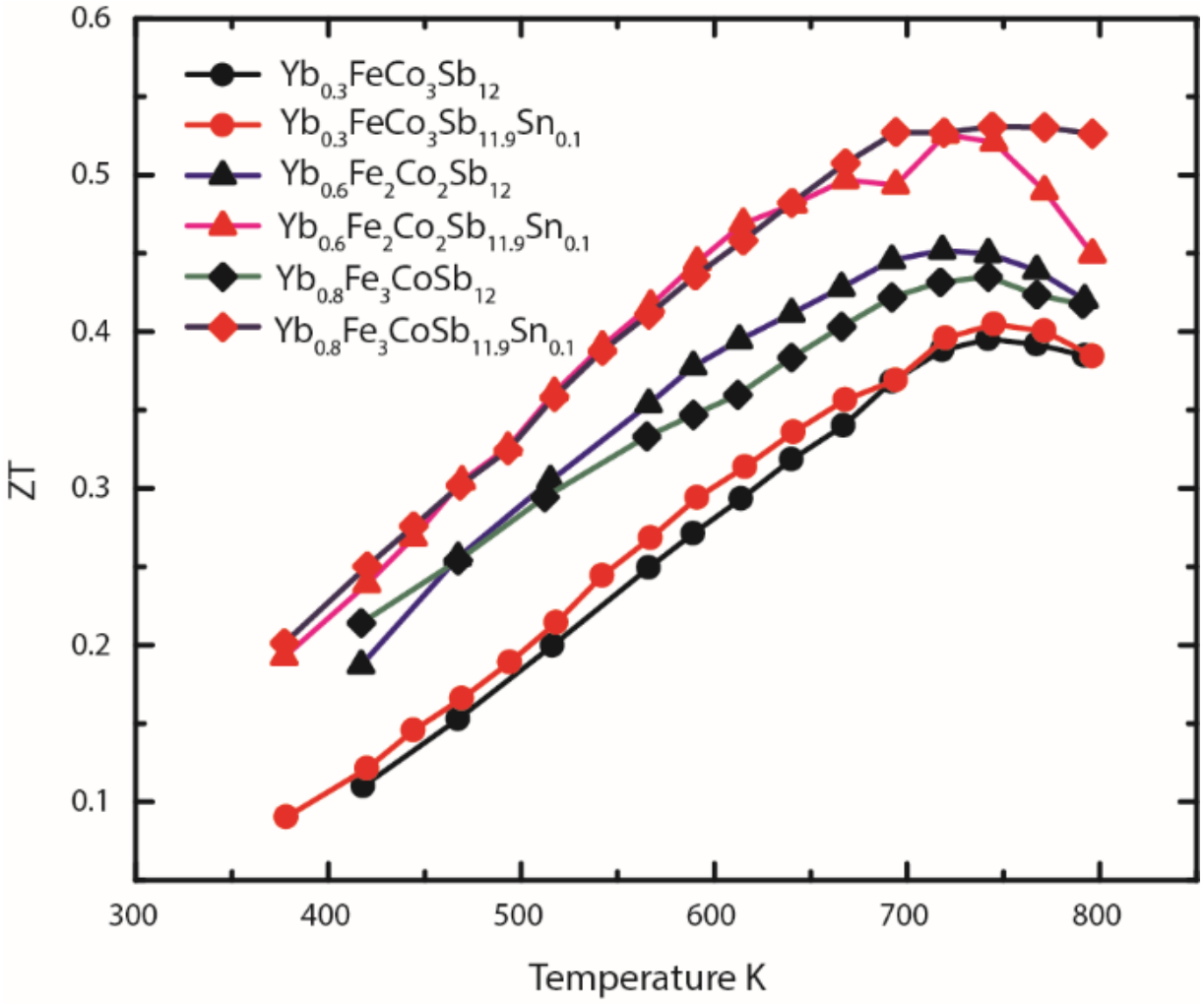

Figure 4.7 High temperature thermoelectric figure of merit.

4.6 Summary

A secondary *p*-type dopant Fe was successfully incorporated on the Co sites and the carrier concentration was thus increased. However, thermoelectric transport measurements indicate that the influence of Sn resonant levels is still not visible. This is attributed to the upshift

of the heavy Fe-d band as the Fe concentration increases. Sn dopants did prove beneficial for thermoelectric figure-of-merit by reducing thermal conductivity.

In addition, we found that increasing the Fe concentration moves the Fe-d band closer to the Sb-p band, which is confirmed by a recent *ab initio* calculation. Such convergence of the heavy Fe band and the light Sb band is beneficial to the thermoelectric performance, confirmed by an enhancement of power factor from 15 $\mu Wcm^{-1}K^{-2}$ for $Yb_{0.3}FeCo_3Sb_{12}$ to 25 $\mu Wcm^{-1}K^{-2}$ for $Yb_{0.8}Fe_3CoSb_{12}$. The contribution of the heavy holes in the heavy Fe band keeps the thermopower at a moderate value in spite of a large carrier concentration. Thus the Seebeck coefficient of $Yb_{0.8}Fe_3CoSb_{12}$ is higher than that of $Yb_{0.3}FeCo_3Sb_{12}$ at room temperature. However, the situation reverses at higher temperatures. This is attributed to the widening of the Fermi window as the temperature increases. As lower temperature, the contribution from the deep heavy Fe band is negligible and the Seebeck coefficient is determined primarily by the contribution of light holes. As the temperature increases, the widening Fermi level gradually touches the heavy Fe band and thus the Seebeck coefficient of $Yb_{0.3}FeCo_3Sb_{12}$ exceeds the value of $Yb_{0.8}Fe_3CoSb_{12}$ at higher temperatures become of a smaller carrier concentration. Such tradeoff between the carrier concentration and the heavy holes suggests an existence of an optimized carrier concentration for maximum power factor. A conventional doping method based on the ionization of impurity atoms has drawbacks due to the severe ionized impurity scattering introduced. A novel doping mechanism is desired, such as that described in the next chapter.

Chapter 5 Engineering Temperature-Dependent Carrier Concentration for Average Power Factor Enhancement *via* Novel Doping Method

5.1 Introduction

Conventional doping is to incorporate guest elements into the matrix. Such method is effective to adjust the carrier concentration. However, most of the dopants have low excitation energies, and thus they can be fully ionized at low temperatures.[51] As a result, the carrier concentration of conventionally doped materials is temperature independent over a wide temperature range. The simulation results presented later, together with the experimental results reported in literature suggest that the carrier concentration needed to optimize the power factor varies with temperature.[52] Thus, a temperature-dependent carrier concentration is desired for high temperature thermoelectric power generation. In this work, we proposed a novel method of incorporating secondary phase materials with a different temperature dependence of Fermi level than the matrix. The charge transfer across the interface of the matrix and the secondary phase aggregates causes a dramatic change of the carrier concentration in the matrix. Numerical simulation also indicates that the charge transfer is sensitive to the Fermi level offset between the matrix and the aggregates. Since the Fermi level offset is temperature-dependent caused by the

distinct temperature dependence of the Fermi level in matrix and secondary-phase aggregates, the carrier concentration in matrix is temperature-dependent. By applying this method to the GeTe-$CuInTe_2$ composites with $CuInTe_2$ as the secondary-phase dopants, the average power factor within a wide temperature range is achieved. Compared to the mobility of GeTe-In_2Te_3 solid solutions, the mobility of secondary-phase-doped GeTe is significantly higher. The synthesis process of the composites is suggested to be important for the doping method. Indeed, by changing from mechanically mixing the micron-size particles of the two materials to direct quenching the mixture of the melts, the thermoelectric power factor is doubled. For the GeTe-$CuInTe_2$ composites with GeTe as the secondary-phase dopants, the thermoelectric power factor is also enhanced, though through a different mechanism. The power factor of $CuInTe_2$ is significantly enhanced at approximately 600 K. Such enhancement is attributed to the energy filtering effect.

5.2 Material Synthesis and Pellet Sintering

Raw elements of germanium, copper, indium, and tellurium were purchased from Alfa Aesar with the following purities: Ge (pieces, 99.9999+%), Cu (shot, 99.999%), In (ingots, 99.9999+%), and Te (lumps, 99.999+%). The starting materials were weighed in the glovebox according to the stoichiometric ratio $(Ge_2Te_2)_{x\%}(CuInTe_2)_{1-x\%}$ with x=100, 95, 90, 87.5, 85, 70, 30, 15, 10, and 0. In this chapter, the samples are denoted as GT-x, where x represents the concentration of GeTe in the sample. The weighed materials were then put in carefully cleaned quartz ampoules and sealed under the pressure of less than 10^{-4} Torr and placed in a furnace

heated according to the following schedule: slow heating up to 1273 K at the rate of 1.5 K/min; rest at 1273 K for 12 hours; slow cooling down to 873 K at 2 K/min; annealing at 873 K for 4 days; and finally slow cooling down to room temperature at 2 K/min. The as-cast ingots were hand-milled to powders under argon atmosphere and hot-pressed at the temperature of ~773 K under the pressure of ~60 MPa for 30 min.

5.3 Crystallographic and Microstructural Characterization

The density of all samples as measured by the Archimedes method is given in Table 5.1. All GeTe rich samples (samples with the GeTe concentration larger than or equal to 70%) have densities above 6.07 g/cm^3, while the $CuInTe_2$-rich samples (samples with the content of GeTe less than or equal to 30%) have densities below 5.88 g/cm^3. If we take the theoretical density of GeTe from the literature to be 6.14 g/cm^3,[53] and 6.07 g/cm^3[54] for $CuInTe_2$, then the theoretical density of the composites can be calculated as below, assuming the phases are separated:

$$\rho = \frac{\rho_{CuInTe_2}\left(1+\frac{m_{CuInTe_2}\times(1-x\%)}{m_{Ge_2Te_2}\times x\%}\right)}{\frac{\rho_{CuInTe_2}}{\rho_{GeTe}}+\frac{m_{CuInTe_2}\times(1-x\%)}{m_{Ge_2Te_2}\times x\%}} \qquad \textit{Equation 5.1}$$

where ρ_{CuInTe_2} is the theoretical density of $CuInTe_2$, ρ_{GeTe} is the theoretical density of GeTe, m_{CuInTe_2} is the molecular mass of $CuInTe_2$, $m_{Ge_2Te_2}$ is the molecular mass of Ge_2Te_2, and x is the concentration of GeTe in the composites. The results of the theoretical densities of the composites together with the corresponding relative densities of the samples are also listed in

Table 5.1. All the GeTe-rich samples have relative densities above 98.9%, while $CuInTe_2$-rich samples only have relative densities between 93% and 97%. This difference suggests that the optimized hot-pressing conditions for GeTe-rich and $CuInTe_2$-rich composites are different and the one we use in this study is optimized only for GeTe-rich composites. The powder XRD patterns of 5 selected samples (GT-100, GT-90, GT-70, GT-30, and GT-10) are presented in Figure 5.1. The major phases of all the samples are identified as those of GeTe and $CuInTe_2$ for the GeTe-rich and the $CuInTe_2$-rich samples, respectively, according to the known peak positions of the minerals (GeTe: ref. 06-0469 and $CuInTe_2$: ref. 06-0605). There are also traces of the secondary phase of Ge in the pure GeTe sample (Ge: ref. 03-0478). Several major Cu β diffraction peaks are also identified and labeled in Figure 5.1, due to the strong Cu β radiation of the X-ray source. As the concentration of $CuInTe_2$ increases, the intensity of the $CuInTe_2$ peaks increases, while that of the GeTe peaks decreases. The peak of Ge impurity disappears for all the $CuInTe_2$-added samples, indicating that the amount of trace Ge falls below the detection limit of powder XRD. The coexistence of GeTe and $CuInTe_2$ peaks confirms that GeTe and $CuInTe_2$ can only form composites, due to the different space group of the two compounds ($CuInTe_2$ has a tetragonal structure with the space group $I\bar{4}2d$, while GeTe crystallizes with a rhombohedral structure in the space group $R4m$).[53, 54] The secondary phase of Ge is present because Ge forms as a consequence of native defects in GeTe.

Sample Name	GT-100	GT-98	GT-95	GT-92.5	GT-90	GT-87.5	GT-85	GT-80	GT-70	GT-30	GT-15	GT-10
Density (g/cm^3)	6.099	6.121	6.071	6.130	6.087	6.143	6.122	6.146	6.082	5.875	5.676	5.664
Theoretical Density (g/cm^3)	6.140	6.139	6.136	6.134	6.132	6.131	6.129	6.125	6.118	6.090	6.080	6.076
Relative Density (%)	99.3	99.7	98.9	99.9	99.3	>100	99.9	>100	99.4	96.5	93.4	93.2

Table 5.1 Measured densities, theoretical densities, and relative densities of $(Ge_2Te_2)_{x\%}(CuInTe_2)_{1-x\%}$.

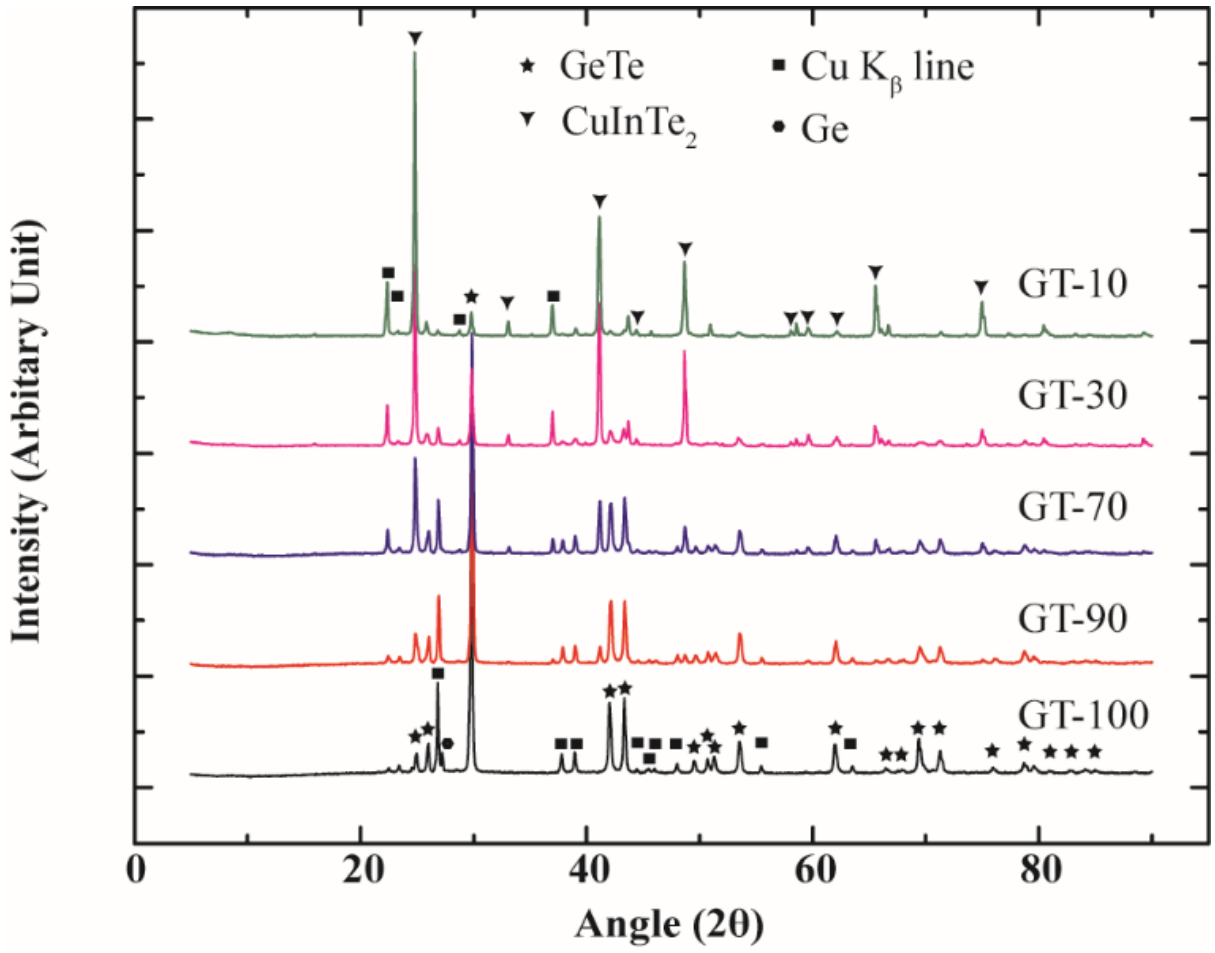

Figure 5.1 Powder XRD patterns of 5 typically selected samples, GT-100, GT-90, GT-70, GT-30, and GT-10.

The BSE images of the GT-98 and GT-95 samples are presented to illustrate the segregation of $CuInTe_2$ secondary phases, as shown in Figure 5.2a-b. The segregation of $CuInTe_2$ in GT-98 sample suggests that the solubility limit of Cu or In in the GeTe matrix is below 2%. The contrast of light and dark regions in the BSE image clearly confirms the existence of two phases with the light-colored "bubbles" depicting the $CuInTe_2$ phase with its larger average atomic weight of 433.566, while the dark background corresponds to the GeTe matrix having a smaller average atomic weight of 400.460. Two macroscale BSE images of GT-70 and GT-90 are presented for comparison, shown in Figure 5.2c-d. The size of the segregated $CuInTe_2$ varies from several micrometers for GT-90 to 50 micrometers for GT-70, and various shapes of the segregated phase can be identified as bubbles, dots, polygons, or stripes in the GT-70 sample. As the concentration of $CuInTe_2$ decreases from 30% to 10%, the extent of the segregated $CuInTe_2$ also decreases, and the shape tends to be only spherical.

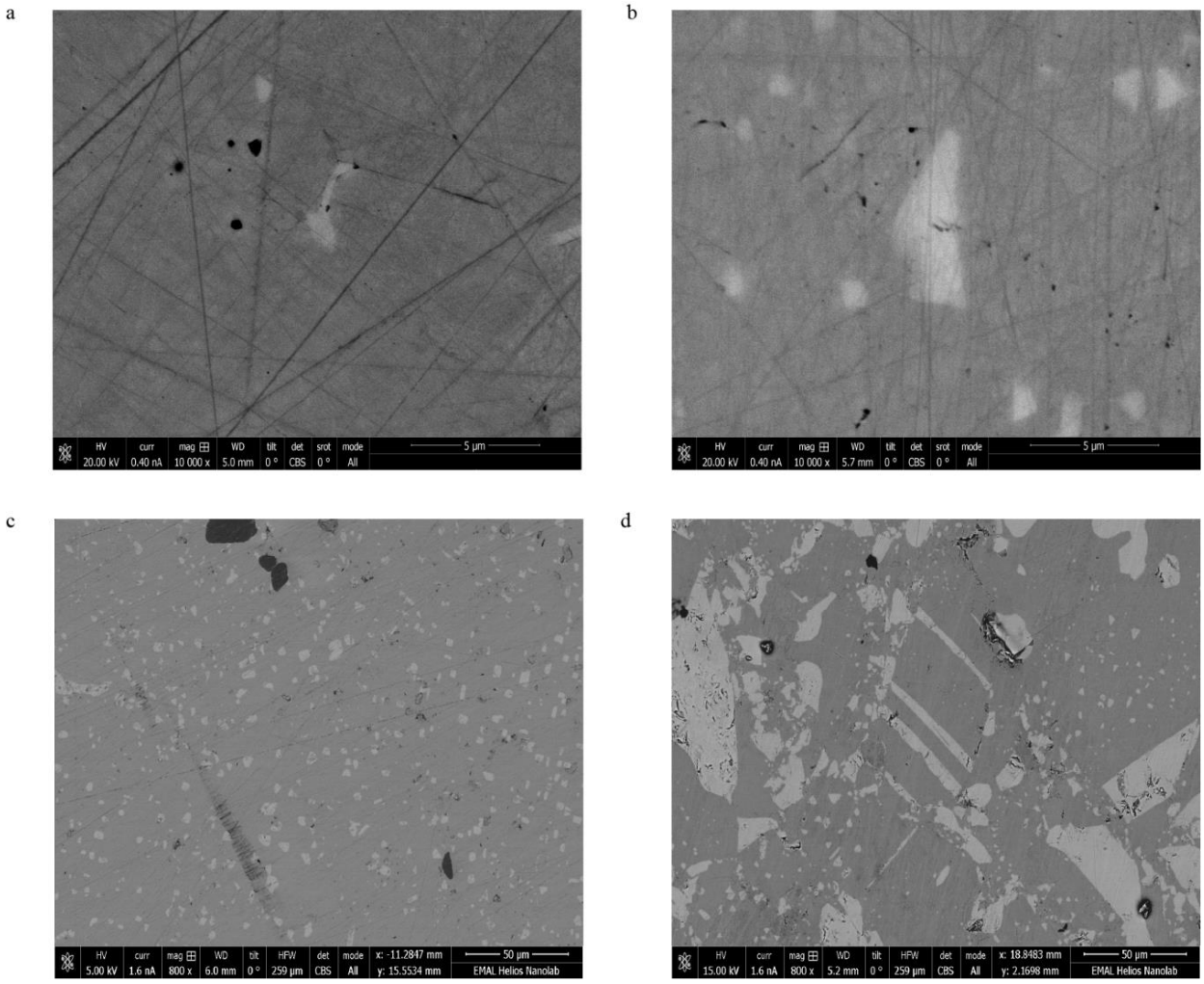

Figure 5.2 (a): Back scattered electron (BSE) image of the GT-98 sample with 10000× magnification. (b): BSE image of the GT-95 sample with 10000× magnification. (c): BSE image of the GT-90 sample with 800× magnification. (d): BSE image of GT-70 sample with 800× magnification.

EDS element mapping further verifies the phase separation of GeTe and $CuInTe_2$, as shown in Figure 5.3a, where the target element accumulates in the lighter area. A small amount of pure Ge is detected in the Ge mapping image as a very light spot and this spot corresponds to the dark spot in the Te mapping image, though the concentration of Ge is so small that powder XRD is not able to detect it. No In or Cu rich secondary phases were detected in the region tested. Since BSE or EDS has detection resolution of approximately 1 μm, nano-scale secondary-phase

aggregates cannot be observed using such technique. High resolution TEM image of a small region of the GT-70 sample is shown in Fig. 5.3b to confirm the nanoscale phase aggregation. The large matrix bears a rhombohedral GeTe structure, well fitted with the overlaid GeTe atomic model. In the matrix, the highlighted area shows an atomic lattice corresponding to the chalcopyrite $CuInTe_2$ structure, confirming the existence of the nano-size $CuInTe_2$ secondary phase. The shape of these nano-size segregations is not spherical. The work function of GeTe and $CuInTe_2$ are determined by UPS. An offset of approximately 0.3 eV is determined. The work function shift shown in the GT-95 sample suggests the interface density is high since the Fermi level is a spatial constant and the local vacuum level bends with the band bending, as illustrated in the middle inset of Fig. 5.3c. This is also confirmed in the XPS peak shifts shown in Fig. 5.3d. The top insets of Fig. 5.3c are the spectroscopy data focusing on the lower (left) and higher (right) kinetic energy range. The right inset verifies that the Fermi levels of the tested 3 samples are all aligned with the measurement system during the measurement, calibrated by measuring Fermi step of a freshly deposited Au film.

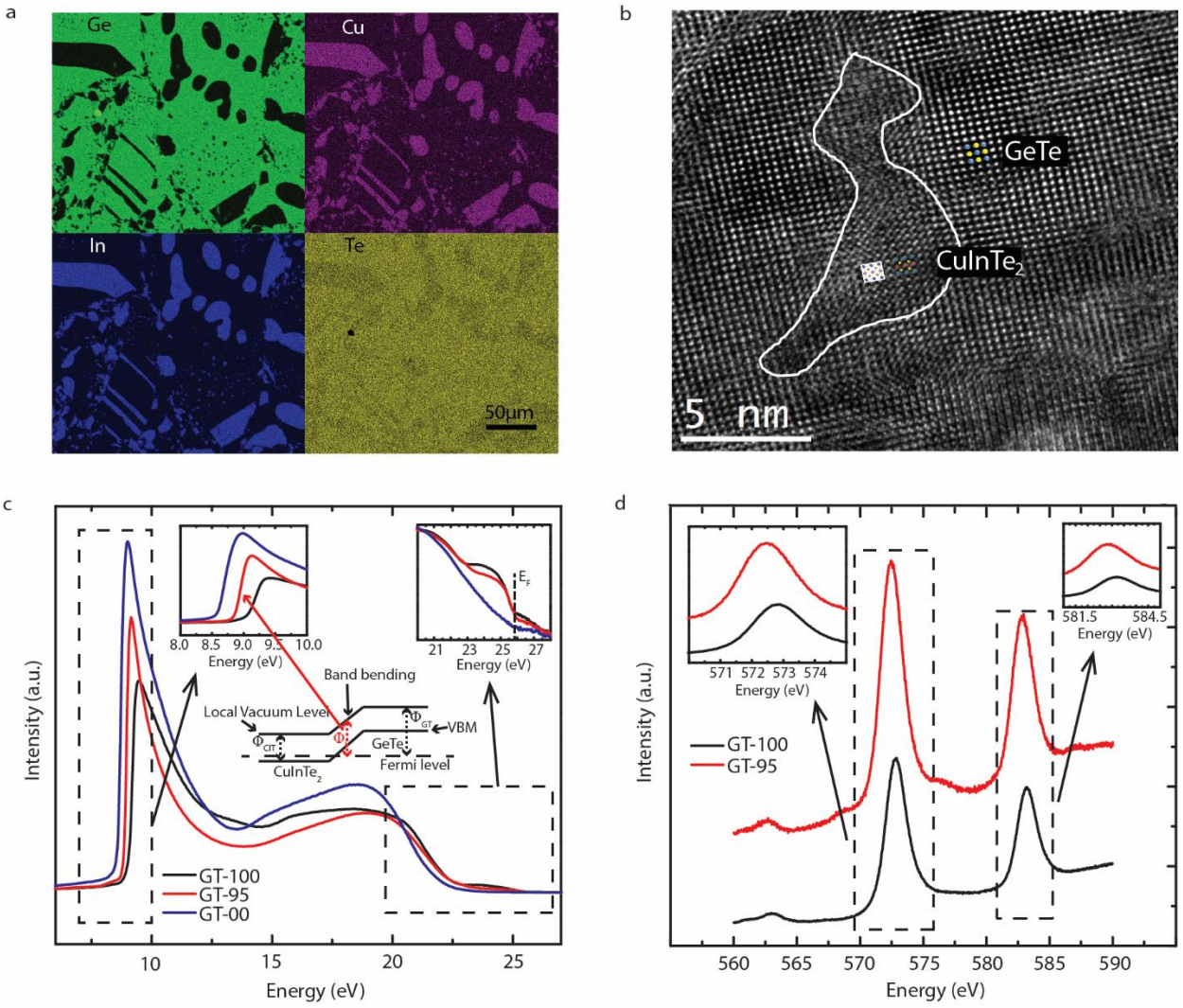

Figure 5.3 (a): EDS mapping of Ge, Cu, In, and Te elements on the GT-70 sample.(b): High resolution TEM image on a small region of the GT-70 sample. (c): UPS results on the GT-100, GT-95, and GT-00 samples. (d): XPS Te-3d core levels.

It will be demonstrated in the next section by calculation that high density of nanoscale $CuInTe_2$ segregations is crucial for the matrix carrier concentration adjustment. However, it is not easy to have a statistical distribution of these nanoscale particles from a single TEM image. Instead, an EDS mapping on a region of ~300 nm size confirms that the signal of Cu and In is

almost everywhere, confirming that the nanoscale $CuInTe_2$ is distributed homogenously in the matrix, as shown in Fig. 5.4.

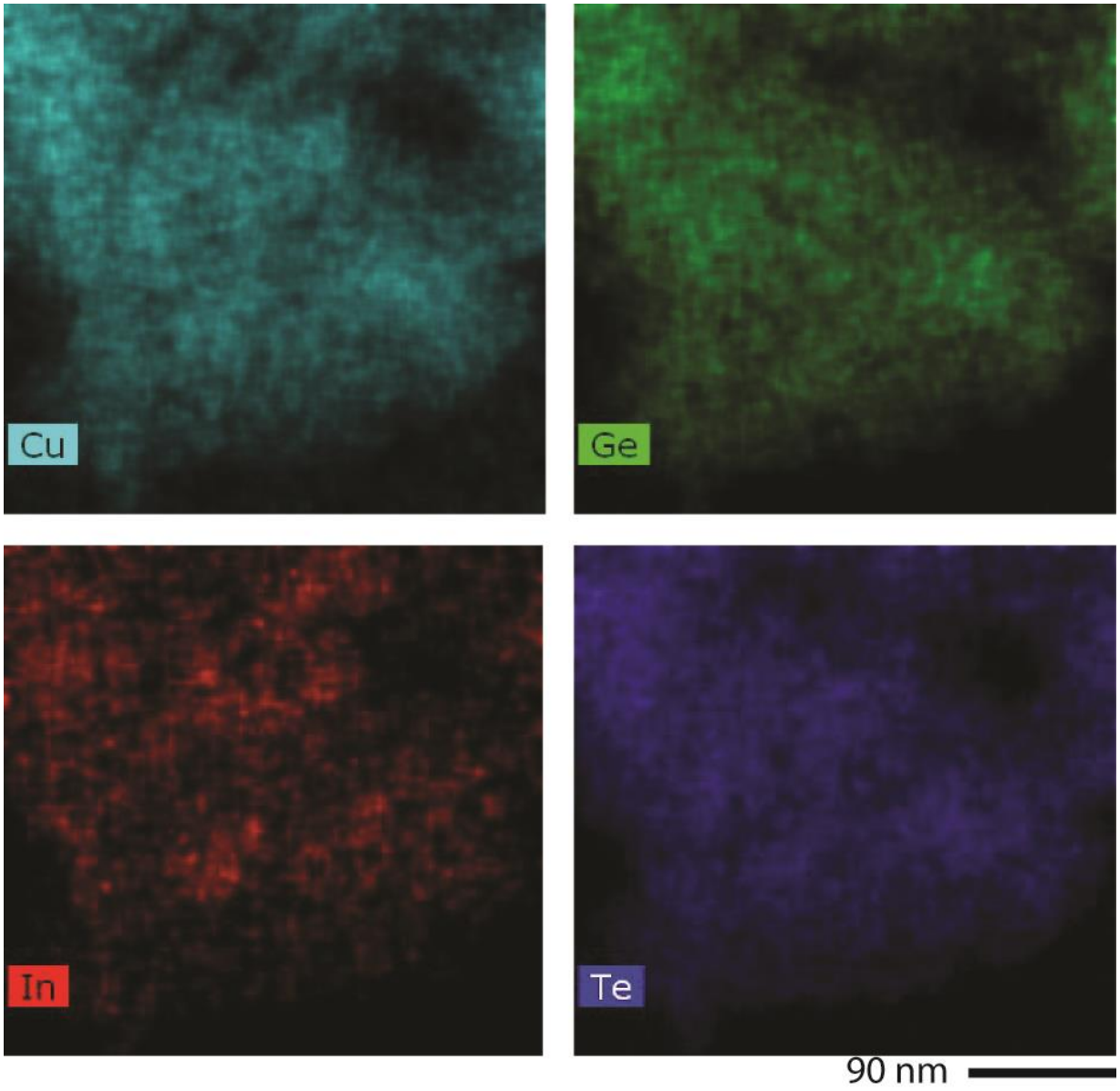

Figure 5.4 EDS mapping of Cu, Ge, In, and Te on a small region in the GT-70 sample.

5.4 Poisson Model

For simplicity, the inclusions of $CuInTe_2$ are assumed to be spheres and the GeTe phase surrounds the $CuInTe_2$ inclusions. The radius of $CuInTe_2$ inclusions is related to that of the GeTe phase by the mole concentration of $CuInTe_2$ as:

$$x = \left(\frac{R_{CIT}}{R_{GT}}\right)^3 \qquad \textit{Equation 5.2}$$

where x is the doping ratio. The common energy reference is set as the valence band maximum of pure GeTe. Note that we are studying the effect of holes, thus the energy increases deeper into the valence band. The spatial distribution of the electrostatic potential $V(r)$ is caused by the charge redistribution after the two phases come into contact, and the potential distribution can be determined *via* the Poisson equation.

For $r \leq R_{CIT}$ in the $CuInTe_2$ region, the Poisson equation can be written as:

$$\frac{1}{r}\frac{d^2}{dr^2}rV(r) = -\frac{e}{\varepsilon_{CIT}\varepsilon_0}p_{CIT-net}(r) \qquad \textit{Equation 5.3}$$

For $R_{CIT} \leq r \leq R_{GT}$ in the GeTe region, the Poisson equation can be written as:

$$\frac{1}{r}\frac{d^2}{dr^2}rV(r) = -\frac{e}{\varepsilon_{GT}\varepsilon_0}p_{GT-net}(r) \qquad \textit{Equation 5.4}$$

where ε_{CIT} is the dielectric constant of $CuInTe_2$, ε_{GT} is the dielectric constant of GeTe, ε_0 is the vacuum permittivity, $p_{CIT-net}(r)$ is the net charge concentration in the $CuInTe_2$ region, and $p_{GT-net}(r)$ is the net charge concentration in the GeTe region.

At a given temperature, the defect concentration in GeTe and $CuInTe_2$ determines their carrier concentrations. If a certain amount of free carriers move away from a region, it will be left with net charges, which can be written as:

$$p_{net} = p[\mu(r)] - p_0 \qquad \textit{Equation 5.5}$$

where $p[\mu(r)]$ is the new carrier concentration determined by the chemical potential $\mu(r)$ after the charge redistribution, and p_0 is carrier concentration under neutral condition before contact, which is decided by the temperature and defect concentration. If we further assume each material possesses a parabolic band structure (more complex band structure can easily be implemented, here we use parabolic band structure for simplicity), then we have:

$$p_{net} = \frac{4\pi(2m^* k_B T)^{\frac{3}{2}}}{h^3}\int_0^\infty \frac{\eta^{\frac{1}{2}}d\eta}{1+exp\left\{\eta-\frac{E_{F-AC}-E_{VBM-AC}}{k_B T}\right\}} - p_0 \qquad \textit{Equation 5.6}$$

with E_{F-AC} representing the Fermi energy after two phases come into contact, and E_{VBM-AC} representing the energy of the maximum of the valence band after two phases come into contact. Plugging *Eqn.* 5.6 into 5.3 and 5.4, we have:

For $r \le R_{CIT}$,

$$\frac{1}{r}\frac{d^2}{dr^2}rV(r) = -\frac{e}{\varepsilon_{CIT}\varepsilon_0}\left\{\frac{4\pi\left(2m_{CIT}k_B T\right)^{\frac{3}{2}}}{h^3}\int_0^\infty \frac{\eta^{\frac{1}{2}}d\eta}{1+\exp\left\{\eta-\frac{E_{F-AC}-eV(r)-E_{off}}{k_B T}\right\}} - p_{CIT-0}\right\}$$

Equation 5.7

where E_{off} is the energy offset between the maximum of the valence bands of the two phases. And for $R_{CIT} \le r \le R_{GT}$

$$\frac{1}{r}\frac{d^2}{dr^2}rV(r) = -\frac{e^2}{\varepsilon_{GT}\varepsilon_0}\left\{\frac{4\pi\left(2m_{GT}k_BT\right)^{\frac{3}{2}}}{h^3}\int_0^{\infty}\frac{\eta^{\frac{1}{2}}d\eta}{1+exp\left\{\eta-\frac{E_{F-ac}-eV(r)}{k_BT}\right\}} - p_{GT-0}\right\}$$

Equation 5.8

In order to solve for V(r) within the domain that we are interested in, additional boundary conditions are needed. At the center of the $CuInTe_2$ inclusion, we set the electric field to be zero, that is:

$$-\frac{dV(r)}{dr}\Big|_{r=0} = 0 \qquad \textit{Equation 5.9}$$

On the other hand, since the total charge within the domain of $r \leq R_{GT}$ is conserved, based on Gauss's law, the electric field at $r = R_{GT}$ is also zero:

$$-\frac{dV(r)}{dr}\Big|_{r=R_{GT}} = 0 \qquad \textit{Equation 5.10}$$

On the interface between the $CuInTe_2$ and GeTe phases, the discontinuity of the electrostatic potential depends on the interface dipole, which is material dependent. Also, the electrical field discontinuity is decided by the interface free charge density. Here, for simplicity, we set them both to be zero. Thus, the third and fourth boundary conditions on the interface are:

$$V(r = R_{CIT}^{-}) - V(r = R_{CIT}^{+}) = 0 \qquad \textit{Equation 5.11}$$

$$-\varepsilon_{CIT}\frac{dV(r)}{dr}\Big|_{r=R_{CIT}^{-}} = -\varepsilon_{GT}\frac{dV(r)}{dr}\Big|_{r=R_{CIT}^{+}} \qquad \textit{Equation 5.12}$$

We used the fourth-order Runge-Kutta algorithm with the shooting method to numerically solve the Poisson equation with the above boundary conditions. The electrostatic potential, electric

field, and charge distribution profile at the interfaces are shown as Fig. 5.5a. To estimate the bulk matrix carrier concentration change due to such a charge transfer effect, we divide the total amount of charge transferred across the interface by the total volume of the sample in the manner of "averaging" the charge transfer effect.

The band bending and charge distribution profiles, together with the average carrier concentration change in the matrix, depend on many parameters, including the Fermi level offset, band structure details, the dielectric constant of each phase, the electrostatic potential drop across the interface, the original carrier concentration in each phase before contact, the secondary phase inclusion size, and secondary phase volume fraction. Other parameters are not included in the model, such as surface states, charge accumulation, and the non-spherical geometry of the inclusion shape. Many of these parameters are fixed when two specific materials are selected, thus a more detailed and rigorous model regarding the whole parameter space must be developed as material selection criteria. Here, we focus on the parameters that change significantly in the GeTe-$CuInTe_2$ system, such as Fermi level offset, secondary inclusion size, secondary phase volume fraction, and the inclusion shape. The average bulk matrix carrier concentration change depending on these parameters is shown as Fig. 5.5b-d.

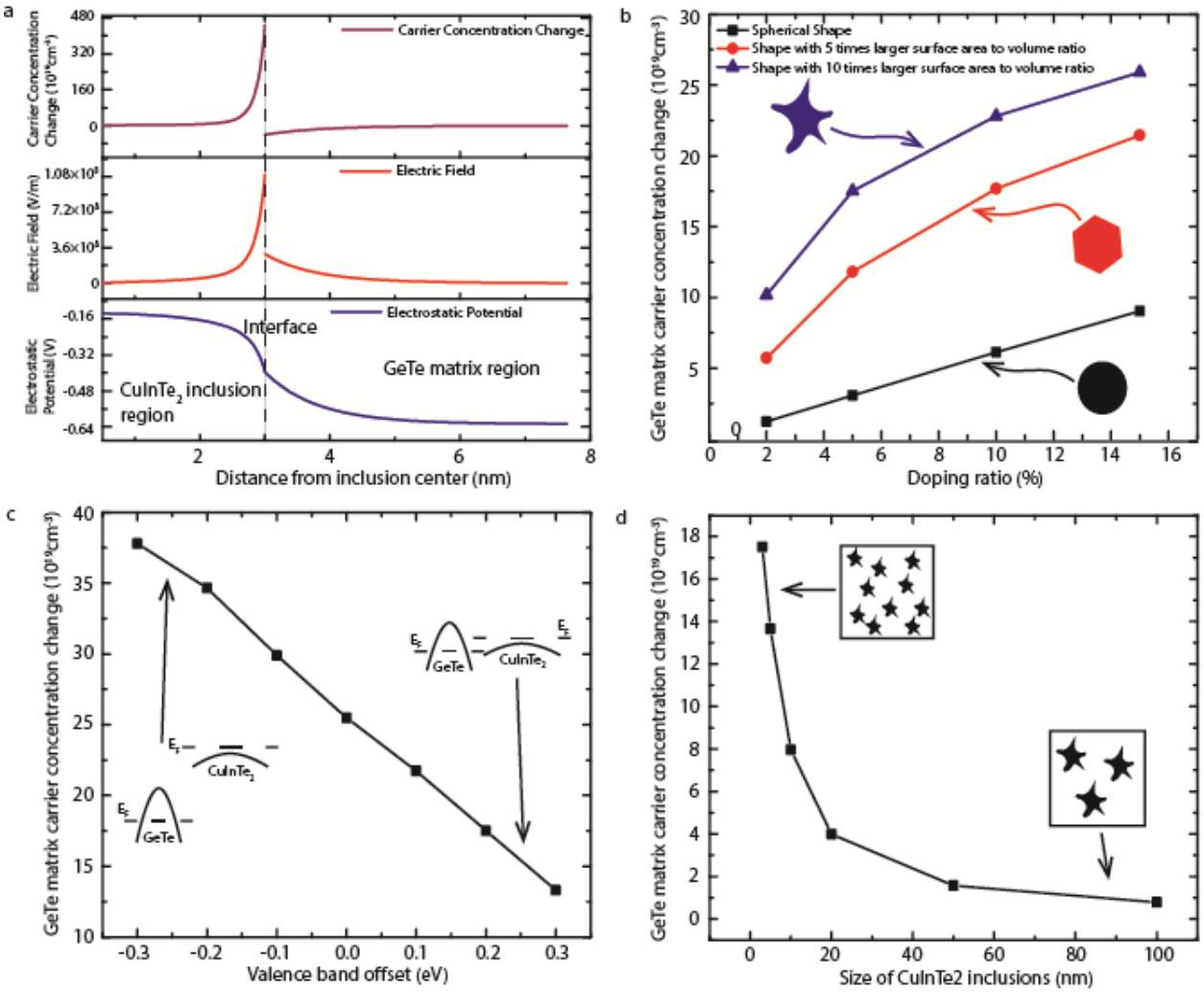

Figure 5.5 (a): Room temperature carrier concentration change, electric field, and electrostatic potential distribution near the interface between GeTe and $CuInTe_2$ phases. (b): Average room temperature carrier concentration depletion over the bulk region as a function of secondary phase concentration with various secondary phase geometries of different surface area to volume ratio. (The size of the secondary phase is set to be 3 nm) (c): Average carrier concentration depletion over the bulk region as a function of valence band offset. (The size of the secondary phase is set to be 3 nm and the doping ratio is set to be 5 mol%) (d): Average room temperature carrier concentration depletion over the bulk region as a function of the size of the $CuInTe_2$ inclusions. (The doping ratio is set to be 5 mol% and the surface to volume ratio is set to be 10 times larger than that of spheres)

5.5 Transport Properties Calculation

For a single parabolic band, the Hall coefficient, the Seebeck coefficient, and the electrical conductivity can be expressed as below by solving the Boltzmann transport equation with the relaxation time assumption:

$$R_H = \frac{1}{e}\left(\frac{\hbar^2}{2m^* k_B T}\right)^{\frac{3}{2}} 3\pi^2 \frac{1}{2} \frac{F_{-\frac{1}{2}}(\eta^*)}{\left(F_0(\eta^*)\right)^2} \qquad \textit{Equation 5.13}$$

$$\sigma = e^2 w \frac{2}{3\pi^2\hbar^2}\left(\frac{\hbar^2}{2m^*}\right)^{-\frac{1}{2}} k_B T F_0(\eta^*) \qquad \textit{Equation 5.14}$$

$$S = \frac{k_B}{e}\left\{2\frac{F_1(\eta^*)}{F_0(\eta^*)} - \eta^*\right\} \qquad \textit{Equation 5.15}$$

where e is the elementary charge, ħ is the reduced Planck's constant, m^* is the effective mass, k_B is the Boltzmann constant, T is the absolute temperature, w is the proportionality constant, $\eta^* = \frac{E_F}{k_B T}$ is the reduced Fermi level, and $F_j(\eta^*) = \int_0^\infty \frac{\eta^j}{1+\exp(\eta-\eta^*)} d\eta$ is the Fermi integral of the j-th order. The relaxation time has the energy dependence as:

$$\tau = wE^r \qquad \textit{Equation 5.16}$$

where w is the proportionality constant, which we set to a value of 1.2×10^{-23} in this work. With acoustic phonon scattering assumed as the dominant scattering process, the scattering parameter r has the value of $-\frac{1}{2}$.

The carrier concentration of a parabolic band can be expressed as:

$$p = \frac{4\pi(2m^* k_B T)^{\frac{3}{2}}}{h^3} F_{\frac{1}{2}}(\eta^*) \qquad \textit{Equation 5.17}$$

The dependence of power factor on the temperature and carrier concentration is shown in Figure 5.6. Relaxation time assumption is applied here and the dominant scattering mechanism is assumed to be acoustic phonon scattering. An unambiguous conclusion can be drawn that the carrier density for the peak power factor changes with the varying temperatures. The changing effective mass of the parabolic band will only alter the specific carrier concentration value for the peak power factor corresponding to the cases of certain materials. Such special dependence originates from the fact that the Fermi-Dirac distribution, which decides the total carrier density and power factor, highly depends on the temperature.

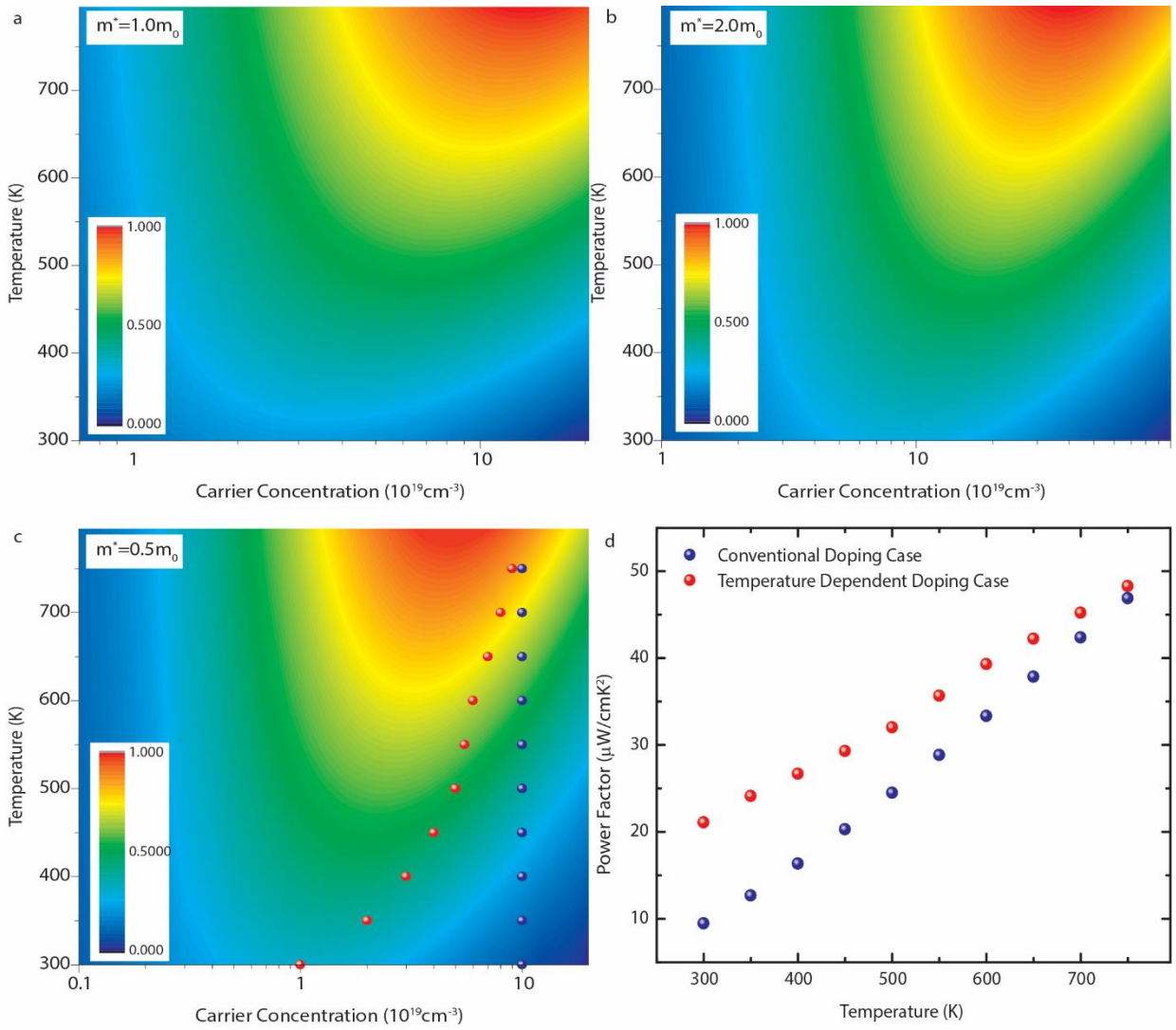

Figure 5.6 (a)-(c): Normalized power factor as a function of carrier concentration and temperature for single parabolic bands of various effective masses. (d): Temperature-dependent power factor with carrier concentration following the trajectories shown in (c).

5.6 Thermoelectric Transport Properties

The temperature-dependent heat capacity clearly indicates that a phase transition has taken place at around 650 K for all the samples, Figure 5.7. It is also noticeable that both the

phase transition temperature and the heat capacity value generally decrease as the mole fraction of $CuInTe_2$ increases. The decreasing phase transition temperature suggests that a small amount of Cu and In might go into the GeTe lattice to alter the phase transition temperature, which has also been observed in a previous study on the In-doped GeTe;[55] however, the phase transition temperature shift in our samples is only around 15 K, much smaller than the value observed in the In-doped GeTe of 125 K, indicating that the amount of Cu and In that went into the GeTe lattice in our sample is much smaller than that of In-doped GeTe in the previous study.[55] The decreasing heat capacity value is consistent with our previous microstructure analysis that GeTe and $CuInTe_2$ form composites with two separated phases and each phase contributes to the heat capacity individually. Three consecutive heat capacity measurements were also done on the GT-87.5 sample to confirm the repeatability of the measurement, inset of Figure 5.7. An abnormal upturn of the heat capacity after the phase transition peak can be observed in the GeTe-rich samples. This feature is confirmed by the three consecutive measurements on the GT-87.5 sample and another measurement at Michigan State University. We qualitatively attribute such an upturn feature to Te vaporization at high temperatures, since we observed the Te deposition layer both inside and outside the crucible after each measurement.

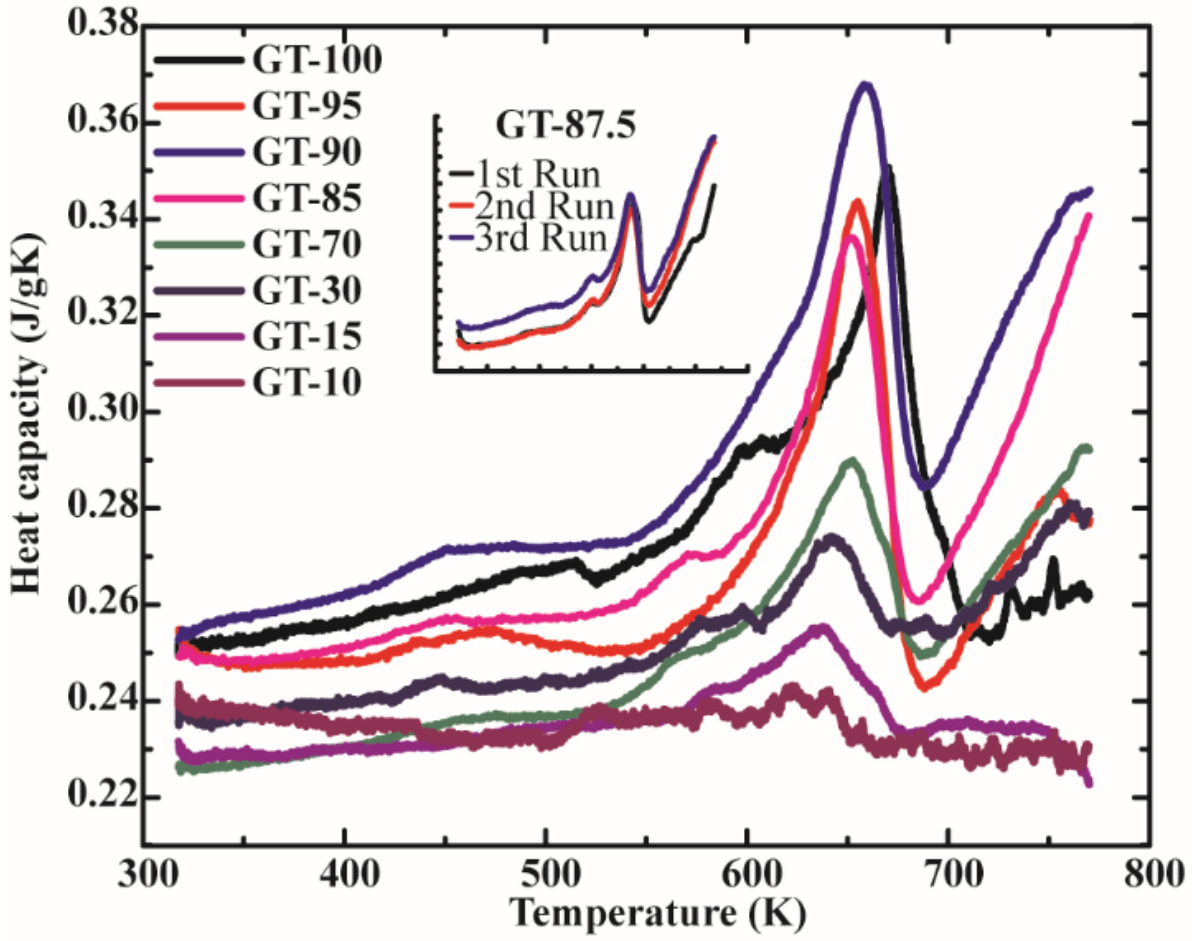

Figure 5.7 Specific heat capacity data of the GeTe-$CuInTe_2$ samples. Results of 3 consecutive measurements on the GT-87.5 sample are shown as the inset.

High temperature electrical transport properties of GeTe-$CuInTe_2$ composites are shown in Figure 5.8. Pure GeTe exhibits the typical metallic conduction feature that the Seebeck coefficient and electrical conductivity have a positive and negative monotonic dependence on the temperature, respectively, confirming that the natural defects on the Ge site make pure GeTe a heavily doped semiconductor. Though the phase transition of pure GeTe is observed in the specific heat capacity curve, it does not influence the electrical transport properties. However, a

distinct mark from 575 K to 625 K on the temperature dependence of the electrical transport parameters of four GeTe-rich composites was observed, which corresponds to the temperature range that is slightly lower than the phase transition peak in the heat capacity data. In the inverse Hall coefficient data that will be discussed later, the temperature range of 575 K to 625 K features convergent inverse Hall coefficient data for all the GeTe-rich samples. I attributed this distinct mark on both the temperature dependence of the electrical transport parameters and the inverse Hall coefficient between 575 K and 625 K to the convergence of the Fermi energy.

According to Fig. 5.5, the incorporation of $CuInTe_2$ secondary phases decreases the electrical conductivity and increases the Seebeck coefficient within the whole temperature range. As the molar fraction of $CuInTe_2$ increases above 70%, the significantly increased Seebeck coefficient and decreased electrical conductivity suggest that the carrier concentration is significantly decreased. The anomalous discontinuity of the temperature dependence of the Seebeck coefficient and electrical conductivity can also be observed for the $CuInTe_2$-rich samples around 600 K. However, the fact that it occurs over the expanded temperature range from 500 K to 700 K indicates that it is not related to the phase transition. Another anomaly is that both the Seebeck coefficient and electrical conductivity increase from 500 K to 600 K for the GT-15 and GT-30 samples. The simultaneous increasing Seebeck coefficient and electrical conductivity result in a sharp increase in the power factor within the temperature range from 500 K to 650 K, nearly tripling the power factor. Though the simultaneously increasing electrical parameters are not observed for the GT-10 sample, a similar feature of rapidly increasing power factor is still present due to the fact that the increasing electrical conductivity has much larger temperature dependence than that of the decreasing Seebeck coefficient. Despite having almost identical power factors with the pure GeTe sample at high temperatures, the GT-95 and GT-90

samples exhibit significantly enhanced power factors at lower temperatures resulting in a much improved average power factor over the whole temperature range. The GT-85 and GT-70 samples have much lower power factors than that of pure GeTe at elevated temperatures, suggesting that incorporating more than 15% mole fraction of $CuInTe_2$ is detrimental for the power factor.

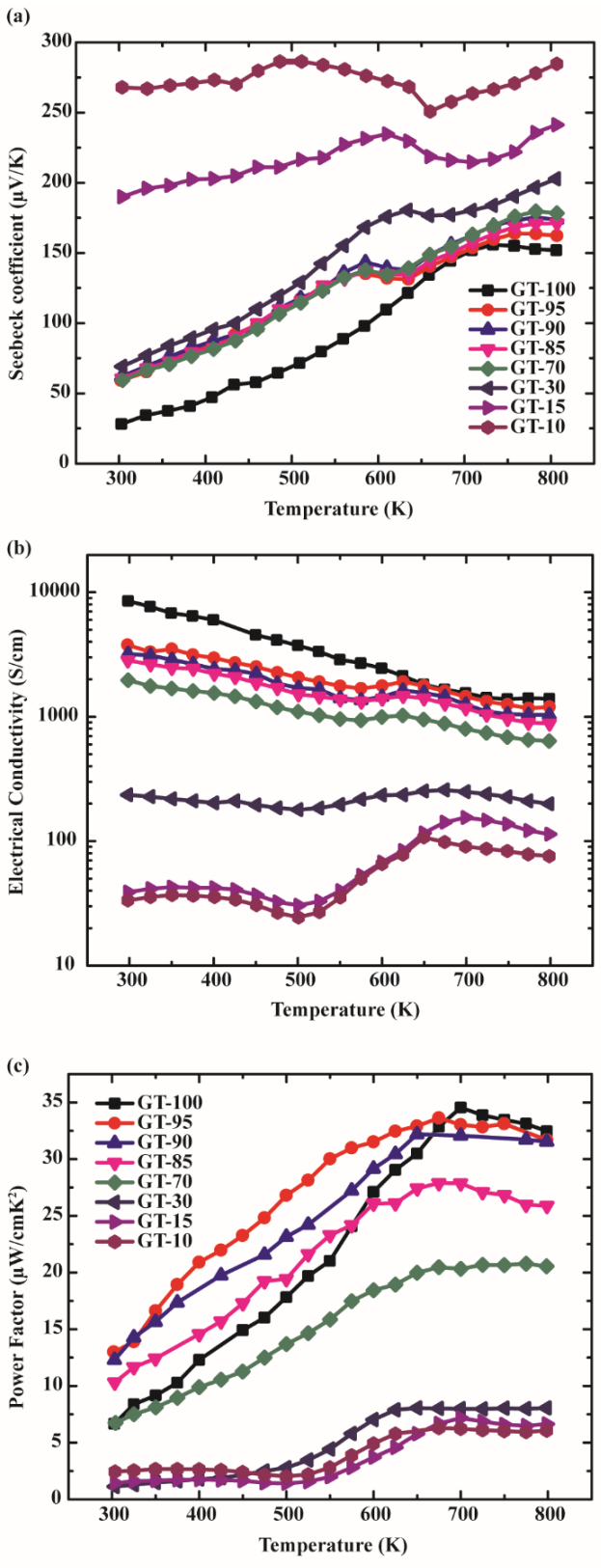

Figure 5.8 High temperature (a) electrical conductivity, (b) Seebeck coefficient, and (c) power factor of 8 GeTe-$CuInTe_2$ samples.

In the XRD phase identification and BSE, SEM, and TEM microstructural analyses, we have confirmed that GeTe and $CuInTe_2$ segregate as separated phases. Below we will show in detail that this two-phase separation feature is crucial for understanding the electrical transport properties in the GeTe-$CuInTe_2$ composites. Electronic band structure schematics of the heterojunction at the interface of GeTe and $CuInTe_2$ phases in the GeTe-rich composites before and after contact at various temperatures are shown in Figure 5.9.

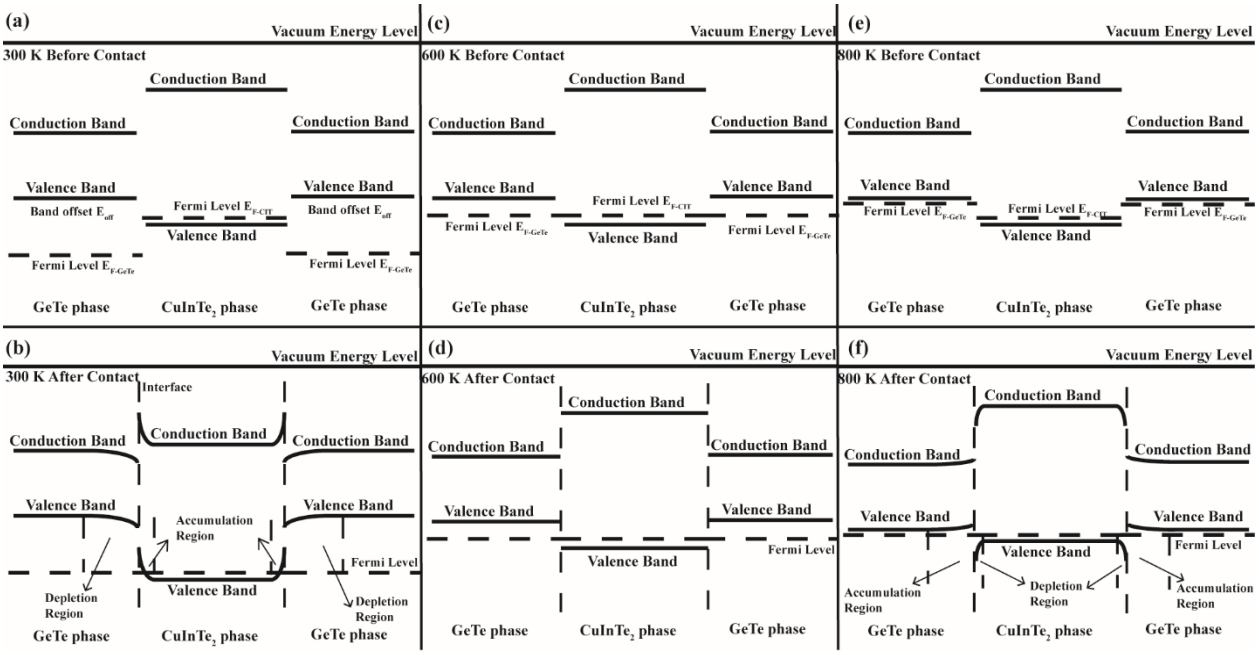

Figure 5.9 Schematics of the band alignment on the interface between GeTe and $CuInTe_2$ phases in GeTe-rich composites (a) 300 K before contact, (b) 300 K after contact, (c) 600 K before contact, (d) 600 K after contact, (e) 800 K before contact, and (f) 800 K after contact.

The determination of the temperature-dependent Fermi energy relative to the valence band maximum of the $CuInTe_2$ phase was based on Boltzmann transport theory and the experimental high temperature Seebeck coefficient, assuming a single parabolic valence band

located at the Γ point, as suggested by previous band structure calculations.[56, 57] The Seebeck coefficient for a single parabolic band is expressed as:

$$S = \frac{k}{e}\left[\frac{2F_1(\eta)}{F_0(\eta)} - \eta\right] \qquad \textit{Equation 5.18}$$

where k is the Boltzmann constant, e is the elementary charge, $\eta = E_f/kT$ is the reduced Fermi level, and $F_r(\eta)$ is the Fermi integral defined as:

$$F_r(\eta) = \int_0^\infty \frac{\varepsilon^r}{1+exp(\varepsilon-\eta)}\, d\varepsilon \qquad \textit{Equation 5.19}$$

The determination of the temperature dependent Fermi energy in the pure GeTe phase relative to its light band edge is more complicated. It is believed that GeTe has 4-fold degenerate light valence bands at *L* point and deeper 12-fold degenerate heavy valence bands at Σ point with an energy difference of 0.27 eV – 0.38 eV at 300 K.[55, 58-60] Here, we take the value of 0.36 eV obtained by Sun et al.[55] The energy difference between the light *L* band and the heavy Σ band also decreases as the temperature increases.[47, 60, 61] Here, we take the temperature dependence of the energy difference to be -1.2×10^{-3} eV/K to meet the requirement that these two bands converge at around 600 K, which was suggested by the Hall coefficient measurement in this work shown in Figure 5.10a and previous work.[47, 60] The two band model for GeTe Fermi energy determination is then expressed as:[55]

$$p_l = 4\pi\left(\frac{2m_l^* kT}{h^2}\right)^{3/2} F_{1/2}(\eta_l) \qquad \textit{Equation 5.20}$$

$$p_h = 4\pi\left(\frac{2m_h^* kT}{h^2}\right)^{3/2} F_{1/2}(\eta_h) \qquad \textit{Equation 5.21}$$

$$\Delta E = (\eta_l - \eta_h)\cdot kT \qquad \textit{Equation 5.22}$$

$$S = \frac{p_h}{p_h + p_l \cdot b} S_h + \frac{p_l \cdot b}{p_h + p_l \cdot b} S_l \qquad \textit{Equation 5.23}$$

$$S_{l,h} = \frac{k}{e}\left[\frac{2F_1(\eta_{l,h})}{F_0(\eta_{l,h})} - \eta_{l,h}\right] \qquad \textit{Equation 5.24}$$

where p is the hole concentration, m^* is the effective mass, h is the Planck constant, T is the temperature, ΔE is the energy difference between the light L band and the heavy Σ band, b is the mobility ratio of light holes to heavy holes. The subscripts h and l in all the equations correspond to the heavy and light holes, respectively. In this work, we take the parameters from the literature to be $m_l^* = 0.5m_0$, $m_h^* = 2.5m_0$, $\Delta E = 0.36 - 1.2 \times 10^{-3}(T - 300)$ eV, $b = 4$.[55] With the room temperature Fermi level offset determined to be 0.3 eV from UPS measurement, the temperature dependent Fermi energy of GeTe and $CuInTe_2$ relative to the $CuInTe_2$ Γ valence band maximum before contact is shown in Figure 5.10b. It is also worth noting that the positive energy direction is pointing toward the valence band since we are studying holes instead of electrons. Thus, the positive Fermi energy value in Figure 5.10b means that the Fermi level is below the $CuInTe_2$ Γ band maximum.

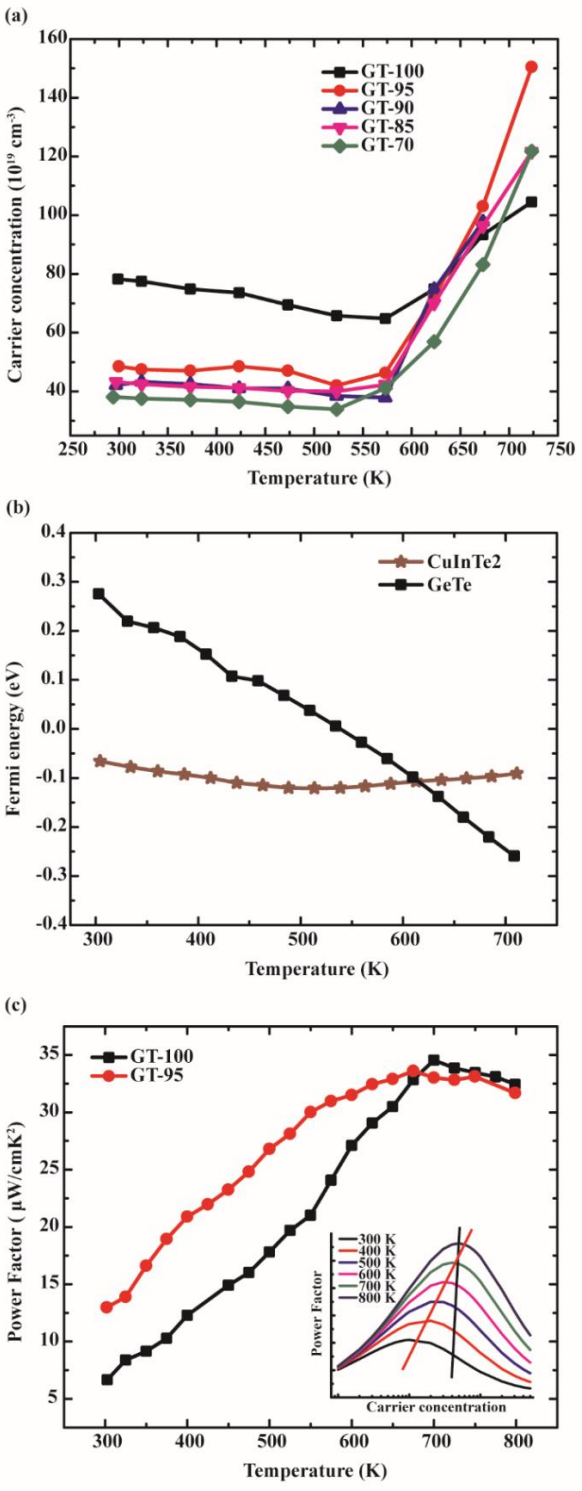

Figure 5.10 (a) High temperature inverse Hall coefficient of 5 GeTe-rich composites, (b) High temperature Fermi energy of pure $CuInTe_2$ and pure GeTe referred to the valence band maximum of $CuInTe_2$ calculated from the measured transport coefficients, and (c) High temperature power factor of the GT-100 and GT-95 samples for comparison. The carrier concentration dependent power factor at various temperatures for a single parabolic band with an effective mass of 0.5 m_e is shown as the inset of (c). The black and red lines in the inset of (c) schematically correspond to the temperature dependence of the carrier concentration of GT-100 and GT-95 samples, respectively.

With the Fermi energy and band offset energy determined, now we are able to discuss in detail how the band alignment and the charge transfer at the interface between the GeTe and $CuInTe_2$ phases influence the transport properties. First, let's discuss the GeTe-rich composites. Figure 5.10b shows that the Fermi energy of GeTe sits at a higher energy than that of $CuInTe_2$ at 300 K before contact, which is schematically illustrated in Figure 5.9a. After the two phases make contact, the carriers in the GeTe phase with larger Fermi energy start to diffuse into the $CuInTe_2$ to build up an electrostatic potential to compensate the Fermi energy difference before contact, and eventually keep the Fermi energy constant over the whole composite material. Consequently, the bands bend near the interface in both the phases, resulting in an accumulation region and a depletion region in the $CuInTe_2$ phase and GeTe phase, respectively, as shown in Figure 5.9b. Such a depletion effect reduces the carrier concentration in the GeTe phase near room temperature significantly, as confirmed by the Hall coefficient measurement shown in Figure 5.10a. The carrier concentration drops from 8×10^{20} cm^{-3} to below 5×10^{20} cm^{-3} at 300 K. As the temperature increases, the Fermi energy difference between the GeTe phase and $CuInTe_2$ phase starts to decrease and at around 600 K, the Fermi energy converges before contact, as shown in Figure 5.9c. Since there is no Fermi energy difference between the two phases, the carriers will not diffuse across the interface after contact, resulting in negligible band bending near the interface, as shown in Figure 5.9d. Thus, $CuInTe_2$ will not deplete the carriers in the GeTe phase at this temperature and the inverse Hall coefficient of the pure GeTe and other GeTe-rich composites converges slightly above 600 K, as shown in Figure 5.10a. It is worth noting that the temperature of the converged inverse Hall coefficient is slightly higher than 600 K due to the fact that the carriers are contributed only by the GeTe phase, which is smaller than

the volume that we use to calculate the carrier concentration. Thus, the carrier concentration of GeTe-rich composites is smaller than that of pure GeTe at 600 K.

As the temperature continues going up, the Fermi energy of $CuInTe_2$ sits higher than that of GeTe before contact, as shown in Figure 5.9e. The carriers now diffuse from the $CuInTe_2$ phase into GeTe after contact and an accumulation region and depletion region are formed in the GeTe phase and $CuInTe_2$ phase, respectively, shown in Figure 5.9f. This results in a higher carrier concentration for GeTe-rich composites than that of the pure GeTe, illustrated in Figure 5.10a. The temperature dependent Fermi energy difference between the GeTe and $CuInTe_2$ phases enhances the temperature dependence of the carrier concentration of the GeTe-rich composites compared to that of the pure GeTe by the temperature dependent de-doping effect. The red straight line in the inset of Figure 5.10c represents how the carrier concentration of the GT-95 sample changes as the temperature changes, while the black straight line represents that of the pure GeTe sample. The inset of Figure 5.10c also depicts how the power factor depends on the carrier concentration at various temperatures for a single parabolic band. I conclude that the carrier concentration for the optimized power factor increases as the temperature increases, which is consistent with a previous study.[52] Since the de-doping effect in our sample only happens at lower temperatures while not influencing the carrier concentration at elevated temperatures, the power factor is enhanced at lower temperatures and kept optimized at higher temperatures, resulting in an enhanced average power factor over the whole temperature range. This novel mechanism of temperature-dependent de-doping effect is suitable for enhancing the average power factor of other heavily doped semiconductors that can only be optimized at high temperature *via* traditional doping method.

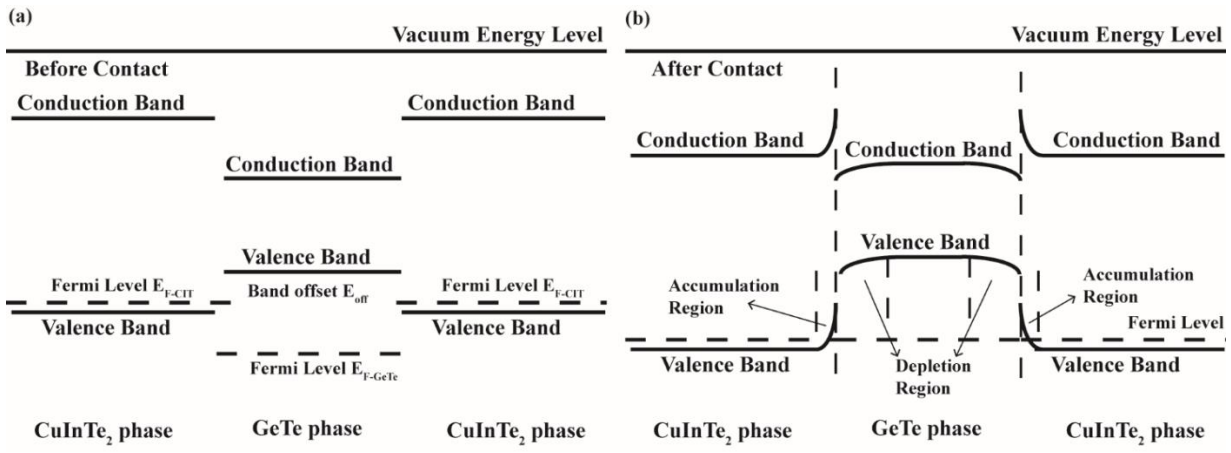

Figure 5.11 Schematics of the band alignment at the interface between GeTe and $CuInTe_2$ phases in $CuInTe_2$-rich composites at (a) 300 K before contact, and (b) 300 K after contact.

While $CuInTe_2$ secondary phases act as de-dopants in the GeTe-rich composites, GeTe secondary phases function quite differently in the $CuInTe_2$-rich composites, which is the next topic of discussion. The band alignment on the interface between the GeTe and $CuInTe_2$ phases at 300 K before and after contact is shown in Figure 5.11. As discussed above, the accumulation region is in the $CuInTe_2$ phase while the depletion region is in the GeTe. However, the Hall coefficient measurement on the $CuInTe_2$-rich samples does not show a dramatic enhancement of the carrier concentration in GT-10 or GT-15 samples compared to the pure $CuInTe_2$ at 300 K, shown in Figure 5.12a. The approximate 4×10^{18} cm^{-3} carrier concentration enhancement at room temperature in the GT-10 and GT-15 samples compared to the pure $CuInTe_2$ is much smaller than the 3×10^{20} cm^{-3} carrier concentration drop in the GT-95 compared to the pure GeTe. We attribute this large difference to the fact that the GeTe secondary phase segregates at larger size. As mentioned in the Poisson Model section, the nanoscale secondary phase segregation is crucial to the carrier concentration adjustment. The GeTe secondary phases with larger scale do not significantly influence the carrier concentration in $CuInTe_2$. Indeed, no Ge signal can be

observed in $CuInTe_2$ in Fig. 5.3a. Hall measurement shows that the carrier concentration of the GT-15 and GT-10 samples increases faster with temperature than the pure $CuInTe_2$ does. This feature is caused by the temperature dependence of the Fermi energy in the $CuInTe_2$ phase. From Figure 5.10b, the Fermi energy of $CuInTe_2$ is around 60 meV at room temperature, increases to a little above 0.1 eV at around 500 K, and then starts to decrease again above 500 K to a value below 0.1 eV. 60 meV corresponds to an excitation energy of ~700 K, which is well above 300 K. Thus, only a very small amount of carriers in the GeTe phase can be thermally excited over the energy barrier, which is equal to the value of the Fermi energy of $CuInTe_2$. As temperature goes up, more and more carriers in the GeTe tend to be thermally excited, however, the increasing energy barrier keeps the carrier concentration at a fairly low value. This behavior is seen in the carrier concentration plateau from 300 K to 500 K in Figure 5.12a. As the temperature goes up above 500 K, more and more carriers tend to conduct across the barrier and the barrier height starts to decrease, thus a sudden increase in the carrier concentration of the GT-10 and GT-15 samples was observed. I can conclude now that the carrier concentration increase in the GT-10 and GT-15 compared to the pure $CuInTe_2$ comes from the thermal excitation of the carriers from the GeTe phase to the $CuInTe_2$ phase, instead of the depletion or accumulation at the interface, which is the main cause for the de-doping effect in the GeTe-rich composites.

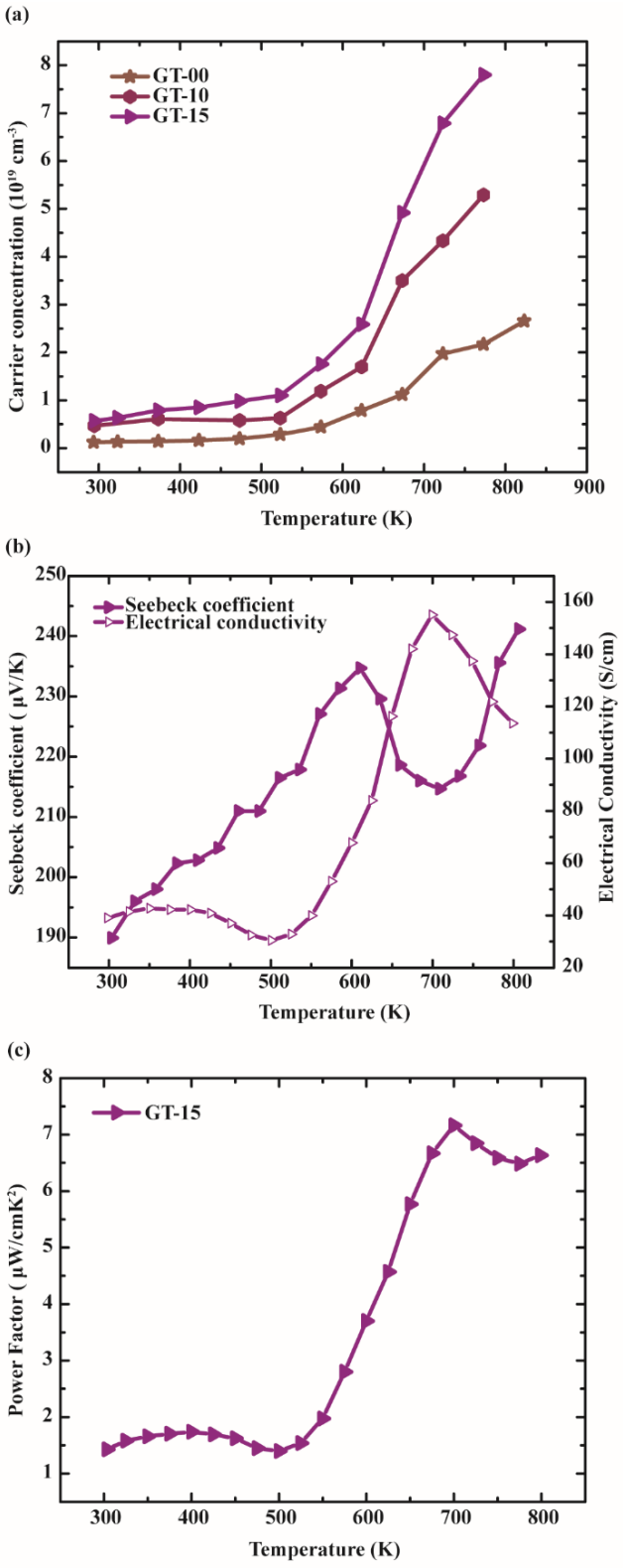

Figure 5.12 (a) High temperature carrier concentration of 3 $CuInTe_2$-rich composites, (b) High temperature Seebeck coefficient and electrical conductivity of the GT-15 sample, and (c) high temperature power factor of the GT-15 sample.

With the charge transfer image in the $CuInTe_2$-rich samples clear in mind, now it is not difficult to explain the simultaneously increasing Seebeck coefficient and electrical conductivity observed in the GT-15 sample. On the one hand, as the temperature increases above 500 K, a large amount of carriers start to be thermally excited over the barrier and contribute to the conduction, thus the electrical conductivity starts to increase dramatically. On the other hand, these excited carriers will continuously move between the $CuInTe_2$ phase and the GeTe phase, thereby experiencing extra scattering. These carriers also tend to occupy the lowest energy in the $CuInTe_2$ bands, since they are excited from even lower energy levels. So a significant amount of low energy carriers have a reduced mobility due to the extra scattering, resulting in an enhanced energy dependence of mobility, which is the well-known effect of energy filtering effect. The enhancement of the Seebeck coefficient is clearly stated in the Mott formula:

$$S = -\frac{\pi^2}{3}\frac{k}{e}kT\left\{\frac{1}{g(E)}\frac{dg(E)}{dE} + \frac{1}{\mu(E)}\frac{d\mu(E)}{dE}\right\}\Big|_{E=E_F} \qquad \textit{Equation 5.25}$$

where $g(E)$ is the density of states, and $\mu(E)$ is the energy-dependent mobility of the carriers. The simultaneously increasing Seebeck coefficient and electrical conductivity of the GT-15 sample, shown in Figure 5.12b, results in a rapid increase of the power factor, shown in Figure 5.12c. The temperature range of this enhancement starts from 500 K, which corresponds to the onset of the thermal excitation discussed earlier. It is also worth noting that this energy filtering effect does not influence the transport properties of the GeTe-rich composites very much by the following argument. At lower temperatures, the carrier concentration increase due to the thermal excitation from the GeTe phase to the $CuInTe_2$ phase in the GT-15 is around 5×10^{18} cm^{-3}. Taking the fact that GeTe is 95% of the whole material in GT-95 rather than 15% in GT-15, the carrier concentration increase due to such thermal excitation over the barrier at low temperature in GT-

95 will be less than 3.0×10^{19} cm^{-3}, which is less than 6% of the total carrier concentration of 5×10^{20} cm^{-3}. Thus, most of the carriers will be blocked by the $CuInTe_2$ secondary phases, and the change of the energy dependence of the mobility contributed by the energy filtering effect is negligible.

In order to uncover the scattering processes in the GeTe-$CuInTe_2$ composites, I performed low temperature transport measurements, the results of which are shown in Figure 5.13. The temperature dependence of the electrical conductivity for the samples GT-*x* with *x*>30 is negative, while GT-15 and GT-10 possess positive temperature-dependent electrical conductivity, Figure 5.13a. This suggests that GeTe dominates the electrical transport properties for the samples with GeTe concentration larger than 30%, which is larger than the percolation threshold, where GeTe forms a continuous path through the material. The electrical conductivity generally decreases as the concentration of $CuInTe_2$ increases. The carrier concentration data also confirms that 30% exceeds the percolation threshold of GeTe in the GeTe-$CuInTe_2$ composites as a large jump of carrier concentration from GT-15 to GT-30 sample can be observed, Figure 5.13b. Low temperature Hall mobility was calculated using the relation:

$$\sigma = ep\mu \qquad \textit{Equation 5.26}$$

The negative temperature dependence of the mobility of 5 GeTe-rich composites suggests mixed scattering processes by acoustic phonons, defects and grain boundaries, while a positive temperature-dependent mobility of the GT-10 and GT-15 samples indicates that only scattering by defects and grain boundaries dominates, as shown in Figure 5.13c. GT-30 shows highly temperature-independent mobility, which represents a transition from GeTe-rich composites to $CuInTe_2$-rich composites near the percolation of GeTe, indicating a suppression of the acoustic

phonon scattering. The mobility generally decreases as the $CuInTe_2$ concentration increases till 70%, when the mobility reaches the minimum. Then the mobility starts to increase as the $CuInTe_2$ concentration continues increasing until 70%. It is of great interest to compare the room temperature mobility of this work to that of a previous work on In-doped GeTe.[55] As shown in the inset of Figure 5.13c, it is obvious that the mobility of GeTe-$CuInTe_2$ composites is significantly larger than that of GeTe-In_2Te_3 solid solutions. It suggests that forming nano-size secondary phases scatters the carriers less significantly than disturbing the lattice by doping does. As discussed earlier, the carrier de-doping effect from the formation of composites, together with enhanced mobility, is a novel mechanism to optimize the thermoelectric performance of semiconductors.

Low temperature thermal conductivity also shows quite different phonon scattering processes between GeTe-rich and $CuInTe_2$-rich samples, Figure 5.13d. The exponentially decreasing thermal conductivity for the $CuInTe_2$-rich samples is due to phonon-phonon scattering processes, while the almost temperature-independent thermal conductivity for the GeTe-rich samples suggests that the phonons are mostly scattered by the grain boundaries and dislocations.

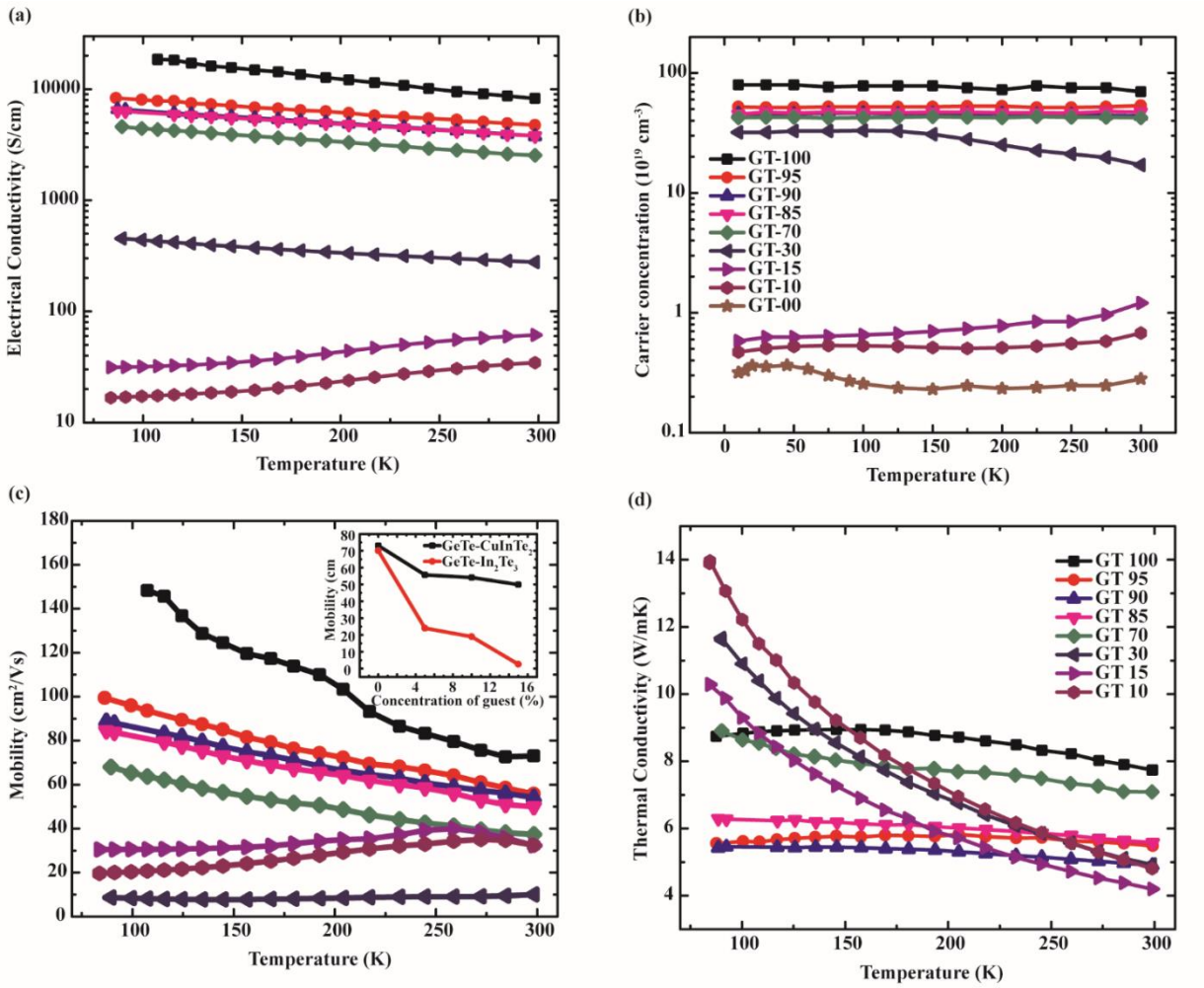

Figure 5.13 Low temperature (a) electrical conductivity, (b) carrier concentration, (c) Hall mobility, and (d) thermal conductivity of GeTe-$CuInTe_2$ composites. The inset of (c) is the comparison of room temperature mobility between GeTe-$CuInTe_2$ composites in this work and GeTe-In_2Te_3 solid solutions.

High temperature thermal conductivity from room temperature to 800 K of all GeTe-$CuInTe_2$ composites generally exhibit negative monotonic temperature dependence, showing the dominance of Umklapp scattering processes, except an anomalous bump from 650 K to 700 K for the GeTe-rich composites, which is related to the phase transition of GeTe, Figure 5.14a. Since GeTe has a much higher thermal conductivity than that of $CuInTe_2$, the total thermal conductivity generally decreases as the mole fraction of $CuInTe_2$ increases. However, the GT-95

sample shows a remarkable deviation from such a trend with its thermal conductivity lower than that of the GT-90 and GT-85 samples and almost identical with that of the GT-70 sample. Such behavior can be attributed to the large amount of small $CuInTe_2$ phases (~500 nm) that can significantly scatter phonons, which was observed in the BSE and SEM images. The large amount of small secondary phase only happens in the GT-95 sample, suggesting that the size of the micron-size $CuInTe_2$ phase is strongly correlated to the mole fraction of $CuInTe_2$ and 5% of $CuInTe_2$ reaches the optimization for the phonon scattering in our study. Because of the enhanced power factor and the suppressed thermal conductivity of the GT-95 sample, the thermoelectric figure of merit *ZT* is greatly enhanced within the whole temperature range studied in this paper from room temperature to 800 K. The 800 K *ZT* is improved from 0.8 to 1.12 by almost 50%, Figure 5.14b. Remember that this *ZT* value is only a lower bound, since we overestimated the thermal conductivity value due to the high temperature Te evaporation effect mentioned before.

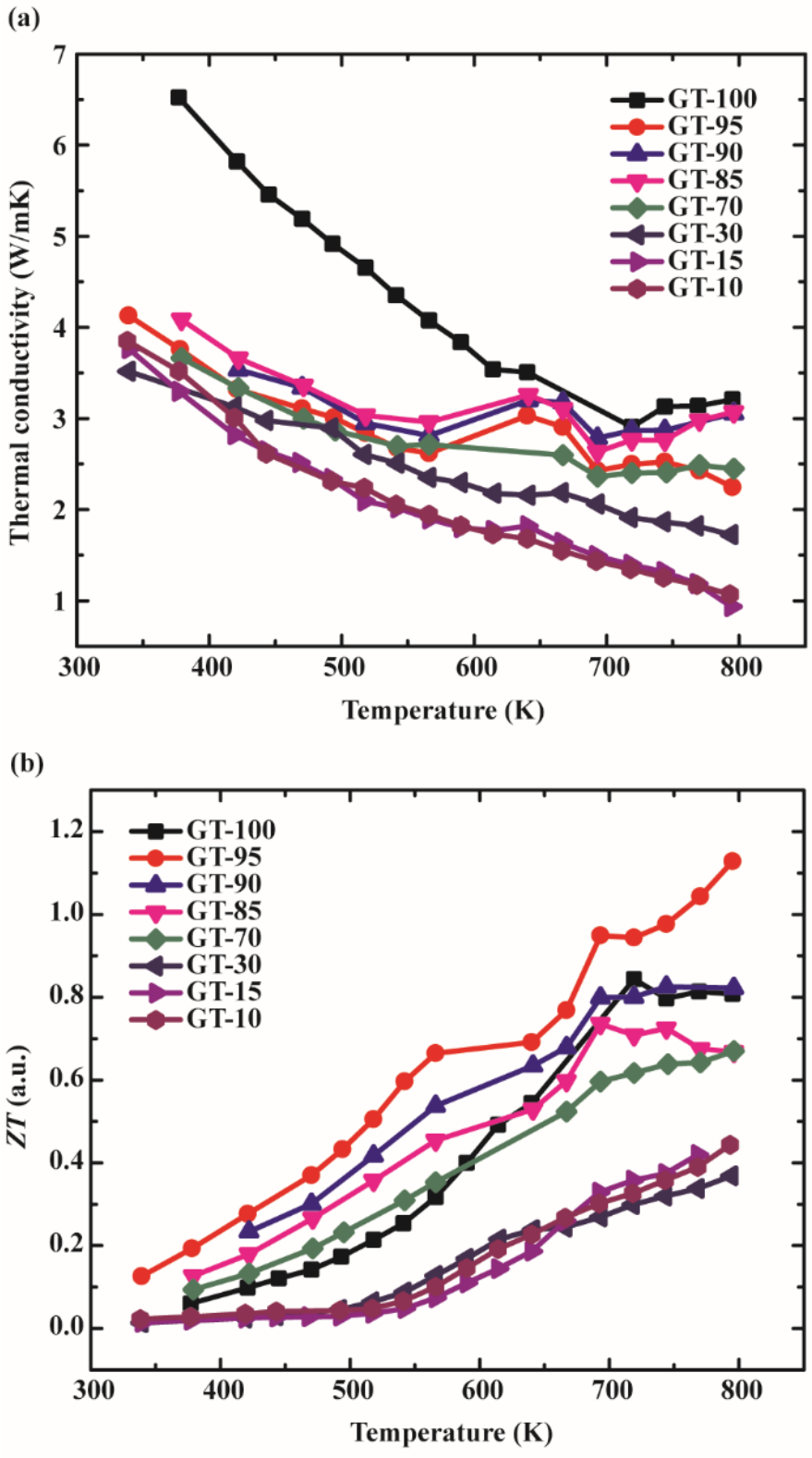

Figure 5.14 High temperature (a) thermal conductivity and (b) thermoelectric figure of merit ZT of 8 GeTe-$CuInTe_2$ composites.

5.7 Summary

The composites of GeTe and $CuInTe_2$ were successfully synthesized over a wide range of GeTe concentration from 0% to 100% using a solid state reaction method followed by hot pressing process. The phase separation of GeTe and $CuInTe_2$ major phases was confirmed by the powder XRD characterization, together with the BSE, SEM, and EDS microstructural study. TEM and nanoscale EDS results confirmed the formation and distribution of the nanoscale segregations. UPS and XPS results determined the Fermi level offset between GeTe and $CuInTe_2$ at room temperature and confirmed the existence of the high density of the nano $CuInTe_2$ segregations. Distinct scattering processes of carriers and phonons between the GeTe-rich and $CuInTe_2$-rich samples were characterized by low temperature thermoelectric transport properties measurement. By detailed theoretical and experimental analysis, we successfully enhanced the average power factor over a wide temperature range in the GeTe-$CuInTe_2$ composites. We proved that such enhancement originated from the temperature-dependent Fermi level offset between the matrix and secondary phase. Such temperature-dependent mechanism results in a temperature-dependent carrier concentration, which is beneficial for thermoelectric power factor enhancement. Small amount of $CuInTe_2$ secondary phases formed nano-size inclusions that strongly scatter phonons and resulted in a much lowered thermal conductivity in the GT-95 sample, confirmed by the BSE and SEM structural analysis and high temperature thermal conductivity measurement. The combined enhanced average power factor and the reduced thermal conductivity made a great improvement on the thermoelectric figure of merit of the GT-95 sample over the whole temperature range from 300 K to 800 K to a peak value of 1.12 at 800 K. The GeTe secondary phases in the $CuInTe_2$-rich samples acted as carrier donors by injecting

carriers at higher temperature into the $CuInTe_2$ phase. Such carrier transfer effect not only increased the electrical conductivity by increasing the carrier concentration, but also increased the Seebeck coefficient by enhancing the energy dependence of the mobility. As a result, the power factor tripled at approximately 600 K. We proposed that this novel secondary-phase doping method demonstrated in the GeTe-$CuInTe_2$ composites in this study can potentially be applied to other composite systems.

Chapter 6 Thermoelectric Power Factor Enhancement from High Order Band Dispersion

6.1 Introduction

The dispersion relation of low energy charge carriers near the band edge is usually parabolic, and thus the thermoelectric transport properties of most of the lightly or moderately doped materials can be well described with a parabolic band model. However, exceptions can exist under certain circumstances. Nonparabolicity has been demonstrated in various narrow bandgap semiconductors and the band dispersion follows the Kane relation.[51] Moreover, some low dimensional materials with high symmetry can have a band dispersion relation other than parabolic. A well-known example in 2D is graphene. In this chapter, we will study how changing the band dispersion influences the electrical transport properties in a thermoelectric material. We derived the transport coefficients by solving Boltzmann transport equation (BTE) with the relaxation time assumption. We also only consider the acoustic phonon scattering, which is the dominant scattering process at room temperature and above for most thermoelectric materials. The numerical calculation results indicate that higher order band dispersion relations indeed dramatically enhance the thermoelectric power factor compared to the parabolic band. Though engineering a material with high order band dispersion relation is very challenging, I propose that the results from this study may open up a new direction to enhance the electrical transport

properties of thermoelectric materials. In addition, real materials may have complex band structures that have parabolic and higher-order contributions,[62] and this work may be considered (from a power series context) quantify non-parabolic contributions to the thermoelectric properties.

6.2 Theory

For simplicity, an isotropic and spherical Fermi surface is assumed in the derivation, which can be extended to more complex cases by changing the one-dimensional integrals to three-dimensional. Applying the relaxation time assumption, the scattering term in the BTE is written as:

$$-\frac{f(E)-f_0(E)}{\tau} \qquad \textit{Equation 6.1}$$

where $f(E)$ is the perturbed distribution function of the charge carriers, $f_0(E)$ is the Fermi distribution function, and τ is the relaxation time. The band dispersion relation is isotropic for a spherical Fermi surface, and thus we have:

$$E(\vec{k}) = a|\vec{k}|^n \qquad \textit{Equation 6.2}$$

where a is the band dispersion proportionality constant that depends on the effective mass of the charge carriers, and n is the order index of the band dispersion. Then the density of states is:

$$\varphi(E) = \frac{8\pi}{(2\pi)^3}\frac{1}{an}\left(\frac{E}{a}\right)^{\frac{3-n}{n}} \qquad \textit{Equation 6.3}$$

with the band effective mass is defined as:

$$\frac{1}{m^*} = \frac{1}{\hbar^2}\frac{\partial^2 E(\vec{k})}{\partial \vec{k}^2} \qquad \textit{Equation 6.4}$$

For a parabolic band, band effective mass is independent of the energy of charge carriers; however, higher order dispersive bands have energy-dependent band effective mass. Such a difference makes it necessary to modify the simplified BTE:

$$\frac{q}{m^*}\left(\vec{E} + \vec{v} \times \vec{B}\right) \cdot \nabla_{\vec{v}} f(E) + \vec{v} \cdot \nabla_{\vec{r}} f(E) = -\frac{f(E) - f_0(E)}{\tau} \qquad \textit{Equation 6.5}$$

to a more generalized form:

$$\nabla_{\vec{p}} E(\vec{k}) \cdot \nabla_{\vec{r}} f(E) + q\left(\vec{E} + \nabla_{\vec{p}} E(\vec{k}) \times \vec{B}\right) \cdot \nabla_{\vec{p}} f(E) = -\frac{f(E) - f_0(E)}{\tau} \qquad \textit{Equation 6.6}$$

where $\vec{p}$ is the momentum of the charge carriers, $E(\vec{k})$ is the band dispersion relation, q is the charge of the carriers, $\vec{E}$ is the electrical field, and $\vec{B}$ is the magnetic field. The derivation of the transport coefficients of high order dispersive bands is quite similar with that for parabolic band,[38] though the assumption of a constant effective mass needs to be abandoned throughout the whole derivation, which I present below.

The solution of the BTE, $f(E)$, which is also the perturbed distribution function, is supposed to have the form of:

$$f(E) = f_0(E) - \vec{v}(E) \cdot \vec{c}(E)\frac{df_0}{dE} \qquad \textit{Equation 6.7}$$

where $\vec{c}(E)$ is a function of carrier energy. Plugging *Eqn.* 6.7 into *Eqn.* 6.6, the BTE can be rewritten as:

$$\vec{v}\cdot\nabla_{\vec{r}}\left(f_0-\vec{v}\cdot\vec{c}\frac{df_0}{dE}\right)+q\left(\vec{E}+\vec{v}\times\vec{B}\right)\cdot\nabla_{\vec{p}}\left(f_0-\vec{v}\cdot\vec{c}\frac{df_0}{dE}\right)=\frac{\vec{v}\cdot\vec{c}}{\tau}\frac{df_0}{dE} \qquad \textit{Equation 6.8}$$

where $\vec{\mathrm{v}}=\nabla_{\vec{\mathrm{p}}}\mathrm{E}\left(\vec{\mathrm{k}}\right)$ is the velocity of the charge carriers. So far, solving for $f(E)$ is equivalent to solving for $\vec{c}(E)$. Each term of the BTE can be further simplified in order to solve for $\vec{c}(E)$.

With the assumption of weak perturbation, the case for thermoelectric applications, the deviation of the perturbed distribution function and its derivative from the unperturbed functions is small:

$$\vec{v}\cdot\vec{c}\frac{df_0}{dE}\ll f_0 \qquad \textit{Equation 6.9}$$

$$\nabla_{\vec{r}}\left(\vec{v}\cdot\vec{c}\frac{df_0}{dE}\right)\ll\nabla_{\vec{r}}f_0 \qquad \textit{Equation 6.10}$$

$$\nabla_{\vec{p}}\left(\vec{v}\cdot\vec{c}\frac{df_0}{dE}\right)\ll\nabla_{\vec{p}}f_0 \qquad \textit{Equation 6.11}$$

Thus the first and the second term of the left side of the BTE (*Eqn.* 6.8) are approximated as:

$$\vec{v}\cdot\nabla_{\vec{r}}\left(f_0-\vec{v}\cdot\vec{c}\frac{df_0}{dE}\right)\approx\vec{v}\cdot\nabla_{\vec{r}}f_0=\vec{v}\cdot\nabla_{\vec{r}}\left(\frac{1}{exp\left(\frac{E-E_F}{k_BT}\right)+1}\right)=\vec{v}\cdot\nabla_{\vec{r}}\left(\frac{E-E_F}{k_BT}\right)\left(k_BT\frac{df_0}{dE}\right)=\vec{v}\cdot$$

$$\left\{-\left[k_BT\nabla_{\vec{r}}\left(\frac{E_F}{k_BT}\right)+\frac{E}{k_BT}\nabla_{\vec{r}}(k_BT)\right]\right\}\frac{df_0}{dE} \qquad \textit{Equation 6.12}$$

$$q\vec{E}\cdot\nabla_{\vec{p}}\left(f_0-\vec{v}\cdot\vec{c}\frac{df_0}{dE}\right)\approx q\vec{E}\cdot\nabla_{\vec{p}}f_0=q\vec{v}\cdot\vec{E}\frac{df_0}{dE} \qquad \textit{Equation 6.13}$$

Since $f_0=\frac{1}{exp\left(\frac{E-E_F}{k_BT}\right)+1}$ only depends on the energy of the carriers, thus:

$$q\vec{v}\times\vec{B}\cdot\nabla_{\vec{p}}f_o(E)=\ q\vec{v}\times\vec{B}\cdot\nabla_{\vec{p}}E\frac{df_0}{dE}=\ q\vec{v}\times\vec{B}\cdot\vec{v}\frac{df_0}{dE}=0 \qquad \textit{Equation 6.14}$$

Then the third term on the left side of the BTE is approximated as:

$$q\vec{v}\times\vec{B}\cdot\nabla_{\vec{p}}\left(f_0-\vec{v}\cdot\vec{c}\frac{df_0}{dE}\right)=-q\vec{v}\times\vec{B}\cdot\nabla_{\vec{p}}\left(\vec{v}\cdot\vec{c}\frac{df_0}{dE}\right) \qquad \textit{Equation 6.15}$$

where:

$$\nabla_{\vec{p}}\left(\vec{v}\cdot\vec{c}\frac{df_0}{dE}\right)=\nabla_{\vec{p}}\left(\nabla_{\vec{p}}E\cdot\vec{c}\frac{df_0}{dE}\right)=\left(\frac{\partial}{\partial p_x}\hat{\imath}+\frac{\partial}{\partial p_y}\hat{\jmath}+\frac{\partial}{\partial p_z}\hat{k}\right)\left[\left(\frac{\partial E}{\partial p_x}c_x+\frac{\partial E}{\partial p_y}c_y+\frac{\partial E}{\partial p_z}c_z\right)\frac{df_o}{dE}\right]=$$

$$\left\{\left(\frac{\partial^2E}{\partial p_x^2}c_x+\frac{\partial E}{\partial p_x}\frac{\partial c_x}{\partial p_x}+\frac{\partial^2E}{\partial p_x\partial p_y}c_y+\frac{\partial E}{\partial p_y}\frac{\partial c_y}{\partial p_x}+\frac{\partial^2E}{\partial p_x\partial p_z}c_z+\frac{\partial E}{\partial p_z}\frac{\partial c_z}{\partial p_x}\right)\frac{df_0}{dE}+\left(\frac{\partial E}{\partial p_x}c_x+\frac{\partial E}{\partial p_y}c_y+\right.\right.$$

$$\left.\left.\frac{\partial E}{\partial p_z}c_z\right)\frac{\partial}{\partial p_x}\frac{df_0}{dE}\right\}\hat{\imath}\ +\left\{\left(\frac{\partial^2E}{\partial p_y\partial p_x}c_x+\frac{\partial E}{\partial p_x}\frac{\partial c_x}{\partial p_y}+\frac{\partial^2E}{\partial p_y^2}c_y+\frac{\partial E}{\partial p_y}\frac{\partial c_y}{\partial p_y}+\frac{\partial^2E}{\partial p_y\partial p_z}c_z+\frac{\partial E}{\partial p_z}\frac{\partial c_z}{\partial p_y}\right)\frac{df_0}{dE}+\right.$$

$$\left.\left(\frac{\partial E}{\partial p_x}c_x+\frac{\partial E}{\partial p_y}c_y+\frac{\partial E}{\partial p_z}c_z\right)\frac{\partial}{\partial p_y}\frac{df_0}{dE}\right\}\hat{\jmath}\ +\left\{\left(\frac{\partial^2E}{\partial p_z\partial p_x}c_x+\frac{\partial E}{\partial p_x}\frac{\partial c_x}{\partial p_z}+\frac{\partial^2E}{\partial p_z\partial p_y}c_y+\frac{\partial E}{\partial p_y}\frac{\partial c_y}{\partial p_z}+\frac{\partial^2E}{\partial p_z^2}c_z+\right.\right.$$

$$\left.\left.\frac{\partial E}{\partial p_z}\frac{\partial c_z}{\partial p_z}\right)\frac{df_0}{dE}+\left(\frac{\partial E}{\partial p_x}c_x+\frac{\partial E}{\partial p_y}c_y+\frac{\partial E}{\partial p_z}c_z\right)\frac{\partial}{\partial p_z}\frac{df_0}{dE}\right\}\hat{k}\ =Matrix\left(\frac{1}{m^*}\right)\cdot\vec{c}\frac{df_0}{dE}+\left\{\left(\vec{v}\cdot\frac{\partial}{\partial p_x}\vec{c}\frac{df_0}{dE}\right)\hat{\imath}+\right.$$

$$\left.\left(\vec{v}\cdot\frac{\partial}{\partial p_y}\vec{c}\frac{df_0}{dE}\right)\hat{\jmath}+\left(\vec{v}\cdot\frac{\partial}{\partial p_z}\vec{c}\frac{df_0}{dE}\right)\hat{k}\right\}+\left(\vec{v}\cdot\vec{c}\frac{d^2f_0}{dE^2}\right)\vec{v}\ =Matrix\left(\frac{1}{m^*}\right)\cdot\vec{c}\frac{df_0}{dE}+\left(\vec{v}\cdot\frac{\partial}{\partial E}\vec{c}\frac{df_0}{dE}\right)\vec{v}+$$

$$\left(\vec{v}\cdot\vec{c}\frac{d^2f_0}{dE^2}\right)\vec{v} \qquad \textit{Equation 6.16}$$

where $Matrix\left(\frac{1}{m^*}\right)$ is the effective mass matrix for the high order dispersive band. A vector is defined as:

$$\vec{A} = Matrix\left(\frac{1}{m^*}\right)\cdot\vec{c}(E) = \begin{pmatrix} \frac{\partial^2 E}{\partial p_x^2} & \frac{\partial^2 E}{\partial p_x \partial p_y} & \frac{\partial^2 E}{\partial p_x \partial p_z} \\ \frac{\partial^2 E}{\partial p_y \partial p_x} & \frac{\partial^2 E}{\partial p_y^2} & \frac{\partial^2 E}{\partial p_y \partial p_z} \\ \frac{\partial^2 E}{\partial p_z \partial p_x} & \frac{\partial^2 E}{\partial p_z \partial p_y} & \frac{\partial^2 E}{\partial p_z^2} \end{pmatrix}\cdot\begin{pmatrix} c_x \\ c_y \\ c_z \end{pmatrix} =$$

$$\frac{1}{\hbar^2}\begin{pmatrix} \frac{\partial^2 E}{\partial k_x^2} & \frac{\partial^2 E}{\partial k_x \partial k_y} & \frac{\partial^2 E}{\partial k_x \partial k_z} \\ \frac{\partial^2 E}{\partial k_y \partial k_x} & \frac{\partial^2 E}{\partial k_y^2} & \frac{\partial^2 E}{\partial k_y \partial k_z} \\ \frac{\partial^2 E}{\partial k_z \partial k_x} & \frac{\partial^2 E}{\partial k_z \partial k_y} & \frac{\partial^2 E}{\partial k_z^2} \end{pmatrix}\cdot\begin{pmatrix} c_x \\ c_y \\ c_z \end{pmatrix} \qquad \textit{Equation 6.17}$$

Then, the third term (*Eqn.* 6.15) can be further simplified as:

$$The\ third\ left\ side\ term = -q\vec{v}\times\vec{B}\cdot\vec{A}\frac{df_0}{dE} = -q\vec{v}\cdot\left(\vec{B}\times\vec{A}\right)\frac{df_0}{dE} \qquad \textit{Equation 6.18}$$

Substituting *Eqn.* 6.12, 6.13, and 6.18 into the BTE, then we have:

$$\vec{v}\cdot\left\{-\left[k_B T\nabla_r\left(\frac{E_F}{k_B T}\right)+\frac{E}{k_B T}\nabla_r(k_B T)\right]\right\}\frac{df_0}{dE} + q\vec{v}\cdot\vec{E}\frac{df_0}{dE} - q\vec{v}\cdot\left(\vec{B}\times\vec{A}\right)\frac{df_0}{dE} = \frac{\vec{v}\cdot\vec{c}}{\tau}\frac{df_0}{dE}$$

Equation 6.19

The solution $\vec{c}(E)$ is derived by rearranging the terms in *Eqn.* 6.19 as:

$$\vec{c} = -q\tau\left(\vec{B}\times\vec{A}\right) + q\tau\vec{E} - \tau k_B T\nabla_r\left(\frac{E_F}{k_B T}\right) - \tau\frac{E}{k_B T}\nabla_r(k_B T) \qquad \textit{Equation 6.20}$$

Without losing generality, the electric field and temperature gradient are set in the *x*-*y* plane and the magnetic field is set along the *z* direction:

$$\vec{E} = E_x\hat{\imath} + E_y\hat{\jmath};\ \vec{B} = B_z\hat{k} \qquad \textit{Equation 6.21}$$

Then the vector $\vec{c}(E)$ only contains *x* and *y* components:

$$\begin{cases} c_x = \beta + q\tau B_z \frac{1}{\hbar^2}\left(\frac{\partial^2 E}{\partial k_y \partial k_x} c_x + \frac{\partial^2 E}{\partial k_y^2} c_y\right) \\ c_y = \gamma - q\tau B_z \frac{1}{\hbar^2}\left(\frac{\partial^2 E}{\partial k_x^2} c_x + \frac{\partial^2 E}{\partial k_x \partial k_y} c_y\right) \end{cases} \qquad \textit{Equation 6.22}$$

where,

$$\beta = \tau\left\{qE_x - k_B T \frac{\partial}{\partial x}\left(\frac{E_F}{k_B T}\right) - \frac{E}{k_B T}\frac{\partial}{\partial x}(k_B T)\right\} \qquad \textit{Equation 6.23}$$

$$\gamma = \tau\left\{qE_y - k_B T \frac{\partial}{\partial y}\left(\frac{E_F}{k_B T}\right) - \frac{E}{k_B T}\frac{\partial}{\partial y}(k_B T)\right\} \qquad \textit{Equation 6.24}$$

With the weak field assumption, the *x* and *y* components of the solution $\vec{c}(E)$ can be further simplified as:

$$\begin{cases} c_x = \left\{1 + q\tau B_z \frac{\partial^2 E}{\partial k_x \partial k_y}\frac{1}{\hbar^2}\right\}\beta + q\tau B_z \frac{\partial^2 E}{\partial k_y^2}\frac{1}{\hbar^2}\gamma \\ c_y = -q\tau B_z \frac{\partial^2 E}{\partial k_x^2}\frac{1}{\hbar^2}\beta + \left\{1 - q\tau B_z \frac{\partial^2 E}{\partial k_x \partial k_y}\frac{1}{\hbar^2}\right\}\gamma \end{cases} \qquad \textit{Equation 6.25}$$

With the perturbed distribution function solved, thermoelectric transport coefficients can now be calculated. The current density along the *x*-direction is the integral over the whole *k*-space:

$$j_x = \sum_{k_x,k_y,k_z} q \frac{V(k_x,k_y,k_z)n(k_x,k_y,k_z)}{dSdt} = \iiint dk_x dk_y dk_z q \frac{v_x(k_x,k_y,k_z)dSdtf(k_x,k_y,k_z)\varphi(k_x,k_y,k_z)}{dSdt} =$$

$$\iiint dk_x dk_y dk_z q\, v_x(k_x,k_y,k_z) f(k_x,k_y,k_z)\varphi(k_x,k_y,k_z) \qquad \textit{Equation 6.26}$$

where $V(k_x,k_y,k_z)$ is the volume in the real space in which the electrons or holes with the momentum (k_x,k_y,k_z) will travel through the cross section dS in the time interval dt; $n(k_x,k_y,k_z)$ is the electrons or holes concentration with the momentum (k_x,k_y,k_z); $v_x(k_x,k_y,k_z)$ is the velocity of the electrons or holes with the momentum (k_x,k_y,k_z) in the *x*-

direction; $f(k_x, k_y, k_z)$ is the distribution function of the electrons or holes with the momentum (k_x, k_y, k_z); and $\varphi(k_x, k_y, k_z)$ is the density of states of electrons or holes with the momentum (k_x, k_y, k_z). For an isotropic and spherical Fermi surface as assumed, the integral can be simplified as:

$$j_x = \sum_{each\ shell} \iiint_{\substack{Constant\\ Energy\\ Shell}} dk_x dk_y dk_z\, q v_x(k_x, k_y, k_z) f(k_x, k_y, k_z) \varphi(k_x, k_y, k_z)$$

Equation 6.27

Since $f(k_x, k_y, k_z)$ is only a function of the energy of the carriers and:

$$\varphi(k_x, k_y, k_z) = \frac{2}{(2\pi)^3} \qquad \textit{Equation 6.28}$$

Thus we have:

$$j_x = \sum_{each\ shell} \iiint_{\substack{Constant\\ Energy\\ Shell}} dk_x dk_y dk_z\, q v_x(k_x, k_y, k_z) f(E) \frac{2}{(2\pi)^3} \qquad \textit{Equation 6.29}$$

Substitute $f(E)$ solved from BTE into *Eqn.* 6.28, we have:

$$j_x = \sum_{each\ shell} \iiint_{\substack{Constant\\ Energy\\ Shell}} dk_x dk_y dk_z\, q v_x(k_x, k_y, k_z) \left[f_0(E) - \vec{v}(E) \cdot \vec{c}(E) \frac{df_0}{dE} \right] \frac{2}{(2\pi)^3} =$$

$$\sum_{each\ shell} \iiint_{\substack{Constant\\ Energy\\ Shell}} dk_x dk_y dk_z q v_x \left\{ f_0(E) - v_x c_x \frac{df_0}{dE} - v_y c_y \frac{df_0}{dE} \right\} \frac{2}{(2\pi)^3}$$

Equation 6.30

Similarly, the current density in the *y*-direction is:

$$j_y = \sum_{each\ shell} \iiint_{\substack{Constant\\Energy\\Shell}} dk_x dk_y dk_z q v_y \left\{ f_0(E) - v_x c_x \frac{df_0}{dE} - v_y c_y \frac{df_0}{dE} \right\} \frac{2}{(2\pi)^3}$$

Equation 6.31

Several terms in the integrals are zero due to the high symmetry of the constant-energy surface:

$$\iiint_{\substack{Constant\\Energy\\Shell}} dk_x dk_y dk_z\, q v_x f_0(E) \frac{2}{(2\pi)^3} = \iiint_{\substack{Constant\\Energy\\Shell}} dk_x dk_y dk_z\, q v_y f_0(E) \frac{2}{(2\pi)^3} = 0$$

Equation 6.32

For high order dispersive bands:

$$E = a\left|\vec{k}\right|^n = a\left(\sqrt{k_x^2 + k_y^2 + k_z^2}\right)^n$$ *Equation 6.33*

The derivatives of the carrier energy with respect to the momentum are:

$$\frac{\partial^2 E}{\partial k_x^2} = an\left(k_x^2 + k_y^2 + k_z^2\right)^{\frac{n}{2}-1} + an(n-2)k_x^2\left(k_x^2 + k_y^2 + k_z^2\right)^{\frac{n}{2}-2}$$

Equation 6.34

$$\frac{\partial^2 E}{\partial k_y^2} = an\left(k_x^2 + k_y^2 + k_z^2\right)^{\frac{n}{2}-1} + an(n-2)k_y^2\left(k_x^2 + k_y^2 + k_z^2\right)^{\frac{n}{2}-2}$$

Equation 6.35

$$\frac{\partial^2 E}{\partial k_x \partial k_y} = an(n-2)k_x k_y\left(k_x^2 + k_y^2 + k_z^2\right)^{\frac{n}{2}-2}$$ *Equation 6.36*

$$v_x = \frac{1}{\hbar}\frac{\partial E}{\partial k_x} = \frac{1}{\hbar} ank_x\left(k_x^2 + k_y^2 + k_z^2\right)^{\frac{n}{2}-1}$$ *Equation 6.37*

and

$$v_y = \frac{1}{\hbar}\frac{\partial E}{\partial k_y} = \frac{1}{\hbar} ank_y\left(k_x^2 + k_y^2 + k_z^2\right)^{\frac{n}{2}-1} \qquad \textit{Equation 6.38}$$

Substitute *Eqn.* 6.33 to 6.37 into the current density integrals, we have:

$$\begin{aligned}
j_x = \sum_{each\ shell} \iiint_{\substack{Energy\\Constant\\Shell}} dk_x dk_y dk_z q \frac{1}{\hbar} ank_x \left(\left|\vec{k}\right|^2\right)^{\frac{n}{2}-1} \Bigg\{ -\frac{1}{\hbar} ank_x \left(\left|\vec{k}\right|^2\right)^{\frac{n}{2}-1} \Bigg[\Bigg\{ 1 \\
+ q\tau B_z an(n-2)k_x k_y \left(\left|\vec{k}\right|^2\right)^{\frac{n}{2}-2} \frac{1}{\hbar^2} \Bigg\} \beta \\
+ q\tau B_z \left[an\left(\left|\vec{k}\right|^2\right)^{\frac{n}{2}-1} + an(n-2)k_y^2 \left(\left|\vec{k}\right|^2\right)^{\frac{n}{2}-2} \right] \frac{1}{\hbar^2}\gamma \Bigg] \frac{df_0}{dE} \\
- \frac{1}{\hbar} ank_y \left(\left|\vec{k}\right|^2\right)^{\frac{n}{2}-1} \Bigg[-q\tau B_z \left[an\left(\left|\vec{k}\right|^2\right)^{\frac{n}{2}-1} + an(n-2)k_x^2 \left(\left|\vec{k}\right|^2\right)^{\frac{n}{2}-2} \right] \frac{1}{\hbar^2}\beta \\
+ \left\{ 1 - q\tau B_z an(n-2)k_x k_y \left(\left|\vec{k}\right|^2\right)^{\frac{n}{2}-2} \frac{1}{\hbar^2} \right\} \gamma \Bigg] \frac{df_0}{dE} \Bigg\} \frac{2}{(2\pi)^3} \\
= \sum_{each\ shell} \iiint_{\substack{Energy\\Constant\\Shell}} dk_x dk_y dk_z q \frac{1}{\hbar} ank_x \left(\left|\vec{k}\right|^2\right)^{\frac{n}{2}-1} \Bigg\{ -\frac{1}{\hbar} ank_x \left(\left|\vec{k}\right|^2\right)^{\frac{n}{2}-1} \Bigg[\beta \\
+ q\tau B_z \left[an\left(\left|\vec{k}\right|^2\right)^{\frac{n}{2}-1} \right] \frac{1}{\hbar^2}\gamma \Bigg] \frac{df_0}{dE} \Bigg\} \frac{2}{(2\pi)^3} \\
= - \sum_{each\ shell} \iiint_{\substack{Energy\\Constant\\Shell}} dk_x dk_y dk_z q \frac{1}{\hbar^2} a^2 n^2 k_x^2 \left(\left|\vec{k}\right|^2\right)^{n-2} \Bigg[\beta \\
+ q\tau B_z an\left(\left|\vec{k}\right|^2\right)^{\frac{n}{2}-1} \frac{1}{\hbar^2}\gamma \Bigg] \frac{df_0}{dE} \frac{2}{(2\pi)^3}
\end{aligned}$$

Equation 6.39

Similarly, the current density in the *y* direction is:

$$j_y = \sum_{each\ shell} \iiint_{\substack{Energy\\Constant\\Shell}} dk_x dk_y dk_z q v_y \left\{ -v_x c_x \frac{df_0}{dE} - v_y c_y \frac{df_0}{dE} \right\} \frac{2}{(2\pi)^3}$$

$$= \sum_{each\ shell} \iiint_{\substack{Energy\\Constant\\Shell}} dk_x dk_y dk_z q \frac{1}{\hbar} a n k_y \left(\left| \vec{k} \right|^2 \right)^{\frac{n}{2}-1} \left\{ -\frac{1}{\hbar} a n k_x \left(\left| \vec{k} \right|^2 \right)^{\frac{n}{2}-1} \left[\left\{ 1 \right.\right.\right.$$

$$\left. + q\tau B_z a n (n-2) k_x k_y \left(\left| \vec{k} \right|^2 \right)^{\frac{n}{2}-2} \frac{1}{\hbar^2} \right\} \beta + q\tau B_z \left[a n \left(\left| \vec{k} \right|^2 \right)^{\frac{n}{2}-1} + a n (n-2) k_y^2 \left(\left| \vec{k} \right|^2 \right)^{\frac{n}{2}-2} \right] \frac{1}{\hbar^2} \gamma \right] \frac{df_0}{dE}$$

$$- \frac{1}{\hbar} a n k_y \left(\left| \vec{k} \right|^2 \right)^{\frac{n}{2}-1} \left[-q\tau B_z \left[a n \left(\left| \vec{k} \right|^2 \right)^{\frac{n}{2}-1} + a n (n-2) k_x^2 \left(\left| \vec{k} \right|^2 \right)^{\frac{n}{2}-2} \right] \frac{1}{\hbar^2} \beta \right.$$

$$\left. + \left\{ 1 - q\tau B_z a n (n-2) k_x k_y \left(\left| \vec{k} \right|^2 \right)^{\frac{n}{2}-2} \frac{1}{\hbar^2} \right\} \gamma \right] \frac{df_0}{dE} \Bigg\} \frac{2}{(2\pi)^3}$$

$$= \sum_{each\ shell} \iiint_{\substack{Energy\\Constant\\Shell}} dk_x dk_y dk_z q \frac{1}{\hbar} a n k_y \left(\left| \vec{k} \right|^2 \right)^{\frac{n}{2}-1} \left\{ -\frac{1}{\hbar} a n k_y \left(\left| \vec{k} \right|^2 \right)^{\frac{n}{2}-1} \left[-q\tau B_z a n \left(\left| \vec{k} \right|^2 \right)^{\frac{n}{2}-1} \frac{1}{\hbar^2} \beta \right.\right.$$

$$\left. \left. + \gamma \right] \frac{df_0}{dE} \right\} \frac{2}{(2\pi)^3}$$

$$= \sum_{each\ shell} \iiint_{\substack{Energy\\Constant\\Shell}} dk_x dk_y dk_z q \frac{1}{\hbar^2} a^2 n^2 k_y^2 \left(\left| \vec{k} \right|^2 \right)^{n-2} \left[q\tau B_z a n \left(\left| \vec{k} \right|^2 \right)^{\frac{n}{2}-1} \frac{1}{\hbar^2} \beta - \gamma \right] \frac{df_0}{dE} \frac{2}{(2\pi)^3}$$

Equation 6.40

After changing the Cartesian coordinates to the spherical coordinates, the integrals can be simplified as:

$$j_x = -\int_0^{\infty} dk \int_0^{2\pi} d\varphi \int_0^{\pi} d\theta \frac{2}{(2\pi)^3} \frac{df_0}{dE} q \frac{1}{\hbar^2} a^2 n^2 k^{2n} sin^3\theta cos^2\varphi [\beta + \delta ank^{n-2}\gamma]$$

$$= -\int_0^{\infty} dE \frac{1}{\hbar^2} \frac{qan}{3\pi^2} \frac{df_0}{dE} \left(\frac{E}{a}\right)^{\frac{n+1}{n}} \beta - \int_0^{\infty} dE \frac{1}{\hbar^2} \frac{qa^2 n^2 \delta}{3\pi^2} \frac{df_0}{dE} \left(\frac{E}{a}\right)^{\frac{2n-1}{n}} \gamma$$

$$= -\int_0^{\infty} dE \frac{1}{\hbar^2} \frac{qa^{-\frac{1}{n}} n}{3\pi^2} \frac{df_0}{dE} E^{\frac{n+1}{n}} \beta - \int_0^{\infty} dE \frac{1}{\hbar^2} \frac{qa^{\frac{1}{n}} n^2 \delta}{3\pi^2} \frac{df_0}{dE} E^{\frac{2n-1}{n}} \gamma$$

Equation 6.41

$$j_y = \int_0^{\infty} dk \int_0^{2\pi} d\varphi \int_0^{\pi} d\theta \frac{2}{(2\pi)^3} \frac{df_0}{dE} q \frac{1}{\hbar^2} a^2 n^2 k^{2n} sin^3\theta sin^2\varphi [\delta ank^{n-2}\beta - \gamma]$$

$$= \int_0^{\infty} dE \frac{1}{\hbar^2} \frac{qa^2 n^2 \delta}{3\pi^2} \frac{df_0}{dE} \left(\frac{E}{a}\right)^{\frac{2n-1}{n}} \beta - \int_0^{\infty} dE \frac{1}{\hbar^2} \frac{qan}{3\pi^2} \frac{df_0}{dE} \left(\frac{E}{a}\right)^{\frac{n+1}{n}} \gamma$$

$$= \int_0^{\infty} dE \frac{1}{\hbar^2} \frac{qa^{\frac{1}{n}} n^2 \delta}{3\pi^2} \frac{df_0}{dE} E^{\frac{2n-1}{n}} \beta - \int_0^{\infty} dE \frac{1}{\hbar^2} \frac{qa^{-\frac{1}{n}} n}{3\pi^2} \frac{df_0}{dE} E^{\frac{n+1}{n}} \gamma$$

Equation 6.42

where $\delta = \frac{q\tau B_z}{\hbar^2}$, and $k = \left|\vec{k}\right|$. Substitute β and γ into the integrals, we have:

$$j_x = -\int_0^\infty dE \frac{1}{\hbar^2} \frac{q a^{-\frac{1}{n}} n}{3\pi^2} \frac{df_0}{dE} E^{\frac{n+1}{n}} \tau \left\{ qE_x - k_B T \frac{\partial}{\partial x}\left(\frac{E_F}{k_B T}\right) - \frac{E}{k_B T}\frac{\partial}{\partial x}(k_B T) \right\}$$

$$- \int_0^\infty dE \frac{1}{\hbar^2} \frac{q a^{\frac{1}{n}} n^2 \delta}{3\pi^2} \frac{df_0}{dE} E^{\frac{2n-1}{n}} \tau \left\{ qE_y - k_B T \frac{\partial}{\partial y}\left(\frac{E_F}{k_B T}\right) - \frac{E}{k_B T}\frac{\partial}{\partial y}(k_B T) \right\}$$

$$= -\int_0^\infty dE \frac{1}{\hbar^2} \frac{q a^{-\frac{1}{n}} n}{3\pi^2} \frac{df_0}{dE} E^{\frac{n+1}{n}} \tau k_B T \left\{ -\frac{\partial}{\partial x}\left(\frac{qV + E_F}{k_B T}\right) + qV \frac{\partial}{\partial x}\left(\frac{1}{k_B T}\right) \right.$$

$$\left. + E \frac{\partial}{\partial x}\left(\frac{1}{k_B T}\right) \right\}$$

$$- \int_0^\infty dE \frac{1}{\hbar^2} \frac{q a^{\frac{1}{n}} n^2 \delta}{3\pi^2} \frac{df_0}{dE} E^{\frac{2n-1}{n}} \tau k_B T \left\{ -\frac{\partial}{\partial y}\left(\frac{qV + E_F}{k_B T}\right) + qV \frac{\partial}{\partial y}\left(\frac{1}{k_B T}\right) \right.$$

$$\left. + E \frac{\partial}{\partial y}\left(\frac{1}{k_B T}\right) \right\}$$

Equation 6.43

$$j_y = \int_0^\infty dE \frac{1}{\hbar^2} \frac{q a^{\frac{1}{n}} n^2 \delta}{3\pi^2} \frac{df_0}{dE} E^{\frac{2n-1}{n}} \tau k_B T \left\{ -\frac{\partial}{\partial x}\left(\frac{qV + E_F}{k_B T}\right) + qV \frac{\partial}{\partial x}\left(\frac{1}{k_B T}\right) + E \frac{\partial}{\partial x}\left(\frac{1}{k_B T}\right) \right\}$$

$$- \int_0^\infty dE \frac{1}{\hbar^2} \frac{q a^{-\frac{1}{n}} n}{3\pi^2} \frac{df_0}{dE} E^{\frac{n+1}{n}} \tau k_B T \left\{ -\frac{\partial}{\partial y}\left(\frac{qV + E_F}{k_B T}\right) + qV \frac{\partial}{\partial y}\left(\frac{1}{k_B T}\right) \right.$$

$$\left. + E \frac{\partial}{\partial y}\left(\frac{1}{k_B T}\right) \right\}$$

Equation 6.44

where $\vec{E} = -\nabla_{\vec{r}} V$. Define integrals:

$$\begin{cases} I_1 = \int_0^\infty dE \frac{1}{\hbar^2} \frac{a^{-\frac{1}{n}} n}{3\pi^2} \frac{df_0}{dE} E^{\frac{n+1}{n}} \tau \\ I_2 = \int_0^\infty dE \frac{1}{\hbar^2} \frac{a^{-\frac{1}{n}} n}{3\pi^2} \frac{df_0}{dE} E^{\frac{2n+1}{n}} \tau \\ I_3 = \int_0^\infty dE \frac{1}{\hbar^2} \frac{a^{\frac{1}{n}} n^2 \delta}{3\pi^2} \frac{df_0}{dE} E^{\frac{2n-1}{n}} \tau \\ I_4 = \int_0^\infty dE \frac{1}{\hbar^2} \frac{a^{\frac{1}{n}} n^2 \delta}{3\pi^2} \frac{df_0}{dE} E^{\frac{3n-1}{n}} \tau \end{cases}$$

Equation 6.45

Then, *Eqn.* 6.43 and 6.44 can be rearranged:

$$\frac{\partial}{\partial x}\left(\frac{qV + E_F}{k_B T}\right) = \frac{I_1}{k_B T (I_1^2 + I_3^2)} \frac{j_x}{q} - \frac{I_3}{k_B T (I_1^2 + I_3^2)} \frac{j_y}{q} + \left(qV + \frac{I_1 I_2 + I_3 I_4}{I_1^2 + I_3^2}\right) \frac{\partial}{\partial x}\left(\frac{1}{k_B T}\right) + \left(\frac{I_1 I_4 - I_2 I_3}{I_1^2 + I_3^2}\right) \frac{\partial}{\partial y}\left(\frac{1}{k_B T}\right)$$

Equation 6.46

$$\frac{\partial}{\partial y}\left(\frac{qV + E_F}{k_B T}\right) = \frac{I_3}{k_B T (I_1^2 + I_3^2)} \frac{j_x}{q} + \frac{I_1}{k_B T (I_1^2 + I_3^2)} \frac{j_y}{q} - \left(\frac{I_1 I_4 - I_2 I_3}{I_1^2 + I_3^2}\right) \frac{\partial}{\partial x}\left(\frac{1}{k_B T}\right) + \left(qV + \frac{I_1 I_2 + I_3 I_4}{I_1^2 + I_3^2}\right) \frac{\partial}{\partial y}\left(\frac{1}{k_B T}\right)$$

Equation 6.47

Define the quantities:

$$\begin{cases} A_{11} = \frac{I_1}{k_B T (I_1^2 + I_3^2)} \\ A_{12} = \frac{I_3}{k_B T (I_1^2 + I_3^2)} \\ A_{13} = \left(qV + \frac{I_1 I_2 + I_3 I_4}{I_1^2 + I_3^2}\right) \\ A_{14} = \left(\frac{I_1 I_4 - I_2 I_3}{I_1^2 + I_3^2}\right) \end{cases}$$

Equation 6.48

Then *Eqn.* 6.46 and 6.47 turn into a more compact form as:

$$\begin{cases} \frac{\partial}{\partial x}\left(\frac{qV+E_F}{k_BT}\right) = A_{11}\frac{j_x}{q} - A_{12}\frac{j_y}{q} + A_{13}\frac{\partial}{\partial x}\left(\frac{1}{kT}\right) + A_{14}\frac{\partial}{\partial y}\left(\frac{1}{kT}\right) \\ \frac{\partial}{\partial y}\left(\frac{qV+E_F}{k_BT}\right) = A_{12}\frac{j_x}{q} + A_{11}\frac{j_y}{q} - A_{14}\frac{\partial}{\partial x}\left(\frac{1}{kT}\right) + A_{13}\frac{\partial}{\partial y}\left(\frac{1}{kT}\right) \end{cases} \quad \textit{Equation 6.49}$$

The electrical transport coefficients can now be calculated based on their own definitions. The electrical conductivity is defined as:

$$\sigma = \frac{j_x}{E_x} \quad \textit{Equation 6.50}$$

with conditions:

$$\frac{dT}{dx} = \frac{dT}{dy} = j_y = 0 \quad \textit{Equation 6.51}$$

Substituting *Eqn.* 6.48, 6.50, and 6.51 into 6.49, then we have:

$$\sigma = -\frac{q^2}{k_BTA_{11}} = -\frac{q^2\left(I_1^2+I_3^2\right)}{I_1} \quad \textit{Equation 6.52}$$

The Seebeck coefficient is defined as:

$$S = E_x/\frac{dT}{dx} \quad \textit{Equation 6.53}$$

with conditions:

$$j_x = j_y = \frac{dT}{dy} = 0 \quad \textit{Equation 6.54}$$

Plugging *Eqn.* 6.48, 6.53, and 6.54 into 6.49, then we have:

$$S = \frac{k_B}{q}\left(\frac{A_{13}}{k_BT} - \frac{qV+E_F}{k_BT}\right) = \frac{k_B}{q}\left(\frac{qV+\frac{I_1I_2+I_3I_4}{I_1^2+I_3^2}}{k_BT} - \frac{qV+E_F}{k_BT}\right) = \frac{k_B}{q}\left(\frac{I_1I_2+I_3I_4}{k_BT\left(I_1^2+I_3^2\right)} - \frac{E_F}{k_BT}\right)$$

Equation 6.55

The Hall coefficient is defined as:

$$R_H = \frac{E_y}{j_x B_z} \qquad \textit{Equation 6.56}$$

with conditions:

$$j_y = \frac{dT}{dy} = \frac{dT}{dx} = 0 \qquad \textit{Equation 6.57}$$

Substitute *Eqn.* 6.55 and 6.56 into 6.48, then we have:

$$R_H = -\frac{k_B T}{q^2 B_z} A_{12} = -\frac{k_B T}{q^2 B_z} \frac{I_3}{k_B T (I_1^2 + I_3^2)} = -\frac{1}{q^2 B_z} \frac{I_3}{I_1^2}$$

Equation 6.58

With the energy-dependent relaxation time having the form of:

$$\tau = w E^r \qquad \textit{Equation 6.59}$$

where w is the proportionality constant and r is the scattering parameter depending on the scattering processes, the transport coefficients can be written as:

$$\sigma = q^2 \frac{n}{3\hbar^2} \frac{1}{\pi^2} a^{-\frac{1}{n}} w \left(\frac{n+1}{n} + r\right) (k_B T)^{\frac{n+1}{n}+r} F_{\frac{1}{n}+r}(\eta^*) \qquad \textit{Equation 6.60}$$

$$S = \frac{k_B}{q} \left\{ \frac{\frac{2n+1}{n}+r}{\frac{n+1}{n}+r} \cdot \frac{F_{\frac{n+1}{n}+r}(\eta^*)}{F_{\frac{1}{n}+r}(\eta^*)} - \eta^* \right\} \qquad \textit{Equation 6.61}$$

$$R_H = \frac{1}{q} \left(\frac{a}{k_B T}\right)^{\frac{3}{n}} 3\pi^2 \frac{\left(\frac{2n-1}{n}+2p\right)}{\left(\frac{n+1}{n}+p\right)^2} \frac{F_{\frac{n-1}{n}+2p}(\eta^*)}{\left(F_{\frac{1}{n}+p}(\eta^*)\right)^2} \qquad \textit{Equation 6.62}$$

where $\eta^* = \frac{E_F}{k_B T}$ is the reduced Fermi level, and $F_j(\eta^*) = \int_0^\infty \frac{\eta^j}{1+exp(\eta-\eta^*)} d\eta$ is the Fermi integral of jth order.

6.3 Results and Discussion

Firstly, we explore the influence of doping on the electrical transport properties for high order dispersive bands. Since we only focus on the transport properties near room temperature, at which acoustic phonon scattering processes dominate, the dopants are considered to be fully ionized and the carrier concentration is equal to the doping concentration:

$$p = \frac{8\pi}{(2\pi)^3} \frac{1}{an} \left(\frac{1}{a}\right)^{\frac{3-n}{n}} (kT)^{\frac{3}{n}} F_{\frac{3-n}{n}}(\eta^*) = N_A \qquad \textit{Equation 6.63}$$

where p is the hole concentration and N_A is the concentration of the impurities. The proportionality constant a in *Eqn.* 6.2 is set to a function of band dispersion order as:

$$a = e \times \text{Å}^n = (1.6 \times 10^{-19} C) \times (10^{-10} m)^n \qquad \textit{Equation 6.64}$$

For acoustic scattering in parabolic bands, the scattering parameter r is equal to -0.5. This value originates from the results of the Fermi Golden Rule that the probability of scattering carriers from their initial states to final states is proportional to the density of the final states:

$$\frac{1}{\tau} \propto DOS = \varphi(E) \qquad \textit{Equation 6.65}$$

Thus, both the scattering parameter r and the proportionality parameter w are functions of the band dispersion order n as:

$$w = \frac{n}{2}\left(e \times \text{Å}^2\right)^{-\frac{3}{2}}\left(e \times \text{Å}^n\right)^{\frac{3}{n}} w_0 \qquad \textit{Equation 6.66}$$

$$p = 1 - \frac{3}{n} \qquad \textit{Equation 6.67}$$

The Fermi level, electrical conductivity, Seebeck coefficient, and power factor are then numerically calculated as a function of doping concentration. The results are shown in Fig. 6.1. In this chapter, I use m^{-3} instead of cm^{-3} as the unit of carrier concentration.

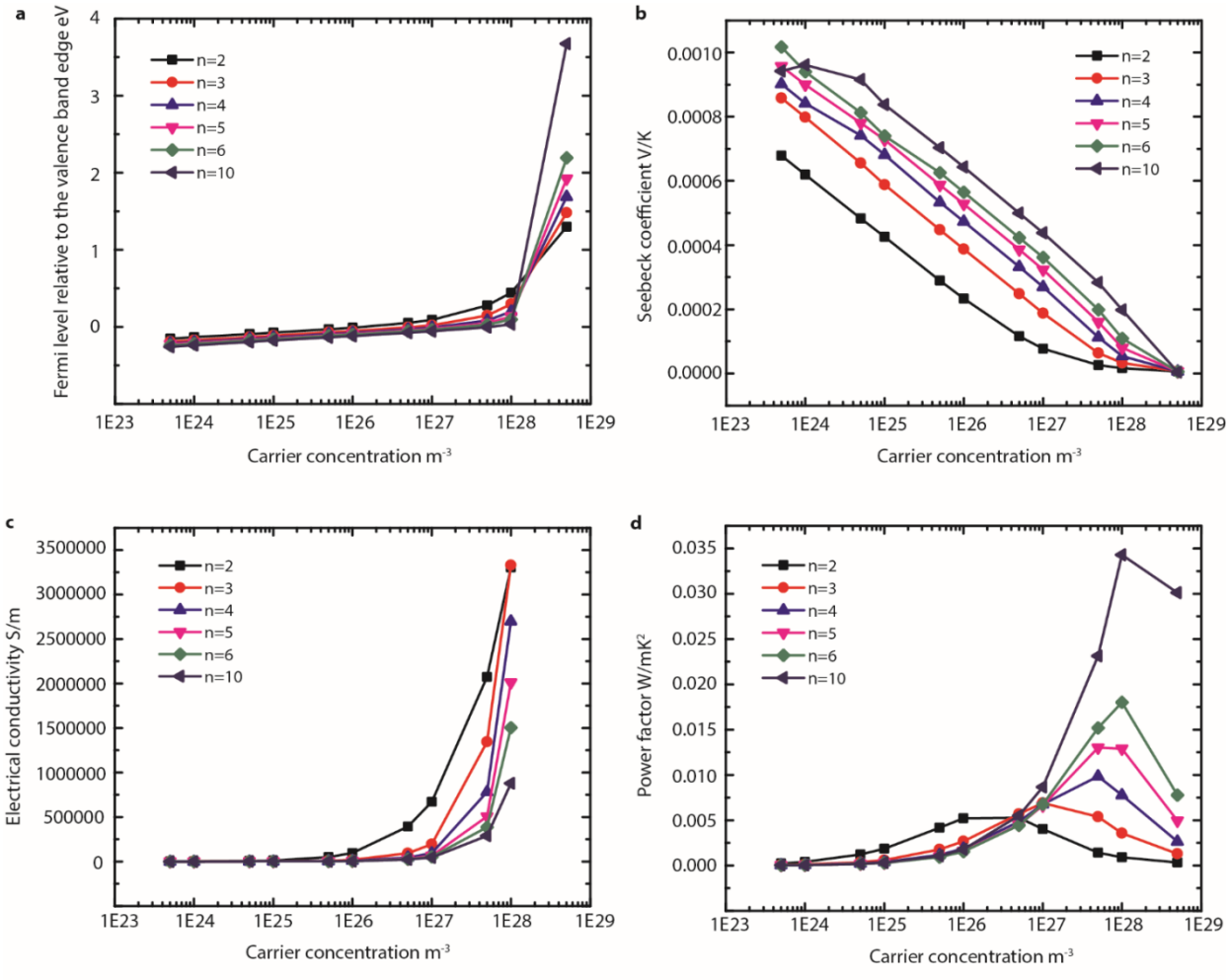

Figure 6.1 Carrier concentration dependent (a) Fermi level, (b) Seebeck coefficient, (c) electrical conductivity, and (d) power factor for various band dispersions with acoustic phonon scattering parameter at 300 K.

Without losing generality, we select holes as the charge carriers and thus all conduction is *p*-type. The Fermi level is pushed into the valence band as the doping concentration increases for all the band dispersion orders studied here. Below the doping concentration of 10^{28} m^{-3}, the Fermi level of lower order dispersive bands is pushed deeper into the valence band. This trend is reversed as the doping concentration increases above 10^{28} m^{-3}. This feature is caused by the change of the density of states as the band dispersion index increases, which will be discussed later. The electrical conductivity increases significantly with the increasing doping concentration. As the doping concentration increases above 10^{22} m^{-3}, lower order dispersive bands exhibit higher electrical conductivity. Expectedly, the Seebeck coefficient follows the opposite trend, decreasing as the carrier concentration increases. Higher band dispersion order leads to a larger thermopower. As a result, the peak power factor is enhanced by almost an order of magnitude as the band dispersion order n increases from 2 to 10, as shown in Fig. 6.1d. Interestingly, the optimized doping concentration for the peak power factor also moves to a higher value as the band dispersion order increases.

It is worth noting that the discussion with the acoustic phonon scattering assumption is only valid for $n \geq 2$. If we apply the model to linearly dispersive band, an infinite thermopower and zero electrical conductivity will be obtained. It is not hard to see that the parameter A_{11} is zero and A_{13} is infinity for linear bands. This indicates that the current along *x* or *y* direction does not contribute to an electrochemical potential drop along that direction, while a finite temperature gradient yields an infinite electrochemical potential drop. The unreasonable results are probably caused by the assumption that only acoustic phonon scattering exists. On the other

hand, such results also indicate that the carriers scattered by acoustic phonons in a linear band do not contribute to the conduction.

From the discussion above, a conclusion can be drawn that high order dispersive bands are beneficial for the thermoelectric power factor. As the band dispersion order *n* increases from 2 to 10, as long as the acoustic phonon scattering process dominates, the power factor can be enhanced by an order of magnitude compared to the parabolic bands. In order to understand how high order dispersive band leads to a higher thermoelectric power factor, more details of the change on the band structure caused by the high band dispersion order are needed. Since the improvement mostly comes from the enhancement of the Seebeck coefficient, it may be helpful to explore what causes the Seebeck coefficient to increase. For degenerate semiconductors, the Seebeck coefficient can be expressed as the Mott relation as:

$$S = \frac{\pi^2}{3}\frac{k_B}{e}k_B T\left[\frac{dln(\mu(E)\varphi(E))}{dE}\right]_{E_F} \qquad \textit{Equation 6.68}$$

where $\mu(E)$ is the energy-dependent carrier mobility. The enhancement of the Seebeck coefficient suggests that the derivative of the product of the mobility and the density of states with respect to the energy must increase. From *Eqn.* 6.3, the energy-dependent density of states and its derivative with respect to energy are shown in Fig. 6.2.

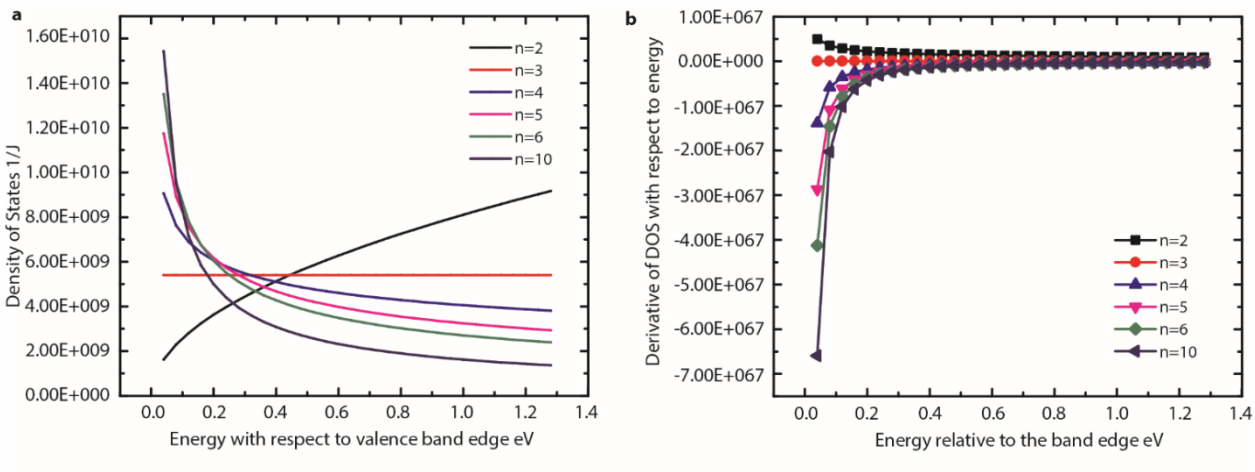

Figure 6.2 (a) Density of states and (b) its energy dependence for various band dispersions.

The energy-dependent density of states is quite different for high order dispersive bands than the parabolic one. The density of states approaches to infinity as the energy approaches to the band edge for band dispersion order larger than 3 and energies near the valence band edge. Such a feature leads to a significantly enhanced magnitude of the derivative of the density of states with respect to the energy near band edge, as shown in Fig. 6.2b. This also explains the trend of the calculated Fermi level shown in Fig. 6.1a. The energy-dependent mobility can be calculated from electrical conductivity:

$$\sigma = \int e\varphi(E)\mu(E)f(E)[1-f(E)]dE \qquad \textit{Equation 6.69}$$

The energy-dependent mobility is then written as:

$$\mu(E) = qa^{\frac{2}{n}}w\frac{n^2}{3\hbar^2}\left(\frac{n+1}{n}+p\right)E^{1-\frac{2}{n}+p}(1+exp(\eta^*-\eta)) \qquad \textit{Equation 6.70}$$

The results are plotted in Fig. 6.3 for two different doping concentrations. The corresponding Fermi levels are also labeled in the figures.

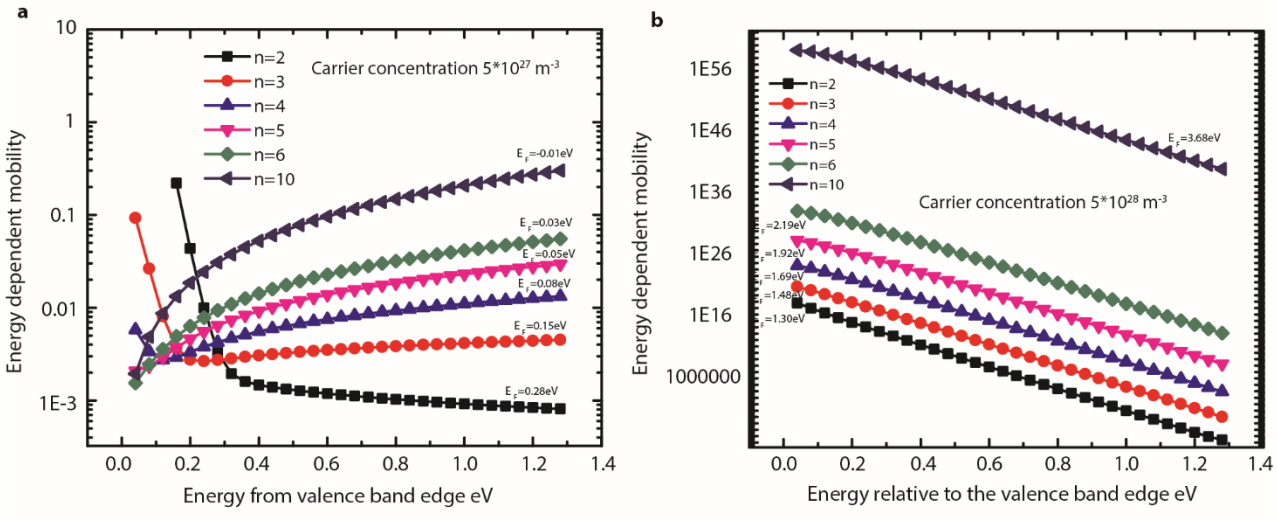

Figure 6.3 Energy-dependent mobility for various band dispersions of carrier concentration of (a) 5×10^{27} m^{-3} and (b) 5×10^{28} m^{-3}.

It is obvious that the energy dependence of the mobility depends heavily on doping concentration. At the doping concentration of 5×10^{27} m^{-3}, the energy dependence of the mobility has an abrupt change near the Fermi level. This feature is absent in Fig. 6.3b, since the Fermi level falls out of the energy range presented. The product of the energy-dependent density of states and mobility is shown in Fig. 6.4 for the doping concentration of 5×10^{27} m^{-3}. As the band dispersion order increases, the Fermi level is pushed closer to the band edge, where the derivative of the product of density of states and mobility with respect to the energy increases. This is why the Seebeck coefficient is significantly enhanced for higher order dispersive bands.

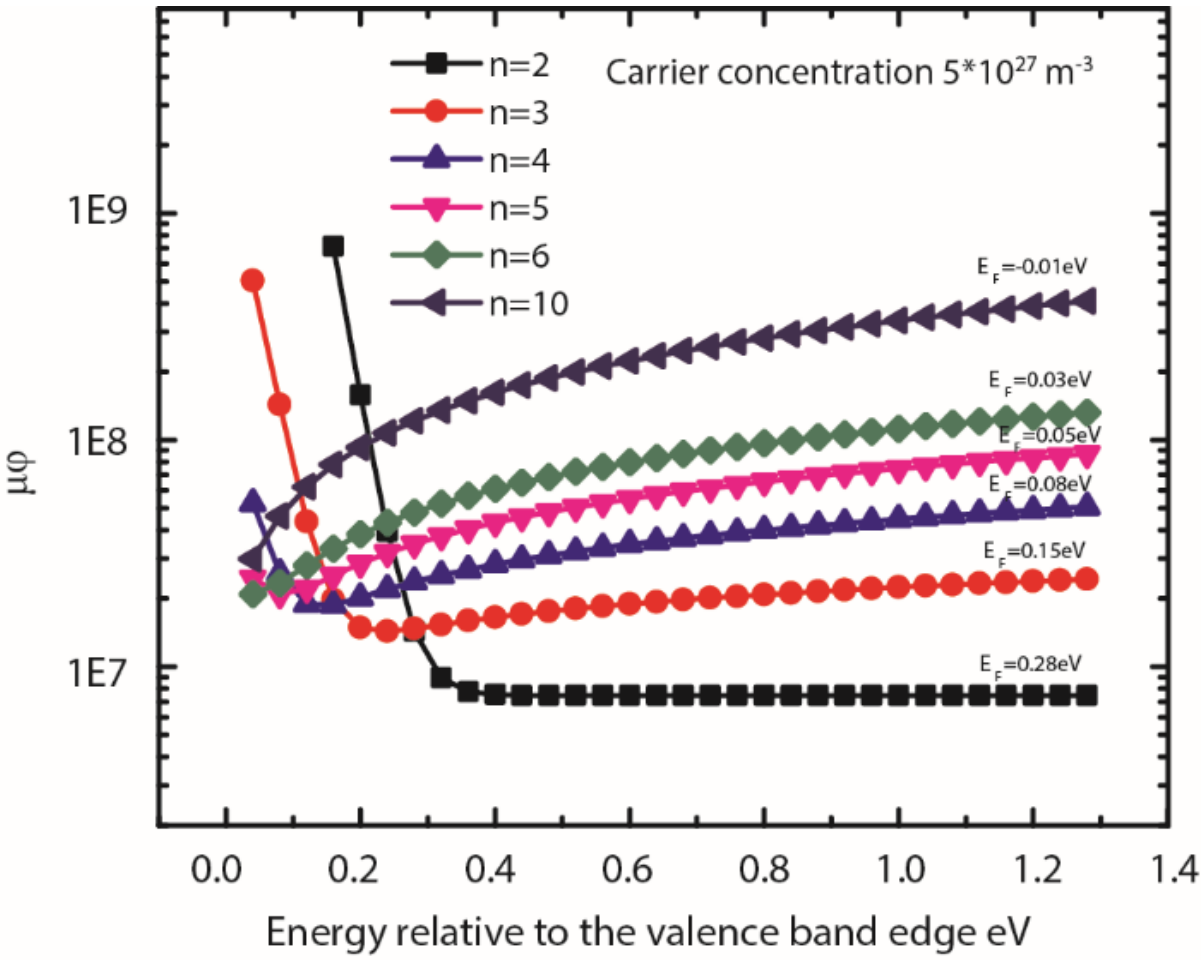

Figure 6.4 The mobility multiplied by the density of states as a function of carrier energy.

Room temperature mobility for various band dispersion orders and various doping concentrations is shown in Figure 6.5a. The mobility of parabolic bands is larger than that of high order dispersive bands up to a doping concentration of 10^{28} m^{-3}. The results above 10^{28} m^{-3} are not discussed here, since most materials do not possess that high carrier concentration. It is also interesting that varying the effective mass of a parabolic band only alters the optimized doping concentration for the maximum power factor. The maximum value is not influenced, as

shown in Fig. 6.5b. It suggests that band engineering of a single parabolic band is not capable of enhancing the power factor.

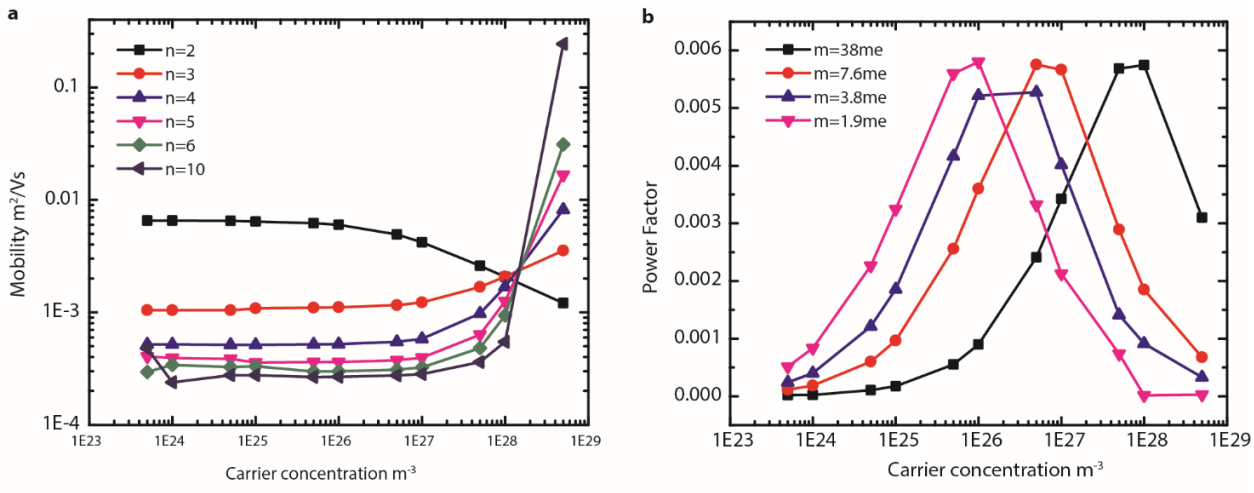

Figure 6.5 (a) Room temperature mobility of various band dispersions at different carrier concentrations. (b) Carrier concentration dependent power factor for a single parabolic band with various effective mass.

6.4 Summary

Electrical transport coefficients were derived for higher order dispersive bands assuming that the acoustic phonon scattering dominates in this chapter. Numerical calculations are shown for the comparison between the higher order dispersive bands and the parabolic band. I find that the thermoelectric power factor can be enhanced by an order of magnitude by increasing the band dispersion order from 2 to 10. Detailed density of states and mobility analysis suggests that the enhancement mostly originates from the enhanced energy dependence of the product of density of states and mobility. Numerical calculations also show that changing the effective mass

of a parabolic band only changes the optimized carrier concentration for the maximum power factor, but not the maximum power factor value. This suggests that engineering a single parabolic band will not benefit the thermoelectric power factor.

Chapter 7 Conclusion

In this work, we have shown that Sn dopants can be successfully incorporated in the binary skutterudite $CoSb_3$ via bulk polycrystalline materials synthesis. *Ab initio* calculation predicts that Sn resonant electronic levels lie approximately 0.3 eV below the valence band maximum of $CoSb_3$. However, experimental studies did not find a significant enhancement of the power factor. Detailed phase identification and microstructural characterization on the $CoSb_{3-x}Sn_x$ samples using XRD, SEM, and TEM suggests that the solubility limit of Sn in $CoSb_3$ is too low to move the Fermi level deep enough into the valence band to reach the Sn resonant levels. On the other hand, we have shown that Sn dopants significantly reduce the thermal conductivity of $CoSb_3$, leading to an enhanced thermoelectric figure of merit.

An additional approach to further push the Fermi level into the valence band to the vicinity of the Sn resonant levels was pursued. Fe was incorporated on the Co sites as a secondary *p*-type dopant. In order to stabilize the crystal structure and further reduce the thermal conductivity, Yb was also filled in the interstitial sites. Microstructural analysis corroborated that Sn, Fe, and Yb were successfully incorporated in the matrix of $Yb_zFe_{4-y}Co_ySb_{12-x}Sn_x$. However, thermoelectric transport measurement results still did not exhibit the influence of the Sn resonant levels. The Sn-doped samples exhibited lower power factor compared to the Sn-free samples. We attributed this to Fermi level pinning by the heavy Fe-*d*-band, which moves to the valence band maximum as the Fe concentration increases.

While Fe doping did not move the Fermi energy sufficiently far to access the Sn resonant levels, we found the convergence of the heavy Fe-d band and the light Sb-p band to be beneficial for the thermoelectric performance of filled skutterudites. $Yb_{0.8}Fe_3CoSb_{12}$ exhibits the best power factor of ~25 $\mu W/cmK^2$. In spite of its greatly increased carrier concentration, $Yb_{0.8}Fe_3CoSb_{12}$ still exhibits an enhanced thermopower compared to $Yb_{0.3}FeCo_3Sb_{12}$ and $Yb_{0.6}Fe_2Co_2Sb_{12}$ at room temperature due to the contribution of the heavy carriers in the Fe-d band. However, the Seebeck coefficient of $Yb_{0.3}FeCo_3Sb_{12}$ exceeds that of $Yb_{0.8}Fe_3CoSb_{12}$ at high temperatures, because the Fermi window at high temperatures becomes so wide that the heavy carriers in the Fe-d band start to contribute to the conduction even in $Yb_{0.3}FeCo_3Sb_{12}$ and thus the Seebeck coefficient is mainly dependent on the carrier concentration. The benefits from the large effective mass and the drawback of the low mobility suggest that an optimized Fermi level exists for thermoelectric performance. Conventional doping on the Sb sites is able to tune the carrier concentration and adjust the Fermi level; however, ionized impurity scattering makes such a method less promising. Thus, a novel doping mechanism is desired.

In addition to ionic impurity scattering, the low ionization energy of most of dopants results in a temperature-independent carrier concentration above the deionization temperature (this temperature is usually very low). Numerical calculation results indicate that a temperature-independent carrier concentration is not beneficial for thermoelectric applications over a wide temperature range. The peak carrier concentration of the power factor varies with temperature. Instead of using elements, secondary phase materials are intentionally incorporated in the matrix. With the Fermi level offset between the matrix and the secondary phase varying with temperature, the charge transfer across the interface is also temperature-dependent. This leads to a temperature-dependent carrier concentration in the matrix. We demonstrate the novel doping

method in GeTe-$CuInTe_2$ composites. The average power factor over a wide temperature range is significantly enhanced. Moreover, the mobility of GeTe-$CuInTe_2$ composites is significantly larger than GeTe-In_2Te_3 solid solutions, suggesting that doping with secondary phase materials is able to tune the carrier concentration without sacrificing the mobility. This novel method can be used in other materials, such as filled skutterudites as proposed in Chapter 4.

Finally, engineering band dispersion is proposed as a potential method of enhancing thermoelectric power factor. As the band dispersion index *n* increases from 2 to 10, the power factor can be enhanced by almost one order of magnitude. Such enhancement originates from the enhancement of the thermopower. Detailed band structure analysis suggests that the enhancement on the thermopower comes from the increased energy dependence of the product of density of states and mobility.

Future work proposed based on the discoveries made in this work has three aspects. Firstly, other elements with their resonant electronic levels in $CoSb_3$ closer to the top of the valence band compared to Sn should be considered. Secondly, the novel doping method devised in Chapter 5 has the potential to be applied to other materials. For those materials which have optimized power factor only at high temperatures, such as heavily doped semiconductors, materials carefully selected based on their temperature dependence of the Fermi levels can be incorporated as secondary phases to optimize the matrix carrier concentration over a wide temperature range, and hence enhance the average thermoelectric performance. For materials that need to be further optimized for thermoelectric performance, such as filled skutterudites discussed in Chapter 4, materials with appropriate Fermi level offset with respect to the matrix can be incorporated to further adjust the matrix carrier concentration without deteriorating mobility to further enhance power factor. Finally, engineering band dispersion in materials can

be beneficial for thermoelectric applications. Theoretically, transport coefficients of higher order dispersive bands need to be derived for other scattering processes. Moreover, mechanisms with potentials to achieve higher order dispersive bands, such as introducing strong spin-orbit interaction or altering the symmetry of the lattice structure, need to be confirmed theoretically. Once confirmed by theory, materials with specific properties will be explored experimentally.

References

1. *Energy Flow Chart*. 2016; Available from: https://flowcharts.llnl.gov.
2. Cataldo, R.L.a.B., Gary L., *U.S. Space Radioisotope Power Systems and Applications: Past, Present and Future*.
3. Energy, A.; Available from: www.alphabetenergy.com.
4. Rowe, D.M., *General Principles and Basic Considerations*, in *Thermoelectrics Handbook Macro to Nano*, D.M. Rowe, Editor. 2006, CRC Press Taylor & Francis Group, LLC: Boca Raton.
5. Lutterotti, L., et al., *Combined texture and structure analysis of deformed limestone from time-of-flight neutron diffraction spectra.* Journal of Applied Physics, 1997. **81**(2): p. 594-600.
6. Parker, W.J., et al., *Flash Method of Determining Thermal Diffusivity, Heat Capacity, and Thermal Conductivity.* Journal of Applied Physics, 1961. **32**(9): p. 1679.
7. Ackermann, J. and A. Wold, *Preparation and Characterization of Cobalt Skutte-Rudites Cop3, Coas3 and Cosb3.* Journal of Physics and Chemistry of Solids, 1977. **38**(9): p. 1013-1016.
8. Singh, D.J. and W.E. Pickett, *Skutterudite Antimonides - Quasi-Linear Bands and Unusual Transport.* Physical Review B, 1994. **50**(15): p. 11235-11238.
9. Morelli, D.T., et al., *Low-Temperature Transport-Properties of P-Type Cosb3.* Physical Review B, 1995. **51**(15): p. 9622-9628.
10. Caillat, T., A. Borshchevsky, and J.P. Fleurial, *Properties of single crystalline semiconducting CoSb3.* Journal of Applied Physics, 1996. **80**(8): p. 4442-4449.
11. Sofo, J.O. and G.D. Mahan, *Electronic structure of CoSb3: A narrow-band-gap semiconductor.* Physical Review B, 1998. **58**(23): p. 15620-15623.
12. Uher, C., *Skutterudite-based thermoelectrics*, in *Thermoelectrics Handbook Macro to Nano*, D.M. Rowe, Editor. 2006, CRC Press Taylor and Francis Group, LLC: Boca Raton.
13. Meisner, G.P., et al., *Structure and lattice thermal conductivity of fractionally filled skutterudites: Solid solutions of fully filled and unfilled end members.* Physical Review Letters, 1998. **80**(16): p. 3551-3554.
14. Yang, J., et al., *Dual-frequency resonant phonon scattering in BaxRyCo4Sb12 (R=La, Ce, and Sr).* Applied Physics Letters, 2007. **90**(19).
15. Alboni, P.N., et al., *Thermoelectric properties of La(0.9)CoFe(3)Sb(12)-CoSb(3) skutterudite nanocomposites.* Journal of Applied Physics, 2008. **103**(11).
16. Graff, J., et al., *High-Temperature Thermoelectric Properties of Co4Sb12-Based Skutterudites with Multiple Filler Atoms: Ce0.1In (x) Yb (y) Co4Sb12.* Journal of Electronic Materials, 2011. **40**(5): p. 696-701.
17. Deng, L., et al., *The thermoelectric properties of InxCo4Sb12 alloys prepared by HPHT.* Materials Letters, 2011. **65**(19-20): p. 2927-2929.

18. Shi, X., et al., *Multiple-Filled Skutterudites: High Thermoelectric Figure of Merit through Separately Optimizing Electrical and Thermal Transports.* Journal of the American Chemical Society, 2011. **133**(20): p. 7837-7846.
19. Liu, R.H., et al., *p-Type skutterudites RxMyFe3CoSb12 (R, M = Ba, Ce, Nd, and Yb): Effectiveness of double-filling for the lattice thermal conductivity reduction.* Intermetallics, 2011. **19**(11): p. 1747-1751.
20. Rogl, G., et al., *A new generation of p-type didymium skutterudites with high ZT.* Intermetallics, 2011. **19**(4): p. 546-555.
21. Rogl, G., et al., *Thermoelectric properties of p-type didymium (DD) based skutterudites DDy(Fe1-xNix)(4)Sb-12 (0.13 <= x <= 0.25, 0.46 <= y <= 0.68).* Journal of Alloys and Compounds, 2012. **537**: p. 242-249.
22. Mahan, G.D. and J.O. Sofo, *The best thermoelectric.* Proceedings of the National Academy of Sciences of the United States of America, 1996. **93**(15): p. 7436-7439.
23. Nemov, S.A. and Y.I. Ravich, *Thallium-doped lead chalcogenides: investigation methods and properties.* Uspekhi Fizicheskikh Nauk, 1998. **168**(8): p. 817-842.
24. Heremans, J.P., B. Wiendlocha, and A.M. Chamoire, *Resonant levels in bulk thermoelectric semiconductors.* Energy & Environmental Science, 2012. **5**(2): p. 5510-5530.
25. Heremans, J.P., et al., *Enhancement of thermoelectric efficiency in PbTe by distortion of the electronic density of states.* Science, 2008. **321**(5888): p. 554-557.
26. Jaworski, C.M., V. Kulbachinskii, and J.P. Heremans, *Resonant level formed by tin in Bi2Te3 and the enhancement of room-temperature thermoelectric power.* Physical Review B, 2009. **80**(23).
27. Bansil, A., et al., *Electronic structure and magnetism of Fe3-xVxX (X=Si, Ga, and Al) alloys by the KKR-CPA method.* Physical Review B, 1999. **60**(19): p. 13396-13412.
28. Stopa, T., S. Kaprzyk, and J. Tobola, *Linear aspects of the Korringa-Kohn-Rostoker formalism.* Journal of Physics-Condensed Matter, 2004. **16**(28): p. 4921-4933.
29. Perdew, J.P. and Y. Wang, *Pair-Distribution Function and Its Coupling-Constant Average for the Spin-Polarized Electron-Gas.* Physical Review B, 1992. **46**(20): p. 12947-12954.
30. Kaprzyk, S. and A. Bansil, *Greens-Function and a Generalized Lloyd Formula for the Density of States in Disordered Muffin-Tin Alloys.* Physical Review B, 1990. **42**(12): p. 7358-7362.
31. Shannon, R.D., *Revised Effective Ionic-Radii and Systematic Studies of Interatomic Distances in Halides and Chalcogenides.* Acta Crystallographica Section A, 1976. **32**(Sep1): p. 751-767.
32. Zhu, J.O., et al., *Effect of aluminum on the reaction synthesis of ternary carbide Ti3SiC2.* Scripta Materialia, 2003. **49**(7): p. 693-697.
33. Bolzan, A.A., et al., *Structural studies of rutile-type metal dioxides.* Acta Crystallographica Section B-Structural Science, 1997. **53**: p. 373-380.
34. Zobrina, B.N. and L.D. Dudkin, *Investigation of the Thermoelectric Properties of Cosb3 with Sn, Te, and Ni Impurities.* Soviet Physics-Solid State, 1960. **1**(12): p. 1668-1674.
35. Kim, I.H., K.H. Park, and S.C. Ur, *Thermoelectric properties of Sn-doped CoSb3 prepared by encapsulated induction melting.* Journal of Alloys and Compounds, 2007. **442**(1-2): p. 351-354.

36. Tobola, J., et al., *Thermoelectric properties and electronic structure of Sn-doped CoSb3.* Twenty-Second International Conference on Thermoelectrics, Proceedings Ict '03, 2003: p. 76-80.
37. Heremans, J.P. and C.M. Jaworski, *Experimental study of the thermoelectric power factor enhancement in composites.* Applied Physics Letters, 2008. **93**(12).
38. H., P.E., *The Hall Effect and Related Phenomena*. 1960, London: Butterworths.
39. Fritzsche, H., *General Expression for Thermoelectric Power.* Solid State Communications, 1971. **9**(21): p. 1813.
40. Qiu, P.F., et al., *Effects of Sn-doping on the electrical and thermal transport properties of p-type Cerium filled skutterudites.* Journal of Alloys and Compounds, 2011. **509**(4): p. 1101-1105.
41. Zhou, C., et al., *Thermoelectric properties of P-type Yb-filled skutterudite YbxFeyCo4-ySb12.* Intermetallics, 2011. **19**(10): p. 1390-1393.
42. Tang, X.F., et al., *Synthesis and thermoelectric properties of p-type barium-filled skutterudite BayFexCo4-xSb12.* Journal of Materials Research, 2002. **17**(11): p. 2953-2959.
43. Qiu, P.F., et al., *"Pesting"-like oxidation phenomenon of p-type filled skutterudite Ce0.9Fe3COSb12.* Journal of Alloys and Compounds, 2014. **612**: p. 365-371.
44. Dilley, N.R., et al., *Intermediate valence in the filled skutterudite compound YbFe4Sb12.* Physical Review B, 1998. **58**(10): p. 6287-6290.
45. Yang, J., et al., *Trends in electrical transport of p-type skutterudites RFe4Sb12 (R = Na, K, Ca, Sr, Ba, La, Ce, Pr, Yb) from first-principles calculations and Boltzmann transport theory.* Physical Review B, 2011. **84**(23).
46. Kajikawa, Y., *Analysis of high-temperature thermoelectric properties of p-type CoSb3 within a two-valence-band and two-conduction-band model.* Journal of Applied Physics, 2014. **115**(20).
47. Ravich, Y.I., B.A. Efimova, and I.A. Smirnov, *Semiconducting Lead Chalcogenides*. Monographs in Semicondutor Physics, ed. L.S. Stilbans. 1970, New York: Plenum.
48. Kajikawa, Y., *Strong temperature dependence of the Hall factor of p-type CoSb3: A re-analysis incorporating band nonparabolicity.* Journal of Applied Physics, 2015. **117**(5).
49. Zawadzki, W., *Electron-Transport Phenomena in Small-Gap Semiconductors.* Advances in Physics, 1974. **23**(3): p. 435-522.
50. Thompson, D.R., et al., *Rare-earth free p-type filled skutterudites: Mechanisms for low thermal conductivity and effects of Fe/Co ratio on the band structure and charge transport.* Acta Materialia, 2015. **92**: p. 152-162.
51. Enderlein, R. and N.J.M. Horing, *Fundamentals of Semiconductor Physics and Devices*. 1997, Singapore: World Scientific.
52. Pei, Y.Z., A.F. May, and G.J. Snyder, *Self-Tuning the Carrier Concentration of PbTe/Ag2Te Composites with Excess Ag for High Thermoelectric Performance.* Advanced Energy Materials, 2011. **1**(2): p. 291-296.
53. Goldak, J., et al., *Structure of Alpha Gete.* Journal of Chemical Physics, 1966. **44**(9): p. 3323.
54. Liu, R.H., et al., *Ternary compound CuInTe2: a promising thermoelectric material with diamond-like structure.* Chemical Communications, 2012. **48**(32): p. 3818-3820.

55. Sun, H., et al., *Highly efficient (In2Te3)(x)(GeTe)(3-3x) thermoelectric materials: a substitute for TAGS.* Physical Chemistry Chemical Physics, 2014. **16**(29): p. 15570-15575.
56. Xue, L., B. Xu, and L. Yi, *Electronic structures and thermoelectric properties of solid solutions CuGa1-xInxTe2: A first-principles study.* Chinese Physics B, 2014. **23**(3).
57. Zhang, X.Z., et al., *A study of the electronic structures and optical properties of CuXTe2 (X = Al, Ga, In) ternary semiconductors.* Computational and Theoretical Chemistry, 2013. **1010**: p. 67-72.
58. Lewis, J.E., *Optical Properties and Energy-Gap of Gete from Reflectance Studies.* Physica Status Solidi B-Basic Solid State Physics, 1973. **59**(1): p. 367-377.
59. Korzhuev, M.A., *On the Fundamental Energy-Gap in Gete.* Physica Status Solidi B-Basic Research, 1982. **112**(1): p. K39-K41.
60. Wu, D., et al., *Origin of the High Performance in GeTe-Based Thermoelectric Materials upon Bi2Te3 Doping.* Journal of the American Chemical Society, 2014. **136**(32): p. 11412-11419.
61. Pei, Y.Z., et al., *Convergence of electronic bands for high performance bulk thermoelectrics.* Nature, 2011. **473**(7345): p. 66-69.
62. Chen, X., D. Parker, and D.J. Singh, *Importance of non-parabolic band effects in the thermoelectric properties of semiconductors.* Scientific Reports, 2013. **3**.